

2022

## Highly Sensitive Soft Foam Sensors for Wearable Applications

Xiao Wang

Follow this and additional works at: <https://ro.uow.edu.au/theses1>

**University of Wollongong**

**Copyright Warning**

You may print or download ONE copy of this document for the purpose of your own research or study. The University does not authorise you to copy, communicate or otherwise make available electronically to any other person any copyright material contained on this site.

You are reminded of the following: This work is copyright. Apart from any use permitted under the Copyright Act 1968, no part of this work may be reproduced by any process, nor may any other exclusive right be exercised, without the permission of the author. Copyright owners are entitled to take legal action against persons who infringe their copyright. A reproduction of material that is protected by copyright may be a copyright infringement. A court may impose penalties and award damages in relation to offences and infringements relating to copyright material.

Higher penalties may apply, and higher damages may be awarded, for offences and infringements involving the conversion of material into digital or electronic form.

Unless otherwise indicated, the views expressed in this thesis are those of the author and do not necessarily represent the views of the University of Wollongong.

---

Research Online is the open access institutional repository for the University of Wollongong. For further information contact the UOW Library: [research-pubs@uow.edu.au](mailto:research-pubs@uow.edu.au)



# **Highly Sensitive Soft Foam Sensors for Wearable Applications**

Xiao Wang

Supervisors:

Dr. Vitor Sencadas

Prof. Gursel Alici

This thesis is presented as part of the requirement for the conferral of the degree:

Master of Research of

The University of Wollongong

August 2022

# ABSTRACT

Due to people's increasing desire for body health monitoring, the needs of knowing humans' body parameters and transferring them to analyzable and understandable signals become increasingly attractive and significant. The present body-sign measurement devices are still bulky medical devices used in settings such as clinics or hospitals, which are accurate, but expensive and cannot achieve the personalization of usage targets and the monitoring of real-time body parameters. Many commercial wearable devices can provide some of the body indexes, such as the smartwatch providing the pulse/heartbeat information, but cannot give accurate and reliable data, and the data could be influenced by the user's movement and the loose wearing habit, either. In this way, developing next-generation wearable devices combining good wearable experience and accuracy is gathering increasing attention.

The aim of this study is to develop a high-performance pressure/strain sensor with the requirements of comfortable to wear, and having great electromechanical behaviour to convert the physiological signal to an analyzable signal.

In this thesis, a wearable strain/stress capacitive sensor with a porous scaffold structure was prepared. The base material was a porous poly(glycerol sebacate) (PGS) polymer synthesised by a polycondensation reaction and a porous structure was formed by a salt-leached process. After adding ethylene glycol (EG) to improve the dielectric properties, the PGS capacitive sensor could present a capacitance change signal when detecting applied mechanical input on it.

The PGS<sub>40</sub>/EG<sub>60</sub> sensor, with an optimal proportioning of PGS and EG, demonstrated great electromechanical behaviour. It has a high sensitivity of around 0.27 kPa<sup>-1</sup> in the stress range of 0 - 8.91 kPa, a rapid response time of 209 ms, great repeatability, and good static stability within one hour with a maximum of 1.89% percentage change of capacitance change. Besides these performances, the PGS<sub>40</sub>/EG<sub>60</sub> sensor could detect the approaching of an item from more than 30 mm (proximity performance), and recognise the temperature change from 25°C up to 70 °C.

Out of these outstanding behaviour, the PGS<sub>40</sub>/EG<sub>60</sub> sensor is able to detect mild deformation and measure different body physiological signals. It could accurately record the angle of the finger while bending. By attaching it to the skin of the volunteer at the 10<sup>th</sup> rib, the breath pattern of a volunteer could be monitored and the change in lung volume during different breath activities could be monitored. The mild skin deformation caused by volunteer wrist pulse could also be monitored, and two peaks of pulses/heart beating could be displayed. To display its good weight measuring performance, this sensor was compared with a commercial load cell, and it showed a weight measurement capability very close to that of the load cell up to 200 g.

Although there is still some remaining work to optimize the sensor performance and applications, the PGS<sub>40</sub>/EG<sub>60</sub> sensor owes a large potential to be applied in varieties of biomedical applications, such as wearable body-sign measuring devices, soft robots and human-machine interfaces.

## ACKNOWLEDGMENTS

First of all, I would like to acknowledge my supervisor, Dr Vitor Sencadas for his constant support and help. I appreciate his enthusiasm and patience with me who didn't know much about the project at the beginning, and he knew me only from his polymer course. He introduced the project in detail and enthusiastically from the morphology of the polymer sensor, to its properties, and to its excellent potential. Even though my English listening was very poor and maybe I could only understand maybe 50% - 60% of it, I still felt his enthusiasm and patience, as if he knew me well and I was like a student of his for many years. This was much appreciated by me as someone who wanted to do a lab project but couldn't find one at the time. From the beginning of the experiment with the basic experiment process and background, to during the research taking me to other workshops for technical help and meeting and knowing technical staff, he was always patient and devoted to me. Furthermore, he is also a very smart, full of imaginative, very careful and observant person. He could always observe and tell me the problem generated during my project timely, for example, liquid leakage, poor stability or similar problem with sensors, and then we worked together on ways to handle the issues raised and these problems were always completed with new methods and with the support of 3D printing or electrical staffs from the other workshop. I am very grateful to him for helping me with my project and my thesis even after he returned to his home country, and for the regular bi-weekly meetings to push me and keep me motivated to the project and report on the new content. I have not had the opportunity to do this before, but here I would like to thank you very much for the care and help you have given me. I hope this job makes you proud and hope all is well with you in Portugal.

I would also like to thank my parents, who kept giving the mentally support during my master's degree. My father is a decisive and determined person who always gives me the right suggestions when things are confusing to me. My mother is nice and gentle that also cures me when things get tough and my emotion goes down. Hope I could finish my master's degree and probably PhD degree soon and I can come back to reunite with you.

Furthermore, give my thank my other supervisor, Prof. Gursel Alici for your kind care and support, also for suggestions on the research and other aspects you gave to me every time I meet you in the hallway of building 2 and 39A. Thank you for your catch-up meeting taking out of your busy schedule to guide me in the directions for my project. Hope all is well with your work and hope there will be more Sunny days so you can enjoy tennis.

I am indebted to my senior, Thomas Searle. He is also kind and patient. To me, he is like a senior and a uni model who know so many skills and knowledge. He taught me the laser cutting machine and the 3D printing devices, told me the electrical knowledge about capacitance converter and proximity, and helped me find items in labs during the pandemic lockdown. Cannot count how many times he help me and cannot thank him just once. Hope all is well after your PhD graduation and find a desired job.



Words cannot express my appreciation for all of my friends. Thanks to Zheng Xue as my partner for so many things, to Durga Tandon for your active chatting and practical help, to Xuexiao Liu and Zhijun Qiu just like big sisters to me and as my cooking partners and for your healing and cheering words, to Prof. Hunjun Li, Prof. Hongtao Zhu for your constant support and suggestions for both my studies and life, to Guoguo Yu and Ting Xia for your Lunar new year meal invitation and demonstrations for young people's lifestyle, to all my friends from the UOW tennis club, Arah, Andy, Danielle, Kobil, Lana, Adrian, Dimitri.

Also, acknowledge all the staff from different workshops or groups. Thanks to Douglas Henness to repair the broken cable "a thousand times", thanks to Chris Hally-Burton, Stuart Rodd and Steve Selby for all the laser cutter and milling machine work, and thanks to Geetika Maddirala for your help on Matlab software.

Last but not least, I am sending sincere acknowledgments and the highest respect to my country, China. I, being one of the millions of students studying abroad, am proud of my motherland. You are always the strongest shield for us.

# **CERTIFICATION**

I, Xiao Wang, declare that this thesis submitted in fulfilment of the requirements for the conferral of the degree Master of Research, from the University of Wollongong, is wholly my own work unless otherwise referenced or acknowledged. This document has not been submitted for qualifications at any other academic institution.

---

Xiao Wang

4<sup>th</sup> August 2022

# TABLE OF CONTENTS

ABSTRACT .....	I
ACKNOWLEDGMENTS .....	II
CERTIFICATION .....	IV
TABLE OF CONTENTS .....	V
LIST OF FIGURES .....	IX
LIST OF TABLES .....	XIV
LIST OF EQUATIONS .....	XV
LIST OF ABBREVIATIONS .....	XVI
Chapter 1 Introduction .....	1
1.1 Background .....	1
1.2 Aims and Novelty .....	2
1.3 Project Path .....	3
1.4 Thesis Outline .....	3
Chapter 2 Literature review .....	5
2.1 Wearable Devices .....	5
2.1.1 Introduction .....	5
2.1.2 E-skin, implantable devices, and other advanced devices with additional features .....	6
2.1.3 Wearable Sensors .....	9
2.2 Wearable Pressure/strain Sensor and Their Working Principles .....	14
2.2.1 Piezoresistive Sensor .....	14
2.2.2 Piezoelectric Sensor .....	15
2.2.3 Capacitive Sensor .....	17
2.2.4 Comparison between Different Sensors .....	17
2.2.5 Fundamentals of a Parallel Plate Capacitor .....	18
2.2.5.1 Principles of Dielectric Polarization and Capacitance .....	19
2.2.5.2 Equations for Capacitance and Permittivity .....	20
2.2.5.3 Dielectric Loss .....	20
2.2.6 Methods to Improve the Performances of Capacitive Sensors .....	22
2.2.6.1 Micro-structure .....	22

2.2.6.1.1	Template Method .....	22
2.2.6.1.2	Phase Separation.....	24
2.2.6.1.3	Gas Foaming.....	25
2.2.6.2	High-dielectric material .....	25
2.2.7	Other Performance Related Background .....	28
2.2.7.1	Proximity .....	28
2.2.7.2	Plasticizer Liquid Caused Drift .....	29
2.3	Material Selection .....	30
2.3.1	Sensor structure .....	30
2.3.2	Dielectric material .....	30
2.3.3	Electrodes material .....	33
2.3.4	Poly(glycerol sebacate) as Dielectric material .....	36
2.4	Outlook .....	38
Chapter 3	Material Preparation and Characterization .....	39
3.1	Chemicals and Reagents Used .....	39
3.2	Material Preparation .....	39
3.3	PGS Dry Sensor Assembly .....	40
3.4	Material Characterization .....	42
3.4.1	Sample Morphology .....	42
3.4.2	Mechanical Behaviour.....	42
3.4.3	Electrical Behaviour .....	42
3.5	Sensor Characterization .....	43
3.5.1	Electromechanical Behaviour.....	43
3.5.1.1	Sensitivity and Gauge Factor.....	44
3.5.1.2	Response Time and Recovery Time .....	45
3.5.1.3	Static Stability .....	45
3.5.1.4	Repeatability and Long-term Dynamic Stability .....	45
3.5.2	Environmental Behaviour.....	46
3.5.2.1	Proximity .....	46
3.5.2.2	Temperature Sensitivity.....	47
Chapter 4	Results and Discussion .....	48

4.1	PGS Foam Characterization.....	48
4.1.1	Morphology .....	48
4.1.2	Mechanical Behaviour.....	48
4.1.3	Electrical Behaviour .....	49
4.2	PGS Dry Sensor Characterization.....	50
4.2.1	Capacitance Change Signal in Load-unload Electromechanical Experiments .....	50
4.2.2	Sensitivity and Gauge Factor.....	51
4.2.3	Static and Dynamic Electromechanical Behaviour .....	52
4.3	PGS/EG Sensor Characterization .....	53
4.3.1	Capacitance Change Signal in Load-unload Electromechanical Experiment.....	54
4.3.2	Sensitivity and Gauge Factor.....	54
4.3.3	Static Stability .....	55
4.3.3.1	Assessment of the Drift Issue Origins .....	55
4.3.3.2	Ecoflex Casing Influence.....	57
4.4	PGS <sub>40</sub> /EG <sub>60</sub> Sensor Characterization .....	59
4.4.1	Capacitance Change Signal in Load-unload Electromechanical Experiment.....	59
4.4.2	Sensitivity and Gauge Factor.....	60
4.4.3	Response Time and Recovery Time.....	61
4.4.4	Repeatability.....	62
4.4.5	Long-term dynamic stability .....	62
4.4.6	Environmental Behaviour.....	63
4.4.6.1	Proximity .....	63
4.4.6.2	Temperature Sensitivity.....	64
Chapter 5	Sensor's Potential for Wearable Applications.....	66
5.1	Finger Bending Monitoring .....	66
5.2	Breathing Measurement.....	67
5.3	Heart Beating Measurement .....	69
5.4	Proximity .....	71
5.5	Temperature Monitoring.....	72
5.6	Weight Measurement Performance.....	74
Chapter 6	Conclusions and Recommendations for Future Work.....	77

6.1	Conclusion .....	77
6.2	Recommendations for Future Work.....	78
	References.....	82
	Appendices.....	91
	Appendix A.....	91
	A.1 Preparation Related Devices.....	91
	A.2 Performance Measurement Devices .....	95
	Appendix B .....	98

# LIST OF FIGURES

Figure 1.1 The project path. ....	3
Figure 2.1 Wearable technology tracks users' data and transmits the data through Internet [16]. ....	5
Figure 2.2 Various e-skins. (a) Zhu's piezoelectric fibre. (i) Photo image, (ii) Monitoring wrist and elbow bending, and (iii) tactile mapping (reprinted with permission from Ref. [34]). (b) Katerinopoulou's temperature sensor. (i) Photo image, (ii) temperature measuring ability compared with a commercial thermistor, and (iii) detecting the temperature of a human hand (reprinted with permission from Ref. [35]). ....	7
Figure 2.3 Present implant devices. (a) Viventi's flexible electrode array (reprinted with permission from Ref. [36]). (i) Photograph, (ii) Electrode array was placed on the visual cortex. (iii) 64-color map monitor presented the neural response to the stimuli. (b) Kim's balloon catheter sensor (i) in deflation and inflation states, (ii) measuring the heart condition and the epicardial ablation lesions, (iii) The record of the electrical signal and mechanical contact, and the temperature monitoring (reprinted with permission from Ref. [37]). ....	8
Figure 2.4 Some devices with unique functions. (a) Tee's self-heal sensor, (i) photo image. The recovery of (ii) conductivity performance and (iii) mechanical performance (reprinted with permission from Ref. [38]). (b) Fan's transparent sensor, (i) photo image (ii) attached to the screen of the phone (iii) Sensing the mild water drop (reprinted with permission from Ref. [39]). ....	9
Figure 2.5 Some present wearable sensors showed good stretchability, (a) Yamada's wearable devices and the good stretchability mechanism of gaps, islands and bundles bridging (reprinted with permission from Ref. [40]). (b) Mattmann's strain sensor (i) Sensor thread; (ii) Sensor thread attached to clothes; (iii) Its good stretchability up to 80% strain (reprinted with permission from Ref. [41]). ....	10
Figure 2.6 Some present wearable sensors showed good sensitivity; (a) Sharma's capacitive sensor; (i) detecting the pulse and, (ii) respiration pattern (reprinted with permission from Ref. [43]). (b) Kim's capacitive pressure sensor, (i) Attached on the wrist; (ii) Size and microstructure; (iii) sensor's pulse waveform; (iv) pulse waveform from ClearSight device (reprinted with permission from Ref. [44]). ....	11
Figure 2.7 The SWS provides could provide the electrical signal of the body and also other parameters (reprinted with permission from Ref. [42]). ....	12
Figure 2.8 Some present wearable sensors to measure finger bending movement, (a) Junh's sensor measured the finger bending angle (reprinted with permission from Ref. [45]). (b) Wang's sensor recorded (i) finger tapping on the touchpad of a laptop, (ii) the real-time finger bending, and (iii) the finger power to lift cups with different weights (reprinted with permission from Ref. [46]). ....	13
Figure 2.9 Some present wearable sensors to measure foot pressure, and leg and elbow movement, (a) Jung's sensor measured the pressure of a part of the foot during walking and running (reprinted with permission from Ref. [45]); (b) Chen's sensor measured the pressures of seven different areas (reprinted with permission from Ref. [47]); (c) Yang's sensor measured the pressures from the front sole and heel and detected the movement of arms and legs (reprinted with permission from Ref. [48]). ....	14
Figure 2.10 Some present wearable piezoresistive sensors. (a) Park's sensor, (i) sensor's structure, (ii) Monitoring human breathing flow through a breathing mask, and (iii) Throat vibration during speaking	

(reprinted with permission from Ref. [54]). (b) Jian's sensor, (i) sensor's structure (ii) Bending and (iii) torsional forces, and (iv) Recognising the different degrees of vibration (reprinted with permission from Ref. [55]).	15
Figure 2.11 Some present wearable piezoelectric sensors. (a) Dagdeviren's sensor, (i) sensor structure, (ii) attached on the wrist, and (iii) monitored the pulse signal (reprinted with permission from Ref. [59]). (b) Zhong's sensor, (i) sensor structure, (ii) sensor pressure array functions as a calculator, and (iii) The sensor's function remain while being cut down (reprinted with permission from Ref. [60]).	17
Figure 2.12 Parallel Plate Capacitor	19
Figure 2.13 Dielectric polarization, (a) the centre of charge coincides with each other; (b) the centre of a symmetrically charged nonpolar molecule shifts [97].	20
Figure 2.14 Definition of complex relative permittivity (reprinted with permission from Ref. [103]).	22
Figure 2.15 Present research using templating Method to create microstructure. (a) Wei used NaCl to create air voids in PDMS (reprinted with permission from Ref. [67]); (b) Jian filled the PDMS/MS composite into a sugar cube (reprinted with permission from Ref. [46]); (c) Sharma mixed the ZnO hemisphere with PDMS and use a continuous centrifugal force to generate a gradient in porosity and pore size (reprinted with permission from Ref. [78]); (d) Mahata applied a rose petal reverse mould template (reprinted with permission from Ref. [108]).	24
Figure 2.16 Ishigami et al. cooled down the PVDF/GTA/glycerol and the non-solvent glycerol showed up (reprinted with permission from Ref. [111]).	25
Figure 2.17 Sensitivities of sensors in present studies after adding different concentrations of high- $\kappa$ filler. (a) Ecoflex with MWCNT (reprinted with permission from Ref. [89]); (b) PDMS with CNT (reprinted with permission from Ref. [66]); (c) porous PDMS with CCP (reprinted with permission from Ref. [67]); (d) TPU with AgNWs (reprinted with permission from Ref. [85]).	26
Figure 2.18 Mechanisms of proximity for two types of capacitive sensors, (a) Self-Capacitance sensor and (b) Mutual capacitance sensor (reprinted with permission from Ref. [63]).	28
Figure 2.19 Parallel plate capacitive sensor. The capacitance decreases and recovers when the human finger approaches and removes (reprinted with permission from Ref. [118]).	29
Figure 2.20 The drift in capacitance stability experiment in Sun's work (reprinted with permission from Ref. [69]).	30
Figure 2.21 Present capacitive sensors using PDMS as the dielectric layer. (a) Wei et al. prepared PDMS-CCP as their dielectric layer (reprinted with permission from Ref. [67]); (b) Xie's napkin wearable sensor with a PDMS dielectric layer (reprinted with permission from Ref. [65]); (c) Kim used PDMS/AgNWs as dielectric layer (reprinted with permission from Ref. [70]); (d) Cui used carbon nanotubes/PDMS as their dielectric material (reprinted with permission from Ref. [71]); (e) Sharma prepared a PDMS dielectric layer (reprinted with permission from Ref. [78]).	31
Figure 2.22 Present capacitive sensors using PVDF or related materials as the dielectric layer. (a) Sharma blended the MXenes ( $\text{Ti}_3\text{C}_2\text{Tx}$ ) with a PVDF-TrFE by an electrospinning process as their dielectric layer (reprinted with permission from Ref. [43]); (b) Chhetry mixed P(VdF-HFP) with [EMIM] [TFSI] (reprinted with permission from Ref. [83]); (c) Cho prepared a P(VdF-HFP) mixed with [EMI] [TFSA] (reprinted with permission from Ref. [84]); (d) Lin prepared a core(PVDF-HFP nanofiber) - shell(PDMS ionogel)	



nanofiber mat (reprinted with permission from Ref. [77]).	32
Figure 2.23 Present capacitive sensors using PU as the dielectric layer. (a) Zhao's sensor with an AgNW interior and a TPU exterior (reprinted with permission from Ref. [85]); Liu mixed HPU solution with a graphene suspension to prepare their dielectric film (reprinted with permission from Ref. [123]); Yao coated graphene nanosheet on a commercial PU sponge as the dielectric layer (reprinted with permission from Ref. [86]).	33
Figure 2.24 Present capacitive sensors using AgNWs as electrode layer. (a) Kim embedded the AgNWs electrode onto the surface of the PDMS substrate (reprinted with permission from Ref. [70]); (b) Xie added AgNWs in ethanol solution to their PDMS dielectric layer (reprinted with permission from Ref. [65]); (c) Li prepared an AgNWs film electrode for their PDMS capacitive sensor (reprinted with permission from Ref. [64]).	34
Figure 2.25 The sebacic acid and glycerol form PGS through condensation polymerization.	37
Figure 3.1 PGS foam preparation.	40
Figure 3.2 Sensor assembling process. (a) Fabrication of the Ecoflex bottom&wall; (b) Ecoflex cover; (c) Laser cutting the silver tapes; (d) Creating an incision on the Ecoflex wall; (e) Assembling (a) - (e); (f) the photo image of the PGS series sensor.	41
Figure 3.3 Sensor's electromechanical behaviour measured with a computer, LCR Meter and universal testing machine.	44
Figure 3.4 Sensor was put on the platform of the universal testing machine.	45
Figure 3.5 Proximity measurement: the pressure head is moved just close to the top surface of the sensor and the proximity experiment process.	47
Figure 4.1 SEM image of the PGS foam. (a) The overall morphology of the PGS foam and (b) detail of the pore walls.	48
Figure 4.2 Stress-strain curve for 3 independent experiments.	49
Figure 4.3 Relative permittivity ( $\epsilon_r$ ) of the PGS and the PGS <sub>40</sub> /EG <sub>60</sub> sensor (a) at different frequencies and (b) at 300 kHz.	50
Figure 4.4 The $\Delta C/C_0$ of the PGS dry sensor under (a) 5 mm/min, 5% strain; (b) 5 mm/min, 20% strain;	51
Figure 4.5 (a) Sensitivity and (b) GF of capacitive sensors.	51
Figure 4.6 (a) Sensitivity, and (b) GF of the PGS dry sensor with strains of 5%, 10%, and 20%.	52
Figure 4.7 The static electromechanical behaviour, (a) Response time and recovery time, (b) Static Stability,	53
Figure 4.8 The assembling of the PGS/EG sensor.	53
Figure 4.9 The $\Delta C/C_0$ of the PGS/EG sensor under (a) 5 mm/min, 5% strain; (b) 5 mm/min, 20% strain;	54
Figure 4.10 (a) Sensitivity, and (b) GF of the PGS/EG sensor with strains of 5%, 10% and 20%.	55
Figure 4.11 The static stability of the PGS/EG sensor.	55
Figure 4.12 The stability of PGS sensors. (a) PGS dry sensor; (b) PGS <sub>60</sub> /EG <sub>40</sub> sensor; (c) PGS <sub>40</sub> /EG <sub>60</sub> sensor;	57
Figure 4.13 The static stability experiment of the PDMS casing sensor, (a) $\Delta C/C_0$ and strain, (b) Stress;	58
Figure 4.14 The $\Delta C/C_0$ of the PGS <sub>40</sub> /EG <sub>60</sub> sensor vs. the PGS dry sensor under (a) 5 mm/min, 5% strain;	

.....	59
Figure 4.15 S of the PGS dry sensor and PGS <sub>40</sub> /EG <sub>60</sub> sensor with strains of 5%, 10% and 20%. ....	60
Figure 4.16 GF of the PGS dry sensor and PGS <sub>40</sub> /EG <sub>60</sub> sensor with strains of 5%, 10% and 20%. ....	61
Figure 4.17 The response and recovery time of the PGS <sub>40</sub> /EG <sub>60</sub> sensor (Represented by blue bars widened for ease of display). ....	62
Figure 4.18 The repeatability experiment of the PGS <sub>40</sub> /EG <sub>60</sub> sensor. ....	62
Figure 4.19 The dynamic stability experiment of the PGS <sub>40</sub> /EG <sub>60</sub> sensor,.....	63
Figure 4.20 Capacitance change in proximity experiment, (a) 200mm proximity experiment; .....	64
Figure 4.21 The change of $\Delta C/C_0$ over the temperature. ....	65
Figure 5.1 Sensor's potential for wearable application. ....	66
Figure 5.2 Finger bending to degrees of (a) 41°, (b) 51°, (c) 58°, (d) 73° while recording (e) $\Delta C/C_0$ vs. time; (f) $\Delta C/C_0$ vs. Finger Bending Angle. ....	67
Figure 5.3 Breathing measurement. (a) The PGS <sub>40</sub> /EG <sub>60</sub> sensor was attached to the skin above the 10 <sup>th</sup> ribs of the volunteer and (b) measured the breath action and partial enlargement of one breath cycle. ....	69
Figure 5.4 Radial augmentation index (reprinted with permission from Ref. [153]), where SBP2 and SBP1 represent the systolic blood pressure of the second peak and first peak, and DBP was the diastolic blood pressure. ....	70
Figure 5.5 The 17.5 s pulses recorded from the volunteer and partial enlargement of one pulse cycle. ....	71
Figure 5.6 Proximity. (a) The sensor could detect the approaching of the finger of around 30mm. ....	72
Figure 5.7 The $\Delta C/C_0$ change of the surface of the beaker, (a) After pouring cold water; (b) Recover; (c) After pouring hot water. ....	73
Figure 5.8 The 3D model of (a) a PTFE platform and (b) a PTFE hanger. ....	74
Figure 5.9 The PGS sensor vs. Load cell comparison system. ....	75
Figure 5.10 (a) The change of $\Delta C/C_0$ and load cell signal with different weights; (b) The fitting of $\Delta C/C_0$ and Load cell signal with weights. ....	76
Figure 6.1 The material (casing) issue. Heat insulation of the thick Ecoflex case. ....	79
Figure 6.2 (a) The oxidization of PGS foam in sensor; (b) Oxidized PGS foam. (c) Unstable capacitance signal after slight oxidation occurs.....	80
Figure 6.3 Oxidation controlled experiments of PGS sensor, (a) Oxidization happened. PGS sensor with full EG and silver tapes; (b) Oxidization happened. PGS dry sensor with silver tapes; (c) No oxidization. PGS sensor with full EG. ....	80
Figure 6.4 The interference between proximity and mechanical force, (a) A clear $\Delta C/C_0$ increase while touching accidentally during proximity; (b) A clear $\Delta C/C_0$ decrease while finger approaching during force experiment.....	81
Figure A.1 PHI Manual Hydraulic Compression Presses – P210C.....	91
Figure A.2 FAITHFUL Vacuum Drying Oven. ....	92
Figure A.3 Corning Hot Plate Stirrer Model PC 351. ....	92
Figure A.4 Fiocchetti Scientific Refrigerators SUPERPOLO 130.....	93
Figure A.5 TOPTION Small Freeze Dryer TOPT-10D. ....	93
Figure A.6 Flashforge Inventor Dual Filament 3D printer.....	94

Figure A.7 Versa Laser Device. ....	94
Figure A.8 JCM-6000 Versatile Benchtop SEM.....	95
Figure A.9 LCR meter from Zurich Instruments MFLI Impedance Analyzer. ....	95
Figure A.10 The interface of the LabOne software.....	96
Figure A.11 Garland Coaxial Cable and Mueller insulate miniature Kelvin clip. ....	96
Figure A.12 Universal testing machine, Shimadzu EZ Experiment Devices [160]. ....	97
Figure A.13 JP-Selecta Heated Vacuum desiccator “Vacuo-temp”. ....	97

## LIST OF TABLES

Table 2.1 Comparison of different types of sensors. ....	17
Table 2.2 Ionic liquids used in some present studies. ....	27
Table 2.3 Recent studies on capacitive strain/pressure sensors with measuring pressure ranges mentioned. .....	36
Table 3.1 List of chemical reagents and materials used in this thesis. ....	39
Table 3.2 The sizes of the PGS dry foam sample and PGS dry sensor. ....	42
Table 3.3 Material Characterization .....	42
Table 3.4 Sensor Characterization.....	43
Table 3.5 Electromechanical Parameters set for universal testing machine and LCR Meter. ....	44
Table B.1 Stability experiments for 3600s. The $\Delta C/C_0$ value, the drift difference of $\Delta C/C_0$ , and the percentage change of $\Delta C/C_0$ of the PGS dry sensor, PGS <sub>60</sub> /EG <sub>40</sub> sensor, PGS <sub>40</sub> /EG <sub>60</sub> sensor and PGS <sub>20</sub> /EG <sub>80</sub> sensor in. ....	104
Table B.2 Repeatability experiments of the PGS <sub>40</sub> /EG <sub>60</sub> sensor. The $\Delta C/C_0$ and differences at load per cycle. .....	105

## LIST OF EQUATIONS

Equation 2.1 .....	20
Equation 2.2 .....	20
Equation 2.3 .....	21
Equation 2.4 .....	21
Equation 2.5 .....	21
Equation 2.6 .....	22
Equation 3.1 .....	43
Equation 4.1 .....	48
Equation 4.2 .....	49
Equation 4.3 .....	49
Equation 4.4 .....	51
Equation 4.5 .....	51
Equation 4.6 .....	64
Equation 5.1 .....	69
Equation 5.2 .....	70
Equation 5.3 .....	75

## LIST OF ABBREVIATIONS

AgNW	Ag nanowires
AIr	Radial augmentation index
AlN	Aluminium nitride
BaTiO <sub>3</sub>	Barium titanate
CB	Carbon black
CCP	Carbon conductive paste
CIP	Carbonyl iron particles
CNT	Carbon nanotube
DI	Deionized water
EA	Ethyl acetate
EDL	Electrical double layer
EEG	Electroencephalogram
EG	Ethylene glycol
EMG	Electromyogram
EOG	Electrooculogram
FDA	Food and Drug Administration
GF	Gauge factor
GTA	Glycerol triacetate
HCl	Hydrochloric acid
high- $\kappa$	High dielectric constant
ILs	Ionic liquids
IoT	Internet of Things
LiNbO <sub>3</sub>	Lithium niobate
MPD	2-methyl-2,4-pentanediol
MS	Microsphere
MWCNT	Multiwall carbon nanotubes
NH <sub>4</sub> HCO <sub>3</sub>	Ammonium bicarbonate
NIPS	Non-solvent induced phase separation
P(VdF-HFP)	Poly(vinylidene fluoride-co-hexafluoropropylene)
PCL	Poly ( $\epsilon$ -caprolactone)
PDLA	Poly(d-lactic acid)
PET	Polyethylene glycol terephthalate
PGS	Poly (glycerol sebacate)
PGS/EG	Poly(glycerol sebacate) foam full immersed in ethylene glycol solution
PGSx/EG100-x	X% weight ratio of PGS foam mixed with (100-x)% weight ratio of EG
PLA	Poly(lactic acid)
PLG	Poly(DL-lactide-co-glycolide)

PLLA	Poly(l-lactic acid)
PMMA	Polymethyl methacrylate
PPI	Pixels per inch
PTFE	Polytetrafluoroethylene
PVDF	Poly(vinylidene fluoride)
S	Sensitivity
SI	Stiffness index
TG	Thermoplastic gelatin
TIPS	Thermally-induced phase separation
TPU	Thermoplastic polyurethane
ZnO	Zinc oxide
$\Delta C/C_0$	Normalized capacitance change

# Chapter 1 Introduction

## 1.1 Background

Body health monitoring is gaining popularity due to increasing health awareness and concerns of people at the individual level. Nowadays, people are willing to track their fitness and well-being wherever and whenever they are. A survey of 2,000 adults in the US with an age composition ranging from Gen Z (born in 1997 - 2012) to baby boomers (born in 1946 – 1964) showed that 75% of Gen Z respondents and 63% of baby boomers respondents worried about their health conditions and wanted to prevent themselves from experiencing illness [1]. Another survey of 1,000 respondents showed that 71% of adults would use a personal health monitoring device if it was clinically accurate while 84% of them believed that tracking their health data with a clinically accurate health monitoring device will improve their overall health [2]. Since the body conditions can be reflected by the measurable physiological parameters, several body-index measuring devices are broadly used in our daily life, such as heart beating testers, sphygmomanometers, electroencephalogram (EEG), electrooculogram (EOG), electromyogram (EMG) and electrocardiogram (ECG).

Each device uses a different mechanism to read human physiological parameters. For instance, the optical heartbeat testers project green light onto blood under the skin and collect the refracted or reflected light to determine the heartbeat based on the calculation of pressure pulse and the time difference between the pulses [3], while a sphygmomanometer uses an inflated cuff to stop the blood flow and reduce the pressure until blood flow to measure the systolic pressure and diastolic pressure [4]. Likewise, ECG is used to measure and diagnose heart conditions. The electrodes and leads of the ECG device are placed on the extremities and torso of the body, which detect the transmembrane ionic currents generated between the cells. These detected ionic currents are then digitized, stored, and processed by a computer, to generate signals that help to assess the heart condition [5]. Furthermore, EMG is used to detect the condition of the muscles and nerves. It is used to measure the movement of muscle by the needles inserted through the skin into the muscles to provide information regarding muscle injuries, disease and neuromuscular disorders [6].

Despite the availability and use of these body-index measuring devices, they are traditionally designed based on a hospital-centric medical model. Due to the uncertainties and randomness of daily activities and body conditions, people require a continuous and real-time body monitoring system even without clinic visits or hospitalization [7]. Furthermore, some of these devices are bulky, uncomfortable to use and unable to deliver real-time information. Although the home or mobile devices are proposed or designed to satisfy the need of consumers, they are neither accurate nor cost-effective [8].

Wearable devices, such as smart watches, have been developed in the last few decades. These smartwatches provide user information such as sleep quality and pulse/heartbeat. However, the



accuracy and reliability of these data are required to be seen. A few smart watches cannot give reliable heartbeat data itself during exercise due to the impact of body movement on device accuracy [8]. The swing of the arm during exercises might cause a challenge to the measurement of heartbeat or other parameters, especially the loose way of wearing watches for many users and some non-deal watches' shape and band design could influence the accuracy of heartbeat measurements a lot [8]. In this way, the need for a comfortable, portable and accurate body index measuring device is growing fastly.

Wearable pressure/strain devices can detect the slight deformation of the skin surface and transfer it to a recognizable signal to identify the physiological parameter. Compared to the traditional hospital-based devices and available wearable devices mentioned earlier, the wearable pressure/strain devices are comfortable to wear, smaller in size and accurate enough to detect real-time body information associated with daily health conditions and physical signs in a disease state [9, 10].

## **1.2 Aims and Novelty**

According to the above statements, the requirements of wearable pressure/strain devices are summarized as follows. Furthermore, the aim and novelty of this thesis are also presented.

1. The material of the sensor is required to be comfortable for users to wear, which means to be soft and have a low Young's Modulus. The sensor needs to have a small size and be flexible. Poly(glycerol sebacate) (PGS) elastomer was chosen to be the base material of the sensor due to its good dielectric properties and soft modulus. This elastomer was synthesized. Besides, a porous microstructure was created for both the comfortable target and the accurate target. The mechanical and electrical behaviour of the material was required to be studied.

The application of PGS was mainly in tissue engineering and drug delivery [11]. Its utilization for wearable sensors was first studied by our Research Group in 2017 [12]. It is a novel and potential material attributed to its good biomedical and excellent elastomeric properties.

2. The sensor needs to be accurate to measure the pressure signal in different ranges, especially mild pressure, such as a pressure of less than 1 kPa caused by the heartbeat or pulse. Also, the other related electromechanical behaviour is required to be measured and have high-quality results. Ethylene glycol (EG) was added to the material to improve its electromechanical behaviour of the material.

The previous studies about the wearable PGS foam sensor focus on its behaviour with the combination of the multiwall carbon nanotubes (MWCNT) [12]. The behaviour of the sensor with the addition of high dielectric liquid, such as EG, still needs to be explored.

3. The behaviour of the assembled sensors is required to be studied, including electromechanical

and environmental behaviour, among many others. According to behaviour, related applications or demonstrations are expected to be explored.

### 1.3 Project Path

The whole research path of this project is presented in a mind-map built in Figure 1.1.

As mentioned above, this project aims to develop a sensor with a good wearing experience and good electromechanical behaviour. The initial stage of this project is the fabrication of PGS foam, and behaviour measurement of the PGS foam material and the PGS dry foam sensor. Due to its relatively poor electromechanical behaviour under mild pressure/strain, the EG was added to improve its performance and study the influence of a liquid with a high dielectric constant dispersed in the elastomeric matrix. The PGS dry sample and PGS/EG sample were assembled in the Ecoflex case, and their performance was experimented with. During the experiment, the PGS/EG sensor show a capacitance change drift in the stability experiment and this led to the second stage experiment.

The second stage is to deal with the stability problem of the PGS/EG sensor. Measurements of the PGS<sub>x</sub>/EG<sub>100-x</sub> sensor were conducted to determine an optimal ratio of PGS and EG. Out of these performances, the related potential applications are demonstrated.

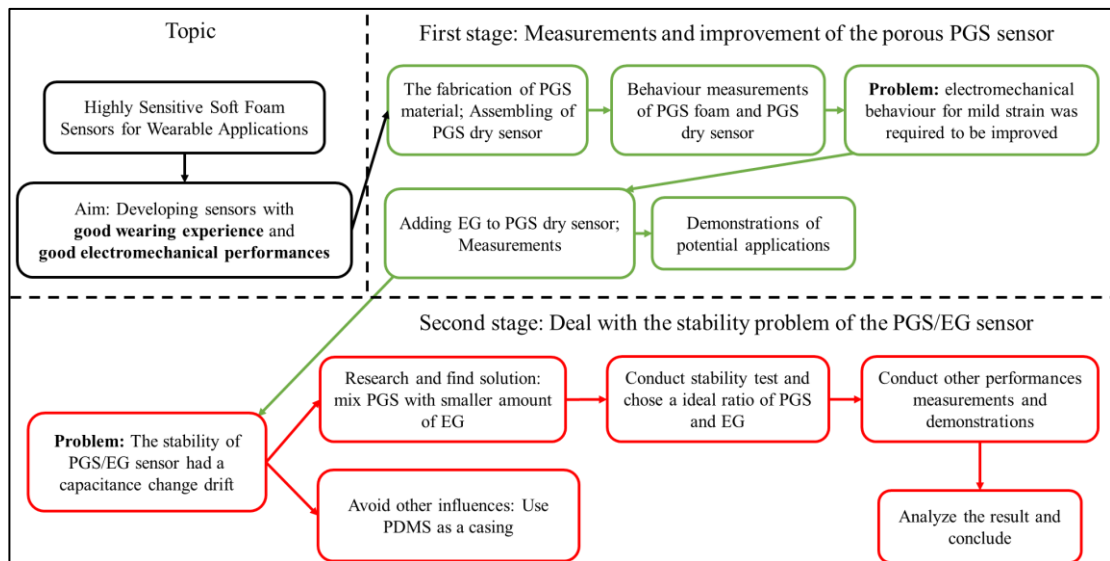


Figure 1.1 The project path.

### 1.4 Thesis Outline

With the aim of developing a wearable pressure/strain sensor with both good wearing experience and great electromechanical performance, this thesis focuses on the wearable PGS sensor with the following outline.

**Chapter 2:** A literature review about wearable sensors is presented. At first, the development and

different types of wearable sensors and pressure sensors, and their working mechanisms and comparisons are discussed. Then, the fundamental of parallel plate capacitive sensors, one of the main types of the chosen capacitive sensor, and the methods to improve its sensitivity are studied and presented. Furthermore, more information about the capacitive sensor is given, including the types of dielectric material and electrode material of capacitive sensors are discussed, and the introduction of the poly(glycerol sebacate), which is the base material of the dielectric layer in this project. Finally, the performances of capacitive sensors in some present studies are presented to be as a reference to compare with those of the PGS sensor in this project.

**In Chapter 3**, the material preparation, sensor assembly, and material and sensor characterization are presented. A wearable capacitive pressure/strain sensor was fabricated with poly (glycerol sebacate) (PGS) dielectric material. The microstructure inside the sensor was created by a salt-leaching method. In the material characterization, the methods of sample morphology, the mechanical behaviour and the electrical behaviour of the material are presented. For the sensor characterization, sensors' electromechanical behaviour, including sensitivity or Gauge Factor, response time and recovery time, static stability, electromechanical repeatability, long-term dynamic stability, and environmental behaviour, consisting of proximity and temperature sensitivity, are explained.

**In Chapter 4**, the results of the characterisation are presented. The PGS foam is studied first. Its morphology, mechanical behaviour and electrical behaviour are tested and analyzed. Then, the results of sensor characterization for the PGS dry sensor, PGS/EG sensor and the PGS<sub>40</sub>/EG<sub>60</sub> sensor are presented and discussed.

**Chapter 5** describes the possible applications and demonstrations of this PGS wearable sensor. With the pressure sensing ability, finger bending monitoring was achieved. With the capability to measure mild pressure/force, a heart beating demonstration to measure the tiny heaving of the vein was achieved; With good dynamic stability, the sensor was attached to the volunteer's 10<sup>th</sup> rib measuring the up and downs of the chest to show breathing patterns of human; With the temperature sensing function, it was used to measure the surface temperature of the item with hot and cold water pouring in to simulate the temperature change sensing in the tactile feeling; Its ability of weight measurements compared with a commercial load cell.

**Chapter 6** gives a conclusion of the whole project and lists the recommendations of the sensor for future work.

## Chapter 2 Literature review

### 2.1 Wearable Devices

#### 2.1.1 Introduction

The wearable device is a type of electronic device that can be directly attached to the body, worn as accessories, embedded in clothing, or implanted in the user's body [13, 14]. By attaching to the body, the devices could track and analyze users' data, such as body movements and vital signs, and send and receive these data via the Cloud or other methods. The usability of these devices falls into a wide range depending on the scope of work to which it belongs, such as health, fitness, or entertainment [15]. Currently, the wearable device has attracted great attention and it is at the forefront of the Internet of Things (IoT) (Figure 2.1).

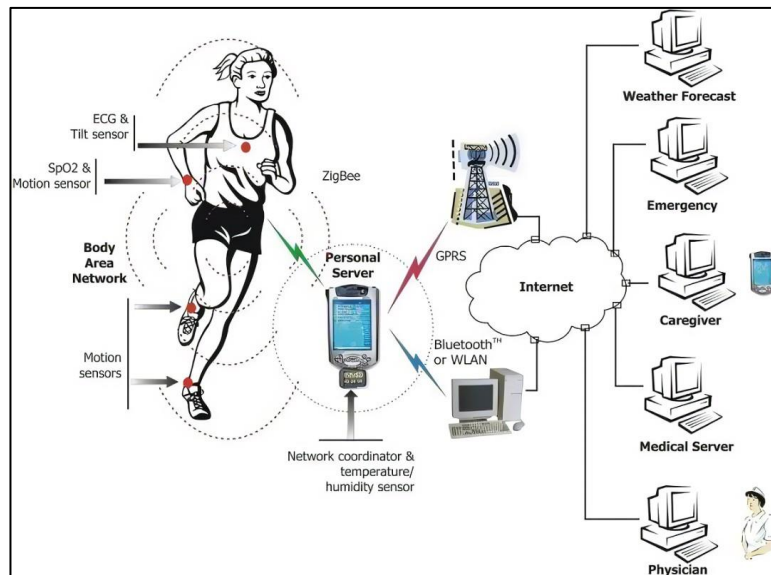


Figure 2.1 Wearable technology tracks users' data and transmits the data through Internet [16].

The development of wearable devices could date back to the first invention of a chest strap wireless ECG around 1980 [17, 18]. Since then, wearable technology has attracted significant interest from both academia and industry, and the publication on wearable electronics has increased from around 300 in 2009 to over 3,000 in 2017 [19]. Wearable devices have been applied in different fields. In the education and culture field, a doctor has used wearable devices (google glass) to receive additional clinical data to assist in guiding surgical activity [20-22]. In the social network field, people trained guide dogs with wearable electronics to provide more communication information to disabled people [22, 23]. Soldiers monitored their physical activity profile with wearable physical sensors, which could optimise their training volume, and recovery, among many others, improves the ability of accurate estimation and also lowers army financial burdens [22, 24].

The wearable devices used in health care are the focus of this thesis. Wearable devices in the form

of portable medical or health electronic devices could achieve real-time detection of patient physical signs, so as to provide exercise guidance and medication reminders [22]. Furthermore, the wearable device aims to achieve accurate and smart detection and analysis of human physiological and pathological information from outside of the hospital. This self-diagnosis and self-monitoring could also ease the burden on healthcare personnel, and people could use hospital resources for more emergent or responsive care [22, 25]. In Pang's review paper, the present wearable devices for health monitoring are divided into four main categories [26]:

- i. electronic artificial skin (e-skins),
- ii. wearable sensors for sensing human motion,
- iii. implantable devices, and
- iv. advanced sensors with additional features such as transparency, self-power, and self-healing [26].

### **2.1.2 E-skin, implantable devices, and other advanced devices with additional features**

The design and studies of e-skin were to mimic the human skin which has the ability of active tactile sensation, passive pressure, vibratory, and humid sensation to sense the various types of stimuli and know where and when they happened [26]. The research on e-skin was in some ways inspired by science fiction which gives people a great demonstration of how e-skin works. The early science fiction book about the e-skin was the novel *Cyborg* written by Caidin, and its TV show, *The Six Million Dollar Man* [27, 28]. This series showed the audience a superpower man owning a bionic replacement arm. Another example is the *Star War* series, one of the most popular sci-fi movies, depicts a scene where Luke Skywalker, the main character, was installed with an artificial hand with full sensory perception [28, 29].

Technological advancements in the e-skin emerged with the inspiration of Sci-fi products. One of the first real e-skins was presented by General Electric for a robotic arm using the flexible sheet attached with infrared sensors. This e-skin could sense the surrounding environment and react to and avoid potential obstacles. It achieved a simple human-machine interaction, such as dancing with a ballerina [30]. The current target of the e-skin is to achieve sophistication in sensing mechanical force and temperature, which are two significant parts of somatosensation, as well as to achieve stretchable, reliable, and user-friendly electronics.

There is a rapid development and innovation of e-skin in the last two decades. The initial version of e-skin fabricated by flexible organic transistors was proposed by Someya and coworkers [31]. They built a conformable and flexible net-shaped network structure of thermal and pressure sensors formed with an array of transistors fabricated on a polyimide film and pressure-sensitive rubber. This net-shaped sensor network could be attached to a round surface, like an egg and measure the pressure and temperature distributions. After this work, many e-skin studies based on various mechanisms and different functions appeared [32]. Suo et al. [33] presented stretchable electrical conductors with a stretchable Au film evaporated onto a flexible PDMS membrane. This stretchable

conductor could return a stable resistance signal up to a strain of 2%. Zhu et al. [34] developed a coaxial piezoelectric fibre using barium titanate (BTO) nanoparticles as the core component and PVDF polymer doped by graphene oxide as the shell (Figure 2.2 (a, i)). This e-skin achieved a sensitivity of  $10.89 \text{ mV kPa}^{-1}$  in the pressure range of 80 – 230 kPa. It could monitor joint movements such as wrist and elbow movement, and mapping tactile pressure (Figure 2.2 (a, ii and iii)). Katerinopoulou et al. [35] demonstrated a printable temperature sensor based on  $\text{CuFe}_2\text{O}_4$  (Figure 2.2 (b, i)). It showed a good temperature measuring performance in a range of 40 – 140 °C, which is similar to that of a commercial thermistor (Figure 2.2 (b, ii)), and it could detect the temperature change of a human hand (Figure 2.2 (b, iii)).

Currently, e-skins have the potential to be applied in many fields, such as flexible screens for touching sensing, humanoid robotics and prosthetics [26].

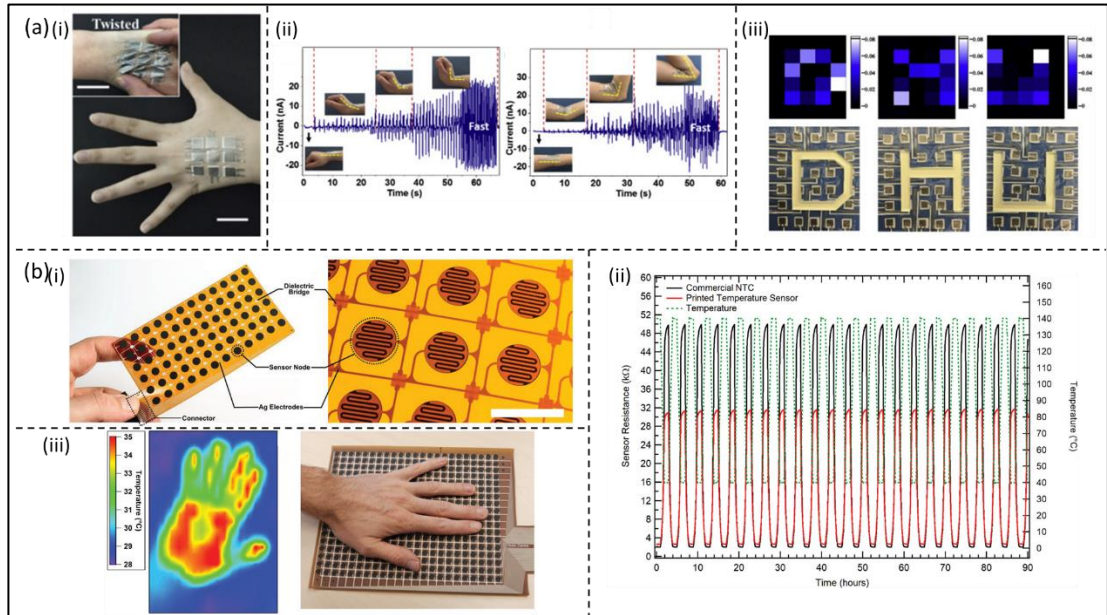


Figure 2.2 Various e-skins. (a) Zhu's piezoelectric fibre. (i) Photo image, (ii) Monitoring wrist and elbow bending, and (iii) tactile mapping (reprinted with permission from Ref. [34]). (b) Katerinopoulou's temperature sensor. (i) Photo image, (ii) temperature measuring ability compared with a commercial thermistor, and (iii) detecting the temperature of a human hand (reprinted with permission from Ref. [35]).

Implantable devices attach directly to organs inside the body and have the potential to monitor electrical signals from the inner body, including cortical and epicardial electrical signals [26]. As the organs inside the human body are very soft, the in vivo diagnostic devices are required to be minimally invasive and non-penetrating, and capable of covering a large measuring area with sufficient accuracy and spatial resolution [26]. Viveni et al. [36] developed a flexible, nonpenetrating electrode consisting of silicon nanomembrane transistors, and these transistors were made of flexible and high-quality single crystal silicon (Figure 2.3 (a, i)). This flexible electrode array could achieve a large-area coverage ( $\sim 80 \times 80 \text{ mm}$ ) while keeping a high temporal resolution ( $>1.2 \text{ kS s}^{-1}$ ), which enables the display of human brain dynamics during normal activity and disease conditions at the micro-scale (Figure 2.3 (a, ii and iii)). This technology provides a potential way to

monitor the spatiotemporal patterns of brain activity long-term in awake, acting animals and humans, which currently no existing tools could accomplish. Kim et al. [37] present a minimally invasive balloon catheter sensor integrated with serpentine-shaped interconnected electrodes, a PI tactile sensor and a Ti/Pt thin layer that served as temperature and flow sensors owning the function of measuring temperature, flow, tactile, optical and electrophysiological data (Figure 2.3 (b, i)). A clinical demonstration of the electrical signal and mechanical contact was measured on the surface of the beating heart, and the temperature monitoring before, during and after RF ablation (Figure 2.3 (b, ii and iii)), which demonstrates its specific utility in cardiac ablation therapy.

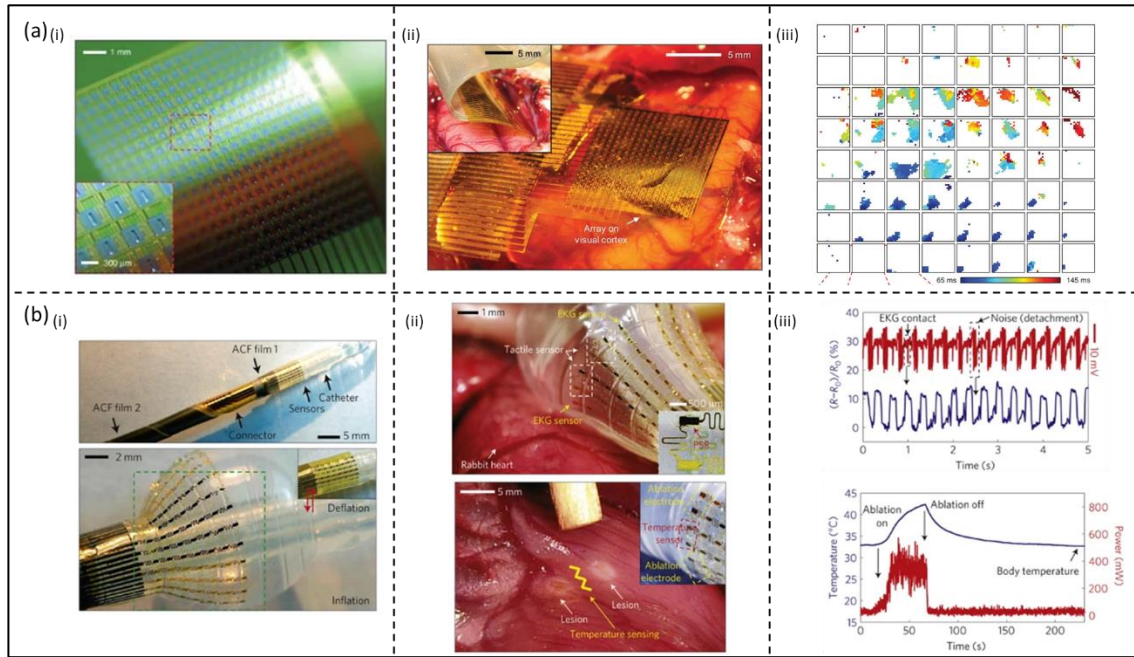


Figure 2.3 Present implant devices. (a) Viventi's flexible electrode array (reprinted with permission from Ref. [36]). (i) Photograph, (ii) Electrode array was placed on the visual cortex. (iii) 64-color map monitor presented the neural response to the stimuli. (b) Kim's balloon catheter sensor (i) in deflation and inflation states, (ii) measuring the heart condition and the epicardial ablation lesions, (iii) The record of the electrical signal and mechanical contact, and the temperature monitoring (reprinted with permission from Ref. [37]).

Many innovative ideas have been proposed regarding present sensing devices to apply them in more fields and various working scenarios. To mimic the self-heal function of the human skin, Tee et al. [38] utilized the self-heal function of the hydrogen bond of a supermolecular polymer network (synthesized from Empol 1016 and diethylenetriamine) and mix  $\mu\text{Ni}$  particles owning a thin native oxide layer, which allow the mixture to self-adhere to the flexible substrate. The self-heal ability was remarkable and did not influence the sensors' performances. After rupture, the sensor's conductivity could recover to 90% after 15 s recovery time, and the mechanical performances could completely recover after 10 min. To achieve a transparent device, Fan et al. [39] develop a flexible transparent nanogenerator with a transparent PDMS membrane sandwiched in two ITO-coated PET membranes. This device was attached to a smartphone and still showed a clear screen, and it also has a good mild force detecting ability which enabled it to sense the dropping of water and feather.



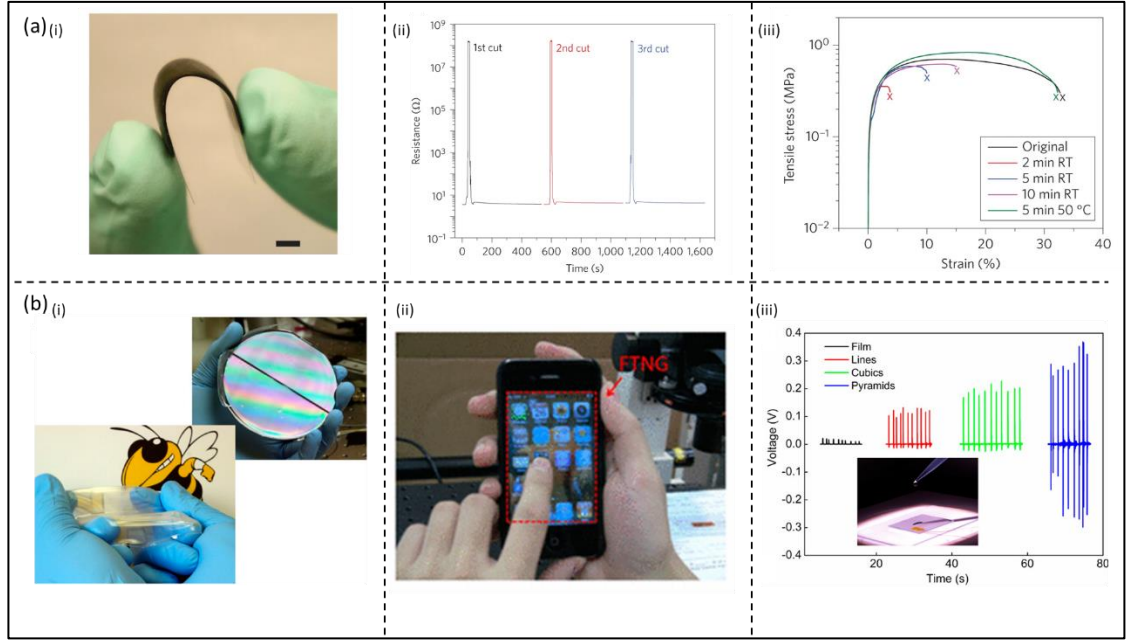


Figure 2.4 Some devices with unique functions. (a) Tee's self-heal sensor, (i) photo image. The recovery of (ii) conductivity performance and (iii) mechanical performance (reprinted with permission from Ref. [38]). (b) Fan's transparent sensor, (i) photo image (ii) attached to the screen of the phone (iii) Sensing the mild water drop (reprinted with permission from Ref. [39]).

### 2.1.3 Wearable Sensors

The wearable sensor is the main study topic of this thesis and will be discussed detailed. The function of wearable sensors has some overlaps with that of e-skin and many researchers actually mix these two concepts.

Similar to the above e-skin to simulate the mechanical and temperature sensing functions of the skin, wearable or skin-attachable devices are studied to detect complex body movements and in vitro diagnostics on human body parameters [26]. With the assembling of sensors, signal transmitters and signal receiving end, a wearable diagnostic or therapeutic devices system could realise a shift in the centre of medical diagnosis from hospitals and clinics to individual homes [26]. The human body conditions could be monitored remotely at any time and anywhere.

To monitor body movements and measure body parameters, wearable devices are required to be flexible and stretchable to withstand large deformation and needed to have high sensitivity to measure the mild or large deformation caused by body signs, like pulse and breath [40]. Many present wearable devices achieve high flexibility and stretchability. Yamada et al. [40] developed wearable devices made of thin films of aligned single-walled carbon nanotubes. An excellent stretchability of a strain up to 280% was achieved by the formation of a mesh structure with gaps, islands and bundles bridging the gaps when the nanotube fracture (Figure 2.5 (a)). Mattmann et al. [41] presented a wearable strain sensor combining 50 wt% of thermoplastic elastomer and 50 wt% of carbon black particles. This sensor was applied to measure the large strain and deformation of clothes capable of measuring a strain of at least 80%, and it could be washed several times in the



conventional washing machine without electromechanical (Figure 2.5 (b)).

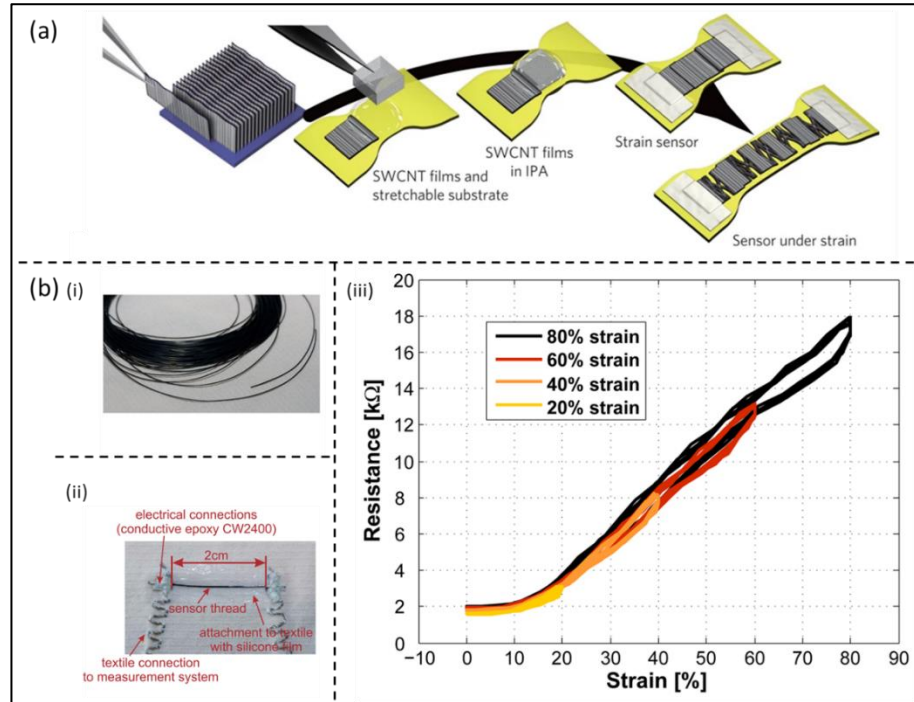


Figure 2.5 Some present wearable sensors showed good stretchability, (a) Yamada's wearable devices and the good stretchability mechanism of gaps, islands and bundles bridging (reprinted with permission from Ref. [40]). (b) Mattmann's strain sensor (i) Sensor thread; (ii) Sensor thread attached to clothes; (iii) Its good stretchability up to 80% strain (reprinted with permission from Ref. [41]).

Furthermore, wearable sensors are required to have good performance in measuring different parameters, such as high sensitivity, low hysteresis, rapid response time, good repeatability and long time stability. For example, the application of wearable sensors in the biomedical field is expected to be capable to detect the vital signs of the human body and to aid in the analysis of the patient's health status. The four main vital signs are body temperature, breathing rate, blood pressure and pulse rate [42]. Noteworthy, most of the present wearable sensors to measure vital signs are capacitive sensors capable of detecting mild pressure and deformation. Sharma et al. [43] reported a wearable capacitive pressure sensor by blending the MXenes ( $\text{Ti}_3\text{C}_2\text{Tx}$ ) with poly(vinylidene fluoride-trifluoroethylene) (PVDF-TrFE) by an electrospinning process. This wearable device achieved a high sensitivity of  $0.51 \text{ kPa}^{-1}$  and a low pressure detection limit of  $1.5 \text{ Pa}$  which help it be capable to detect the pulse with three peaks and the respiration pattern. Kim et al. [44] developed a soft capacitive pressure sensor using a wrinkled Au thin film on top of an elastomer as a stretchable electrode and compared this sensor with the FDA-approved blood pressure measuring device (Clearsign device). Their sensor could detect the arterial pulse pressure clearly and this could help to track and detect the nominal changes in systolic, diastolic, and mean arterial pressure, with a high correlation between the Clearsign device. The rapid response time and high sensitivity made it capable of detecting specific features, such as the late systolic peak, in its clear pulse waveform which is not easy to be detected in Clearsign devices.

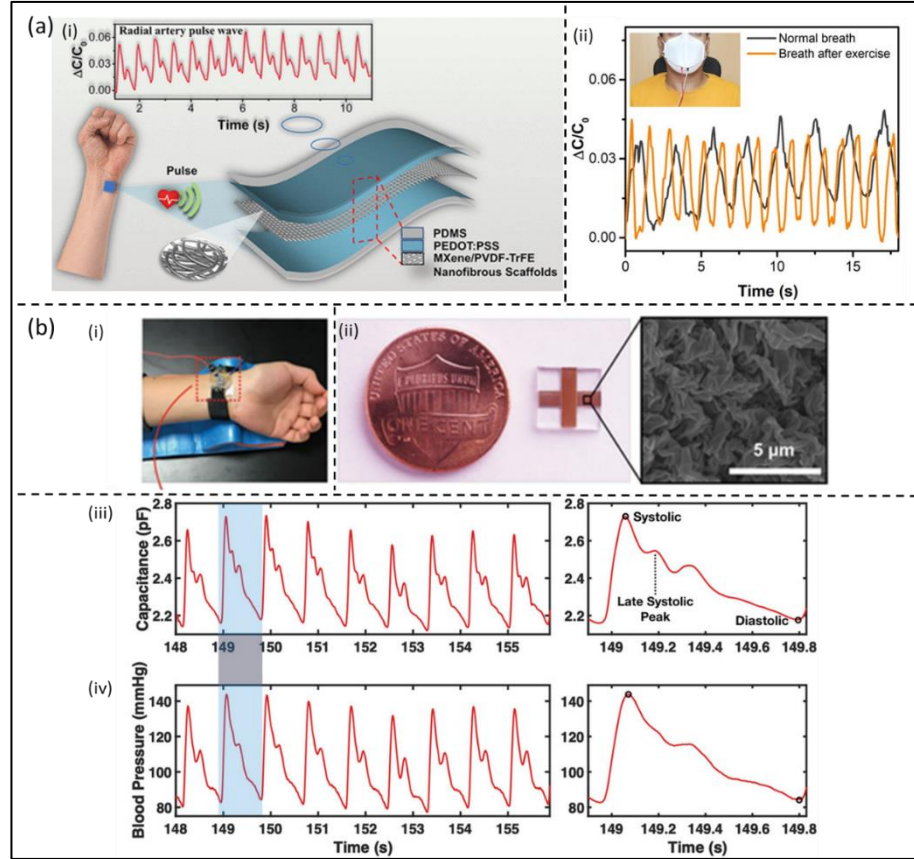


Figure 2.6 Some present wearable sensors showed good sensitivity; (a) Sharma's capacitive sensor; (i) detecting the pulse and, (ii) respiration pattern (reprinted with permission from Ref. [43]). (b) Kim's capacitive pressure sensor, (i) Attached on the wrist; (ii) Size and microstructure; (iii) sensor's pulse waveform; (iv) pulse waveform from ClearSight device (reprinted with permission from Ref. [44]).

Besides the vital signs, other physiological signals are also studied and measured by the wearable sensor. According to Omer et al. [42]'s review about health monitoring, they classify the physiological signal into four categories, which are (1) biochemical signals, based inbody secreted chemical compounds such as lactic acid in muscles, (2) body electrical signals, which control the body's movement and activity such as electrocardiogram (ECG), electroencephalogram (EEG), electrooculogram (EOG), mentioned at the beginning, (3) the kinematic signals, which is the body movement e.g. the movement paths and speed of arms and legs, (4) the physical signals, which are the four vital signs mentioned in the previous paragraph. In these four types of signals, the biochemical signals are chemical properties rather than electrical signals or mechanical deformations, so they are not the measurement target of the wearable sensor. For the electrical signal measurements, the Smart Wearable Systems (SWS) (Figure 2.7) [42], which are a network of several electrode sensor nodes, could provide the ECG and also other parameters like body temperature, and pulse, among many others. However, this electrode sensor network was not a pressure/strain measurement, either.

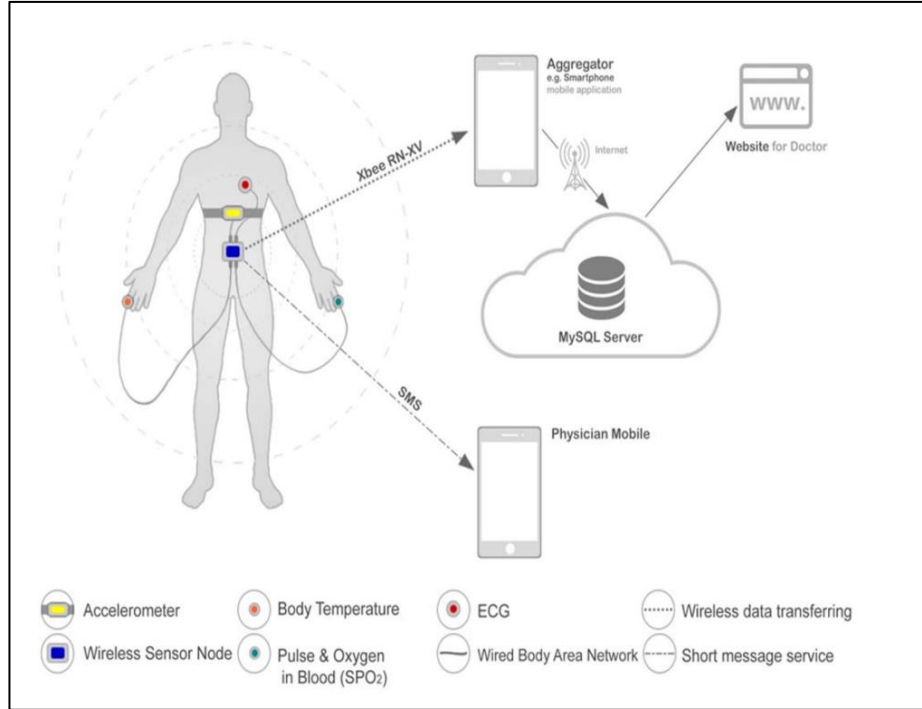


Figure 2.7 The SWS provides could provide the electrical signal of the body and also other parameters (reprinted with permission from Ref. [42]).

For the kinematic signals, many studies about wearable sensors demonstrate good performance for the measurement of body movement or other pressure signals. Jung et al. [45] developed their sensor with a dielectric layer of a composite of PDMS and thermoplastic resin microspheres, and this sensor measured the finger bending angle accurately. Wang et al. [46] reported a wearable sensor with a bionic Komachi konbu structure and a dielectric material of PDMS, and this sensor could record the finger tapping on the touchpad of a laptop, the real-time finger bending and the finger power to lift cups with different weights. Besides the finger bending, the foot, leg and arm movement parameters were also measured in the separate works from Jung [45], Chen [47], and Yang [48]. Jung et al. [45] measured the pressure of a part of the foot during walking and running (Figure 2.9 (a)), Chen et al. [47] measured the pressures of seven different areas of the foot (Figure 2.9 (b)), and Yang et al. [48] measured the pressures from the front sole and heel (Figure 2.9 (c)). Yang et al. [48] also attached their sensor to the elbow and knee to detect the movement of arms and legs.

In summary, wearable sensors could be applied in real-time body monitoring, advanced therapies, and diagnostics, among many others [26]. The portability and convenience of the wearable sensors give individuals the opportunity to know their body health status and adjust their lifestyle on time, which could reduce the possibility of disease and reduce the burden on health services worldwide [49].

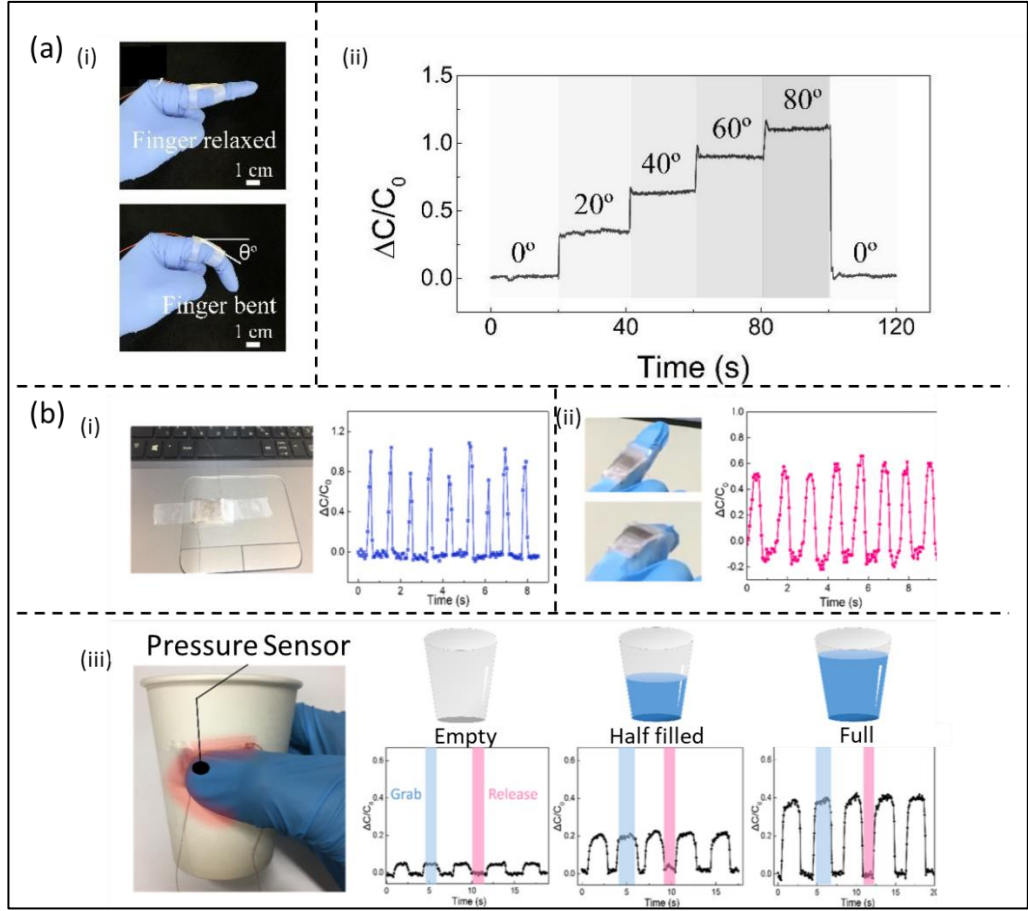


Figure 2.8 Some present wearable sensors to measure finger bending movement, (a) Junh's sensor measured the finger bending angle (reprinted with permission from Ref. [45]). (b) Wang's sensor recorded (i) finger tapping on the touchpad of a laptop, (ii) the real-time finger bending, and (iii) the finger power to lift cups with different weights (reprinted with permission from Ref. [46]).

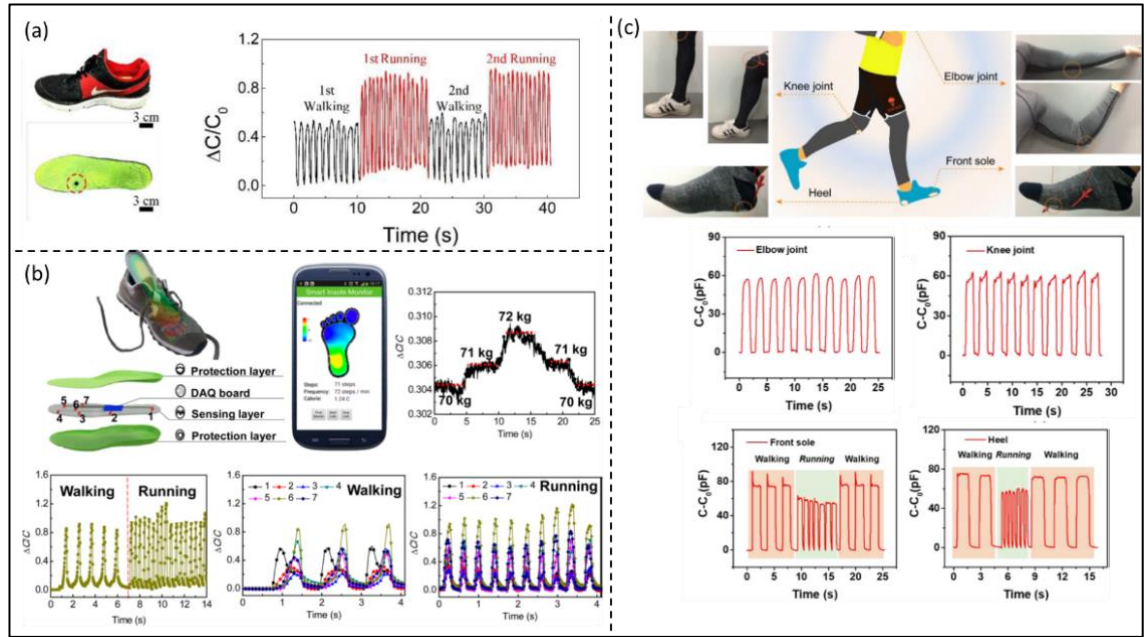


Figure 2.9 Some present wearable sensors to measure foot pressure, and leg and elbow movement, (a) Jung's sensor measured the pressure of a part of the foot during walking and running (reprinted with permission from Ref. [45]); (b) Chen's sensor measured the pressures of seven different areas (reprinted with permission from Ref. [47]); (c) Yang's sensor measured the pressures from the front sole and heel and detected the movement of arms and legs (reprinted with permission from Ref. [48]).

## 2.2 Wearable Pressure/strain Sensor and Their Working Principles

To monitor the body signs and movements, wearable sensors are required to have the capability to sense the pressure or deformations that these movements cause. The wearable pressure/strain sensor is the mainstream of wearable sensor studies because they are simple to fabricate and could detect the mild pressure/deformation of body skin caused by pulse, breath, and body joint movement, among many others. The present wearable pressure/strain sensors are mainly piezoresistive, piezoelectric or capacitive sensors.

### 2.2.1 Piezoresistive Sensor

The mechanism of the piezoresistive sensor is the piezoresistive effect. The pressure/stress being applied to the sensor causes a change in the length of the sensor which leads to a change in resistance. By quantifying this change, the pressure data could be obtained.

The functional part of piezoresistive sensors mainly consists of conductive fillers and stretchable substrates, such as some metals and alloys, semiconductors, and elastomeric matrix, among many others [50, 51]. Metals and alloys have a limited Gauge Factor of around 3 [52], and they are rigid and have limited stretchability, while flexible piezoresistive nanocomposites made from the soft elastomeric matrix (PDMS, Ecoflex, among many others [51]) filled with a conductive reinforcement conductive material like MWCNTs, graphene, Au or Ag nanoparticles and



nanowires, have higher stretchability (more than 20% strain) and Gauge Factor that could reach 20 – 30 [53] or Sensitivity of 15 - 20 kPa<sup>-1</sup>. Park et al. [54] present a piezoresistive sensor fabricated by a mixture of CNTs and PDMS with interlocked microdome arrays (Figure 2.10 (a, i)). This sensor had a great sensitivity of 15.1 kPa<sup>-1</sup> and a low pressure detection of 0.2 Pa which made it capable of monitoring human breathing flow through a breathing mask and throat vibration during speaking (Figure 2.10 (a, i&ii)). Jian et al. [55] reported a piezoresistive sensor with aligned carbon nanotubes/graphene hybrid films as the active material and microstructured PDMS films as the flexible substrate (Figure 2.10 (b, i)). The sensor achieved a high sensitivity of 19.8 kPa<sup>-1</sup> under the pressure of 0.3 kPa and a minimum detection limit of 0.6 Pa. It could detect bending and torsional forces (Figure 2.10 (b, ii&iii)), and recognise the different degrees of vibration while speakers said different syllables of different words (Figure 2.10 (b, iv)).

Piezoresistive sensors have a relatively high sensitivity or Gauge Factor. However, with a high GF, these sensors show high nonlinearity between the resistance output signal and stress input, and the conflicting relationship between “high sensitivity” and “high linearity” is the main problem that needs to be addressed with this type of sensor [50].

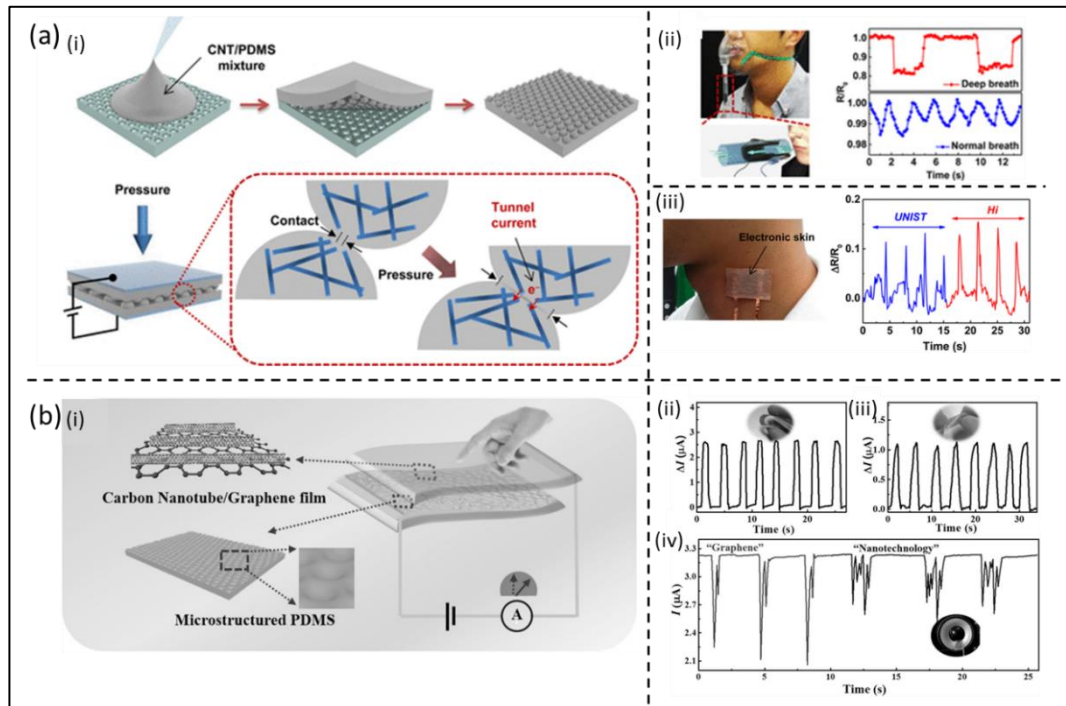


Figure 2.10 Some present wearable piezoresistive sensors. (a) Park's sensor, (i) sensor's structure, (ii) Monitoring human breathing flow through a breathing mask, and (iii) Throat vibration during speaking (reprinted with permission from Ref. [54]). (b) Jian's sensor, (i) sensor's structure (ii) Bending and (iii) torsional forces, and (iv) Recognising the different degrees of vibration (reprinted with permission from Ref. [55]).

### 2.2.2 Piezoelectric Sensor

The piezoelectric effect is a phenomenon that when a dielectric is deformed (including bending and stretching deformation), charges are generated on its surface, thereby generating a voltage that

changed due to the change in deformed volume. By measuring the generated voltage, a calibrated deformation or pressure could be obtained. When stress is applied to a dielectric, the dielectric deforms and its dimensions change. The resulting change in dimension shifts the centres of mass for positive and negative ions, which generate a dipole. The dipoles inside the material cancel each other out, but the dipoles on the surface are not cancelled out, generating a polarity given by [56-58].

The materials owing piezoelectric effect are mainly two types, organic polymers and inorganic ceramics [51]. The organic polymers can be poly(L-lactic acid) (PLLA), poly(D-lactic acid) (PDLA), and polyvinylidene fluoride (PVDF) [51], those materials realize the piezoelectric effect through the mechanism described above. The inorganic materials, for instance, lead zirconate titanate (PZT) [59], zinc oxide (ZnO), aluminium nitride (AlN), lithium niobate (LiNbO<sub>3</sub>), barium titanate (BaTiO<sub>3</sub>), among many other materials [51]. Dagdeviren et al. [59] developed a piezoelectric sensor using PZT as the active component and connecting with a SiNM n-MOSFET amplifier to amplify the piezoelectric voltage response and these components were mounted on an Ecoflex film substrate (Figure 2.11 (a, i)). The sensor owned a dynamic sensitivity of 0.005 Pa and a fast response time of 0.1 ms, and it could show a clear signal monitoring the three peaks of the wrist pulse which help to obtain the radial artery augmentation index and pulse pressure velocity (Figure 2.11 (a, ii)). Zhong et al. [60] built a piezoelectric sensor with a size customizing function based on a PP piezoelectret film sandwiched between two electrodes printed on two pieces of paper (Figure 2.11 (b, i)). The sensor array showed a dynamic sensitivity of 0.35 V/N and has good pressure measuring function to act as a calculator (Figure 2.11 (b, ii)). The sensor could remain functional even when partial areas were cut down (Figure 2.11 (b, iii)).

The piezoelectric sensor has the advantage of a simple sensor structure, a low-material cost, low power consumption, and fast response time [61]. Its limitation is that it can only be used for dynamic pressure measurements [61].

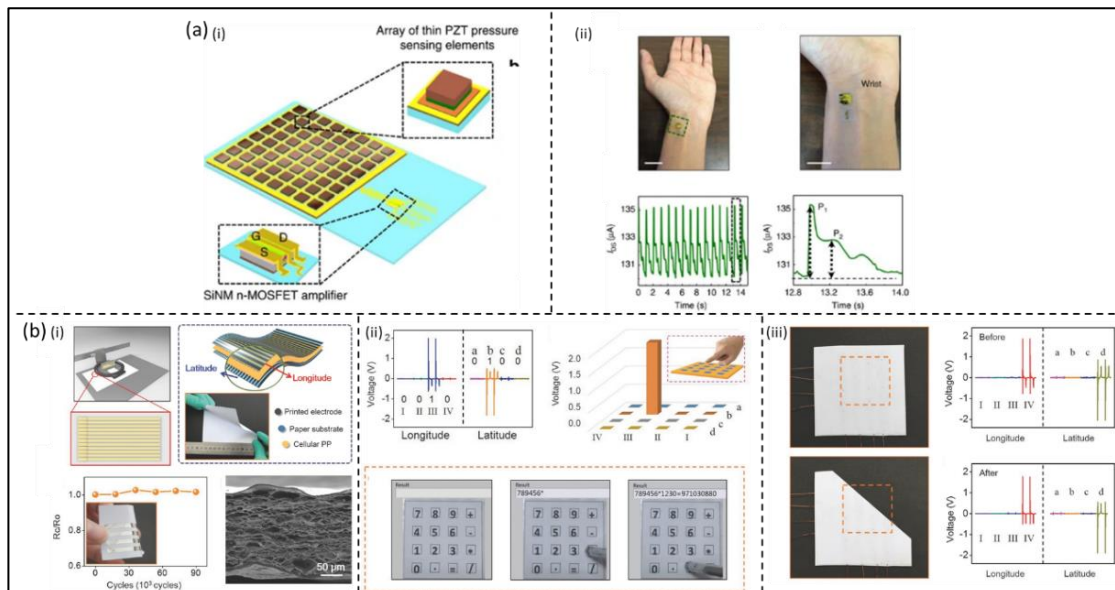


Figure 2.11 Some present wearable piezoelectric sensors. (a) Dagdeviren’s sensor, (i) sensor structure, (ii) attached on the wrist, and (iii) monitored the pulse signal (reprinted with permission from Ref. [59]). (b) Zhong’s sensor, (i) sensor structure, (ii) sensor pressure array functions as a calculator, and (iii) The sensor’s function remain while being cut down (reprinted with permission from Ref. [60]).

### 2.2.3 Capacitive Sensor

The parallel-plate capacitive sensor is the main type of capacitive sensor. Capacitance refers to the ability to store the charge between two electrodes of the capacitor while a voltage or electric field is applied across the capacitor. A sensor with a large capacitance can store more charges inside it [62].

The capacitive sensor is to utilize its properties that the capacitance value changes as the distance change between its two electrodes. When mechanical stress is applied, the distance between the two electrodes will change, which promotes a quantifiable capacitance variation that can be later used to monitor pressure or strain changes.

Capacitive sensors are made by insulative materials, e.g. PDMS [45-47, 63-82], poly(vinylidene fluoride) (PVDF) [43, 77, 83, 84], polyurethane (PU) [85, 86], polyethylene glycol terephthalate (PET) [45, 46, 87], polyethylene [88], Ecoflex [89, 90], hydrogels [91], graphene oxide-enhanced foam-like paper, among many other insulative material.

Compared with other types of pressure sensors, the capacitive one has high linearity between the capacitance signal and stress, which means it could measure pressure inputs with great accuracy and with less noise. It also has a mild detect limit and small hysteresis. However, its relatively low sensitivity is the present challenge that researchers trying to address.

### 2.2.4 Comparison between Different Sensors

Comparing these three types of sensors, the piezoresistive sensor has high sensitivity and a wide range of pressure detection and monitoring, but its low linearity is difficult to handle and the high power consumption could be a disadvantage for wearable applications. The piezoelectric sensor has low power consumption and facile material preparation method, but it can only be used for dynamic sensing.

Compared with the other two sensor mechanisms, capacitive sensors have the benefits of excellent linearity, fast response time, small hysteresis, and low power consumption, both in dynamic and static pressure applications [92], which is ideal for the wearable sensor which is required to let people know the body parameters accurate and in a real-time and easy to implement at industrial scale.

Table 2.1 Comparison of different types of sensors.

Sensor Types	Advantages	Disadvantages
Piezoresistive	Simple sensor structure; Wide range of pressure detection; High sensitivity [61, 84, 93, 94].	Low linearity; High power consumption [61, 84].



Piezoelectric	Low cost; fast response time; Low power consumption [61, 94, 95].	Dynamic pressure sensing only [61].
Capacitive	Excellent linearity; small hysteresis; wide dynamic range [92]; Low power consumption [61, 84].	Hard to achieve high sensitivity.

### 2.2.5 Fundamentals of a Parallel Plate Capacitor

The parallel plate capacitor is the main study focus in capacitive sensors and the focus in this study. As shown in Figure 2.12, the structure of a parallel plate capacitor can mainly be divided into two parts: dielectric layers and electrode layers [96]. Dielectric layers are made from insulative materials that are able to store the electrical charge. Under the external electrical field, the dielectric polarization occurs, and the electrical energy is stored in the capacitor. Electrode layers, or electrodes, are conductive plates connected with a power supply that generates an electric field and measure the capacitance change. Owing to the function of generating an electric field, the electrode materials are required to have good electrical conductivity.

For a parallel plated capacitor, three significant aspects are required to be known. First of all, the mechanism of capacitors is through dielectric polarization. By dielectric polarization, the capacitor generates an inner electrical field and stores charge to form the capacitance. Secondly, the ability to store charge is called capacitance, and the magnitude of capacitance depends on the dielectric permittivity of the material. Thirdly, one significant performance of a capacitor is its dielectric loss, which could cause the loss of stored charge over time.

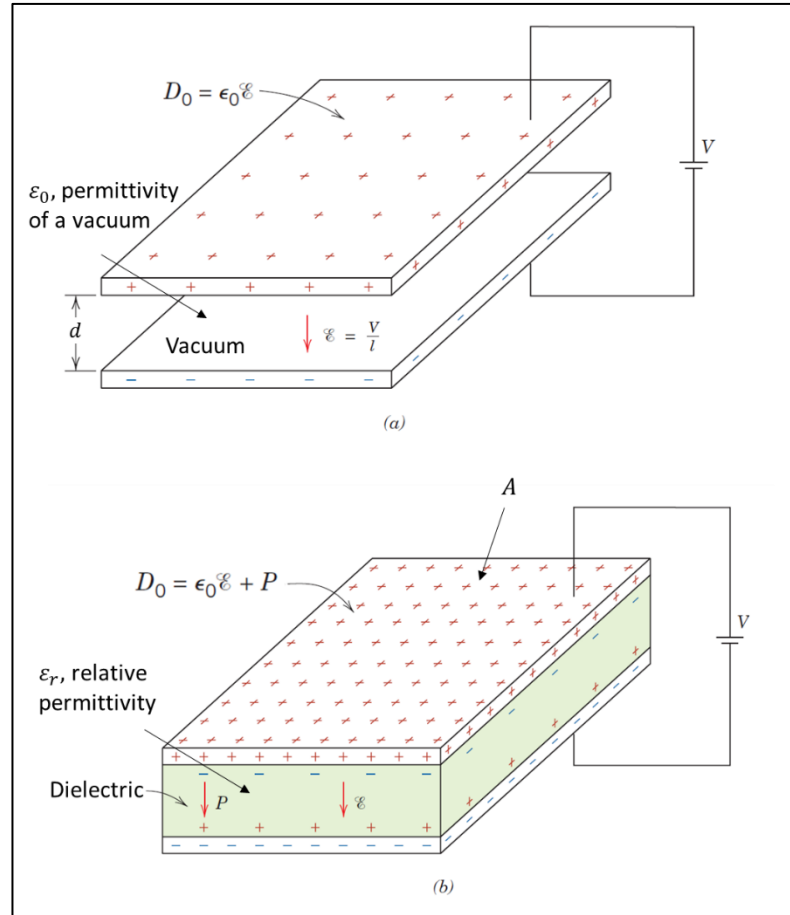


Figure 2.12 Parallel Plate Capacitor.

#### 2.2.5.1 Principles of Dielectric Polarization and Capacitance

Dielectric polarization is the mechanism that gives a capacitive sensor the ability to store the charge and generate capacitance. When a dielectric is placed in an electrical field and the non-conductive dielectric shows electrical properties is called polarization. An ideal dielectric is non-electrical conductive and there are no free electrons inside. Only positive and negative bound charges exist inside the dielectric and their centre of charge coincides with each other causing the charges to cancel out everywhere and the resultant no electrical properties are displayed macroscopically.

When an external electrical field is applied to the dielectric material, the centre of a symmetrically charged nonpolar (a positive charge and a negative charge) molecule shifts and an electric dipole is formed (Figure 2.13), and this phenomenon is called the (displacement) polarization. This polarization caused the electric dipole to arrange in the direction of the external electric field (positive charges are aligned with the electric field and negative charges aligned in the opposite direction [97]), and an electric field opposite the polarity of the source appears and the charge accumulates on the surface of the plates (for every free electron that leaves the positive plate to the power source, one electron accumulates on the negative pole). In this process, the energy from the power source in this process of the voltage and the electrical field is stored in the capacitor, and this

is called capacitance.

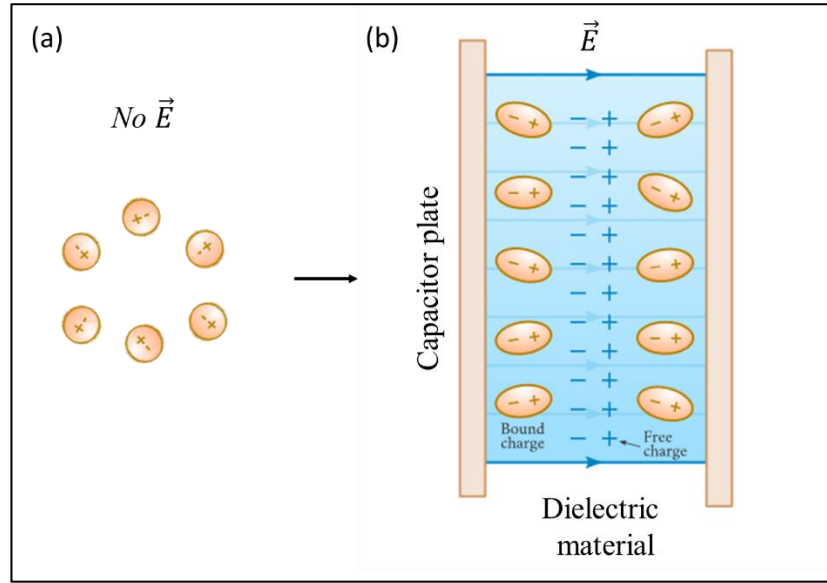


Figure 2.13 Dielectric polarization, (a) the centre of charge coincides with each other; (b) the centre of a symmetrically charged nonpolar molecule shifts [97].

#### 2.2.5.2 Equations for Capacitance and Permittivity

The capacitance of the parallel plate capacitor is shown in Equation 2.1.

$$C = \epsilon \frac{A}{d} \quad \text{Equation 2.1}$$

where  $\epsilon$  is the permittivity or dielectric constant of the dielectric,  $A$  is the area of electrodes facing each other and  $d$  is the distance between two electrodes.

When a dielectric material is placed between two electrodes (Figure 2.12 (b)), the permittivity of the dielectric can be calculated by

$$\epsilon = \epsilon_r \epsilon_0 \quad \text{Equation 2.2}$$

where  $\epsilon_0$  is the permittivity of vacuum, which is a universal constant equal to  $8.85 \times 10^{-12}$  F/m,  $\epsilon_r$  is the relative permittivity or dielectric constant of the insulative material ( $\epsilon_r$  will all be referred to as the permittivity in the later explanation). Permittivity is a significant parameter of capacitors or capacitive sensors to characterize the electrical properties of dielectric or insulating material. It is a measure of the ability of a substance to increase the capacitance of a capacitor compared with a vacuum condition, indicating the relative ability of the dielectric to store electrostatic energy under an electric field. The permittivity increases as the dipole moment and polarisability of the molecule increase, and can be used to determine the polarity of a polymer material.

#### 2.2.5.3 Dielectric Loss

A real capacitor can not achieve absolutely insulated and there are still free electrons passing

through the dielectric which causes its stored electrical energy to dissipate, a phenomenon known as dielectric loss [98].

The interior of an ideal capacitor is a dielectric with no free electrons, so it is impossible to generate charge movement, i.e. current [99]. However, any real dielectric is not absolutely insulating, and they still have some free electrons and consequently some ability to conduct electricity, so there is a leakage current in any capacitor.

In an alternating electric field, the free electrons generate conducted current (leakage current) under the external electrical field. They consume partial electrical energy stored in the capacitor and transfer this energy to heat energy, so the dielectric itself heats up and dielectric loss occurs. Dielectric loss can be divided into polarization loss (or dielectric loss) and conduction loss [100] (there is also loss related to the resistance of the metal part of the capacitor, but this does not belong to dielectric loss, so this will not be discussed here). The former is caused by the polarization of various dielectric causing current, which is related to the relaxation of the polarization.

While applying an electric field to an actual dielectric, the polarization process of the dielectric is not instantaneous but lags behind the voltage, this lag is usually caused by the required time of the polarisation of the dipole and the polarisation of the space charge, and this is the relaxation of polarization. The latter arises due to the current caused by the leakage current, which is related to the free charge [101]. In this way, the equation of relative permittivity can be represented as a complex description,  $\epsilon_r^*$ , of relative dielectric permittivity as the real component and relative dielectric loss as the imaginary component (Figure 2.14):

$$\epsilon_r^* = \epsilon_r' - i\epsilon_r'' \quad \text{Equation 2.3}$$

where  $\epsilon_r'$  is the real component of relative permittivity,  $\epsilon_r''$  is the imaginary component of relative permittivity which represents the dielectric loss [102],  $i$  is the imaginary unit,  $i^2 = -1$ .

With the help of complex permittivity, capacitance can be also described as a complex number  $C^*$ :

$$C^* = C' - iC'' \quad \text{Equation 2.4}$$

where  $C'$  is the real component of the complex capacitance, which means the net electrical energy stored and  $C''$  is the imaginary component of the complex capacitance which represents the capacitance loss due to the dielectric loss [103]. The complex format can also be described by the loss angle.

The loss angle,  $\delta$ , is the angle between the current density and displacement current density. It can be used to quantitative analyze the loss performances of dielectric material [102]. The  $\epsilon_r^*$  and the  $\delta$  can describe each other by:

$$\epsilon_r^* = \frac{\vec{D}}{\vec{E}} = \frac{D}{E} (\cos \delta - i \sin \delta) \quad \text{Equation 2.5}$$

$$\text{so,} \quad \tan \delta = \frac{\varepsilon_r''}{\varepsilon_r'}, \quad \varepsilon_0 \varepsilon_r' = \frac{D}{E} \cos \delta, \quad \varepsilon_0 \varepsilon_r'' = \frac{D}{E} \sin \delta \quad \text{Equation 2.6}$$

where  $\vec{E}$  is the external electrical field vector,  $\vec{D}$  is the displacement current density vector,  $E$  and  $D$  are the amplitudes of these two vectors [104].  $\vec{D}$  is the change of  $D$  over time. As there is no physical conduction in a capacitor, to make sure the current flows constantly in a circuit, the term of displacement current density,  $D$ , was introduced by Maxwell [105].

As the focus of this project is to study the capacitance change of the capacitive sensor rather than its energy-storing performance, the dielectric loss will not be discussed in the later discussion.

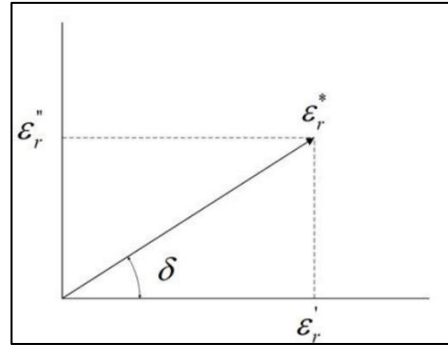


Figure 2.14 Definition of complex relative permittivity (reprinted with permission from Ref. [103]).

## 2.2.6 Methods to Improve the Performances of Capacitive Sensors

As mentioned in subchapter 2.2.3, the capacitive sensor had a problem of low sensitivity, which is almost the most important performance for the pressure/strain sensor. In this way, many present researchers are trying to find the proper methods to improve the sensitivity of the capacitive sensor.

### 2.2.6.1 Micro-structure

One way to improve the sensitivity ( $S$ ) of the capacitive sensor is to introduce the microstructure. Micro-structure improves  $S$  from two perspectives: first, the various microstructures give dielectric material a low Young's modulus [67] and a low stiffness [45]. The sensor has more space/distance to compress and has a bigger capacitance change value. Secondly, the air in the microstructure has a relatively lower dielectric constant. When the air is expelled, the total dielectric constant is increasing, and the capacitance change is higher. Various methods of producing microstructured dielectric layers have been reported, such as the template method [106], phase separation [45], and gas foaming [106].

#### 2.2.6.1.1 Template Method

The template process can be achieved by two methods. The first is to mix the porogen with the polymer evenly, then use physical or chemical methods to remove the porogen to create air voids in the sensor material. The most popular and easy example is to use sodium chloride (NaCl) or sugar porogen as the porogen and use water as the solvent to dissolve and remove them after the polymer

is solidified. Young et al. [45] filled the PDMS & microsphere (MS) composite with the sugar cubes; Jian et al. [46] mixed the instant sugar/salt solution and PDMS; Wei et al. [67] mixed PDMS-carbon conductive paste composite with NaCl (Figure 2.15 (a)); Siming et al. [74] mixed dry ground sugar particles with PDMS base gel and a curing agent; Kim et al. [75] mixed perfluorocarbon with PDMS pre-polymer; Sharma et al. [78] mixed zinc oxide (ZnO) hemisphere with PDMS and use a continuous centrifugal force to generate a gradient in porosity and pore size (ZnO was removed by hydrochloric acid, HCl) (Figure 2.15 (c)); Sujie et al. [47] mixed PDMS pre-polymer and its curing agent with ammonium bicarbonate ( $\text{NH}_4\text{HCO}_3$ ) (the sample was annealed to cure the PDMS pre-polymer and decompose the  $\text{NH}_4\text{HCO}_3$  into  $\text{NH}_3$ ,  $\text{H}_2\text{O}$  and  $\text{CO}_2$  gas). In these studies, the mixing method can be ultrasonic agitation [74, 107, 108], using mechanical mixers [75], or manually stirring. After mixing the polymer with porogen followed by curing, the porogen was removed by dissolving in water or other suitable solvents and dried or freeze-dried to preserve the porous structure of the material.

The second template method is called the reverse template/mould process or the two-step template method [109]. To mimic the shape of the desired part, the item is attached to a readily moulded material, e.g. silicon [76], to create a reverse template or the first template. Then, this reverse template is used to mimic the final of the material. The reverse templating process can also be achieved by 3D printing technology [45]. Mahata et al. [108] fabricated a polymethyl methacrylate (PMMA) inverse mould using rose petals as the base material and formed the shape of the PDMS sensor (Figure 2.15 (d)). Luo et al. [76] used a Si reverse mould to create PDMS pyramids-shape microstructure film. Kim et al. [75] mixed perfluorocarbon (a sacrificial solvent with a higher boiling point than PDMS) with PDMS pre-polymer and warmed the composite to remove the porogen solvent. Then, they used an opaque glass plate mould to create the microstructure for the surface of porous PDMS. Due to porogen material being common, the mixing and separating methods are easy to operate and the final sensor material had good hydrophobicity, flexibility, and thermal stability, and the whole process was low cost.

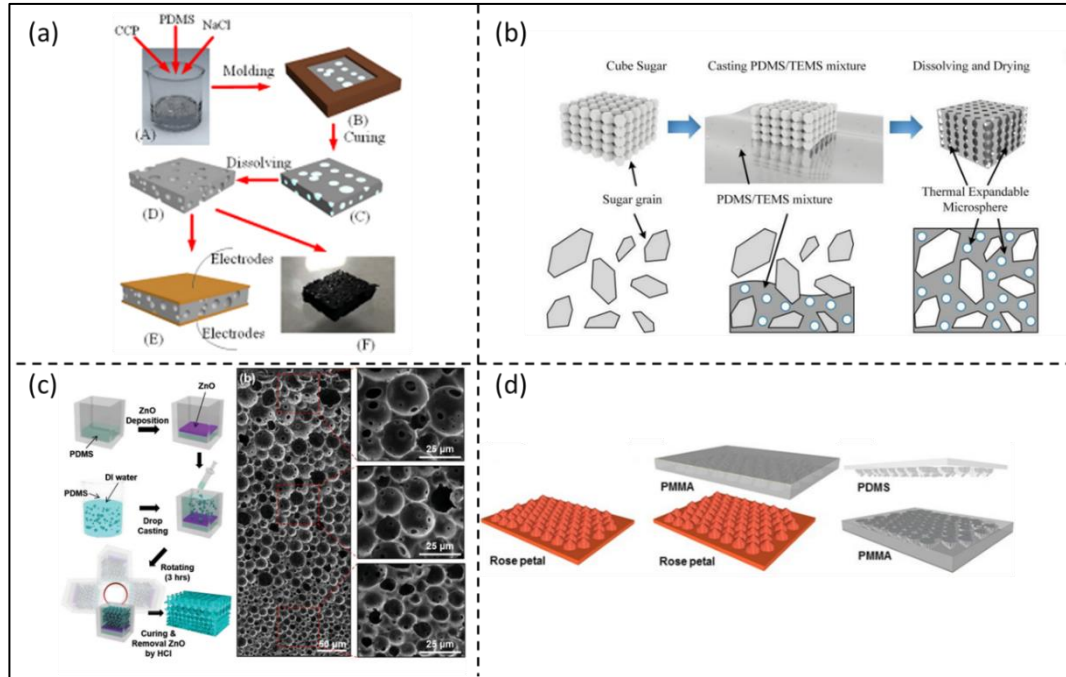


Figure 2.15 Present research using templating Method to create microstructure. (a) Wei used NaCl to create air voids in PDMS (reprinted with permission from Ref. [67]); (b) Jian filled the PDMS/MS composite into a sugar cube (reprinted with permission from Ref. [46]); (c) Sharma mixed the ZnO hemisphere with PDMS and use a continuous centrifugal force to generate a gradient in porosity and pore size (reprinted with permission from Ref. [78]); (d) Mahata applied a rose petal reverse mould template (reprinted with permission from Ref. [108]).

#### 2.2.6.1.2 Phase Separation

The phase separation method is a common process in the polymer foam field. It means the separation of two distinct phases from a single homogenous mixture, e.g. oil and water mixture. Two types of phase separation processes are discussed here. Thermally-induced phase separation (TIPS) is to add porogens with a high boiling point into the polymer, and the system forms a homogeneous system via heating and melting. Then, lowering the temperature causes the polymer to separate from the solvent and generates a phase, so the porogen could be extracted with organic solvents.

Non-solvent induced phase separation (NIPS) involves mixing the polymer and the solvent to form a homogenous solution, and the solution is leached away by adding extractant, which is more miscible with the solvent, into the solution to dissolve the solvent, and the porous polymer structure is generated. For NIPS, Danesh et al. [110] prepared a microporous composite film using Poly(methyl methacrylate) (PMMA), ethyl acetate (EA), and 2-methyl-2,4-pentaanediol (MPD) as their base material, solvent, and non-solvent separately. The homogenous solution consisted of these three components, and after the solvent evaporated, the non-solvent MPD was extracted by immersing the films in an aqueous methanol solution. For TIPS, Ishigami et al. [111] analyzed the solidification behaviour of poly(vinylidene fluoride) /Glycerol triacetate (PVDF/GTA) solution and used glycerol as the non-solvent (Figure 2.16). The sample was heated on a hot stage at 150 °C. According to the cooling process in Figure 2.16, the system was homogenous when it cool down to 115 °C. When PVDF/GTA/glycerol system reached its crystallization point, 102 °C, the polymer-

lean phase which represented the glycerol showed up, and the glycerol can be removed by extractant to get the porous PVDF/GTA.

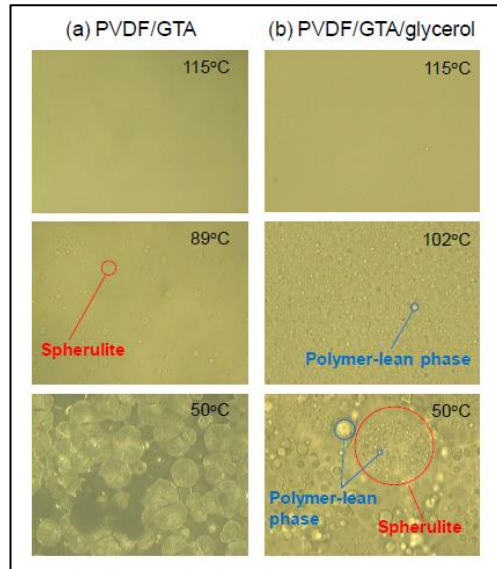


Figure 2.16 Ishigami et al. cooled down the PVDF/GTA/glycerol and the non-solvent glycerol showed up (reprinted with permission from Ref. [111]).

#### 2.2.6.1.3 Gas Foaming

In the gas foaming methods, the gas was blown into the samples to form the air void. Salerno et al. [106] designed a porous scaffold using poly ( $\epsilon$ -caprolactone) (PCL)/ thermoplastic gelatin (TG) blends. The porous structure was formed by solubilizing the blend in an  $N_2/CO_2$  pressure vessel. When it reached the foaming temperature and the pressure was released to ambient pressure, the nucleation and growth of the gas bubble started.

#### 2.2.6.2 High-dielectric material

To improve the performances of the dielectric materials, especially sensitivity, specific materials or fillers, which have high dielectric properties, can be mixed into the insulative matrix. Ionic liquids (ILs) are commonly used to improve the dielectric properties of the material. ILs are liquids formed by melting pure salts which have high melting points. They consist exclusively or almost exclusively of ions [112]. As ILs are usually powerful solvents and have a good dielectric constant, the sensitivity of the sensor can be improved [48, 69, 77, 83, 84, 113], after mixing ILs with the original dielectric material. Lin et al. [77] showed the sensitivity/capacitance change improvement of their PVDF-HFP dielectric layer from  $0.006 \text{ kPa}^{-1}$  to  $0.43 \text{ kPa}^{-1}$  with the increasing ionic liquid concentration from 0 to 40 wt%. The other IL used in selected articles is shown in Table.2. Besides ionic liquid, researchers also added a small number (near the percolation threshold [89]) of high dielectric constant (high- $\kappa$ ) fillers [114] to improve the sensors' performances, e.g., carbon nanotube (CNT) [66, 69, 71, 89], carbonyl iron particles (CIP) [73], carbon black (CB) [81, 82], carbon conductive paste (CCP) [67], graphene [115], Ag nanowires (AgNW) [85, 90], among many others.



To improve the sensitivity of the sensor, Choi et al. [89] added (0.2wt%, 0.4wt%, and 0.6wt %) multiwalled CNT into Ecoflex (Figure 2.17 (a)), Guo et al. [66] added carbon nanotube with an aspect ratio of 1250-3750 into PDMS (Figure 2.17 (b)), Wei et al. [67] added three composites into PDMS (Figure 2.17 (c)), Cho et al. [85] mixing the Ag nanowires (AgNWs) into the thermoplastic polyurethane (TPU) (Figure 2.17 (d)). All these filler materials improve the sensitivity of the sensor as shown in the following figure.

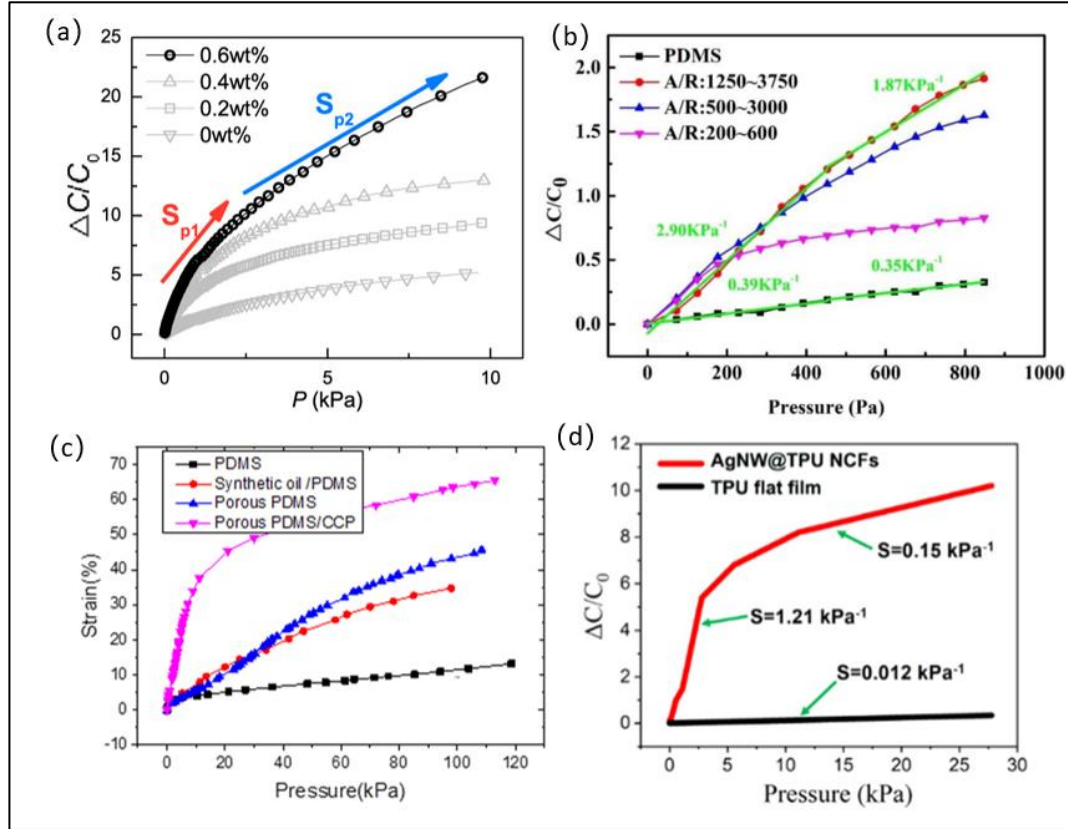


Figure 2.17 Sensitivities of sensors in present studies after adding different concentrations of high- $\kappa$  filler. (a) Ecoflex with MWCNT (reprinted with permission from Ref. [89]); (b) PDMS with CNT (reprinted with permission from Ref. [66]); (c) porous PDMS with CCP (reprinted with permission from Ref. [67]); (d) TPU with AgNWs (reprinted with permission from Ref. [85]).

Table 2.2 Ionic liquids used in some present studies.

Ionic Liquid (IL)	Abbreviation of IL	Reference	Dielectric Material	Sensitivity
poly (1-butyl-3-vinylimidazolium bis(trifluoromethanesulfonyl)imide)	[PBVIm] [TFSI]	[113]	Electrospinning the poly(ionic liquid) (synthesized by [PBVIm] [TFSI] via a free radical polymerization) and polyacrylonitrile (PAN, an electrospinning auxiliary) to form a poly(IL) nanofibrous membranes	0.49 kPa-1, <0.2 kPa; 0.18 kPa-1, 0.2-10 kPa.
1-ethyl-3-methylimidazolium bis-(trifluoromethylsulfonyl)imide	[EMIM] [TFSI]	[83]	P(VdF-HFP) added [EMIM] [TFSI]	131.5 kPa-1.
1-ethyl-3-methylimidazolium bis-(trifluoromethylsulfonyl)imide	[EMIM] [TFSI]	[69]	PVDF-HFP added [EMIM] [TFSI]	9.55 kPa-1.
1-ethyl-3-methylimidazolium bis(trifluoromethylsulfonyl)amide	[EMI] [TFSA]	[84]	Micropatterned pyramidal P(VDF-HFP) added [EMI] [TFSA]	41 kPa-1, <400 Pa.
1-butyl-3-methylimidazolium hexafluorophosphate	[BMIM]·PF6	[48]	Four porous substrates added [BMIM]·PF6 (Printing paper, textile, porous cellulose acetate (CA) film, and polyester foam)	4.46 kPa-1, 0.5 kPa; 0.312 kPa-1, 0.5-10 kPa; 0.0143 kPa-1, 10-120 kPa.
1-Butyl-3-methylimidazolium bis(trifluoromethylsulfonyl)imide	[BMIM] [TFSI]	[77]	The PDMS added [BMIM] [TFSI] and PVDF-HFP nanofiber solution were electrospined together	0.54 kPa-1, 0.01-1.5 kPa.

## 2.2.7 Other Performance Related Background

### 2.2.7.1 Proximity

The proximity performance is a characteristic only observed in capacitive sensors. Owing the proximity performance, the capacitive sensors can be categorized as self-capacitance sensors and mutual capacitance sensors [63, 82, 116]. Self-capacitance sensors, as shown in Figure 2.18 (a), have only one electrode and their capacitance are with respect to the ground [63, 82]. While the item or human skin is approaching the sensor, the capacitance value of the sensor is increasing due to the capacitance from the human body. Mutual capacitance sensors, as shown in Figure 2.18 (b), are parallel structure sensors that have a pair of parallel electrodes and the capacitance between the electrodes is measured [63, 68, 82, 115]. While an item or human skin approaches the sensor, the approaching object function as a grounded conductor which disturbs [63, 117] or absorbs [115] the fringing electric field of the sensor and absorbs the charges [116] leading to a decrease in capacitance (Figure 2.19). The capacitive sensing or proximity performance can help the sensor to detect the approaching object for collision avoidance [118] and can be used to sense the approaching item, e.g. sensing liquid height during bottling, or knowing the distance from an item to a robotic hand during grasping objects.

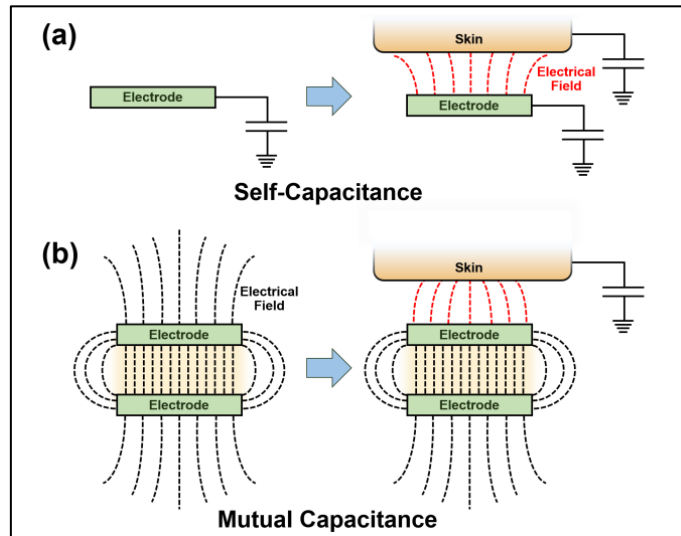


Figure 2.18 Mechanisms of proximity for two types of capacitive sensors, (a) Self-Capacitance sensor and (b) Mutual capacitance sensor (reprinted with permission from Ref. [63]).

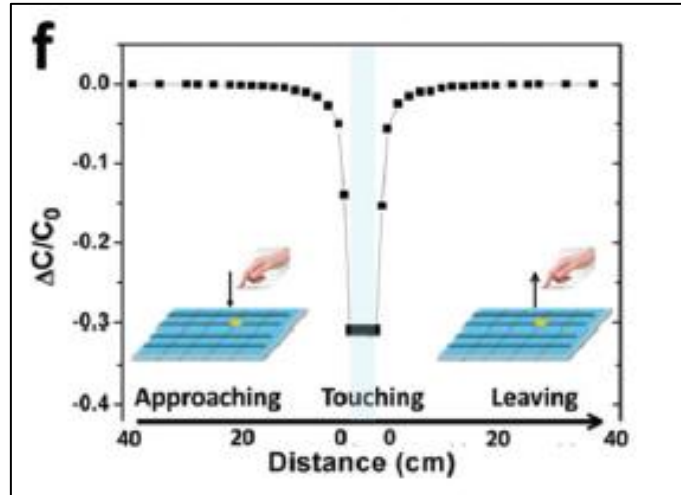


Figure 2.19 Parallel plate capacitive sensor. The capacitance decreases and recovers when the human finger approaches and removes (reprinted with permission from Ref. [118]).

#### 2.2.7.2 Plasticizer Liquid Caused Drift

For a polymer-based capacitive sensor, the addition of liquid filler could cause a capacitance change drift problem in the stability experiment, which is the measured capacitance signal keeps increasing although the applied strain/pressure remains constant.

To know the reason that caused this  $\Delta C/C_0$  drift, articles concluding stability experiments for the capacitive sensor with liquid-filler were studied. Yoon et al. [69] used PVDF-HFP as the capacitive sensor matrix and ([EMIM][TFSI]), an ionic liquid (IL), as a conducting liquid-filler. According to their stability experiment (around 10s duration) (Figure 2.20), the capacitance signal remained constant while the IL constant was 40%, but a drift in capacitance change showed up while the IL constant was 60% and this drift increased with the amount of IL used in sample preparation. They attribute this drift to a changeable mechanical modulus, which is induced by the IL content, of the sensor [69]. The addition of IL or any other plasticizing agent will weaken the secondary bonds between the polymer chains. Further, these materials have a low molecule weight, and when added to the polymer it will improve the flexibility of the polymer backbone, decreasing the crystallinity degree [119]. The decreased crystallinity could promote a decrease in the mechanical modulus of the polymer film [119], and be responsible for the capacitance change drift. This phenomenon, in which the addition of plasticizer liquid caused capacitance change drift and decreased stress, will be called “Plasticizer Liquid Caused Drift”.

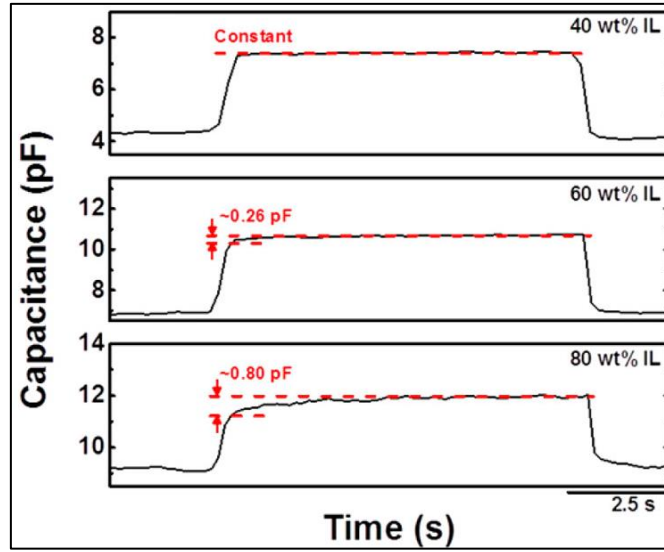


Figure 2.20 The drift in capacitance stability experiment in Sun's work (reprinted with permission from Ref. [69]).

## 2.3 Material Selection

The base material used in the wearable capacitive sensor determines its performance. The selected material is required to be comfortable, which means with a low Young's Modulus. Furthermore, to have a good sensitivity, which is one of the most important properties, suitable dielectric properties and be able to achieve a large deformation. For wearable applications, the base material needs to be soft, biocompatible and preferentially biodegradable.

### 2.3.1 Sensor structure

Currently, the main study for capacitive sensors is parallel plate capacitors. This type of capacitor is usually composed of two flexible electrodes at the top/bottom and a vacuum or a dielectric material between the two electrodes (Figure 2.12). According to the capacitance equation in Equation 2.1 and the dielectric constant equation in Equation 2.2, the capacitance value is related to the area of the electrodes facing each other, the distance between two electrodes, and the dielectric constant of the material. Also, the  $\Delta C/C_0$  is only related to  $d$  (mentioned in subchapter 2.2.5.2), but using a material with a high dielectric constant can enhance the absolute value of the capacitance to reduce its noise. Furthermore, a good electrically conductive electrode material can help import the charge from the power source to the capacitive sensor. In this way, choosing the right dielectric and electrode material is key for an enhanced capacitor.

### 2.3.2 Dielectric material

The dielectric or base material gives the capacitive sensor the most significant properties. The most popular base dielectric material used in present research is PDMS [45-47, 63-82], a silicone-based elastomer polymer. It is widely used in contact lenses, medical devices, also lubricating oils [120]. Most PDMS used commonly is the network/crosslinking format, which is fabricated by crosslinking

the vinyl groups of the two ends of long PDMS pre-polymer chains by the polymethylhydro-siloxane (curing agent) and using platinum as a catalyst [121] or mixing the base material and curing material of SYLGARD™ 184 Silicone Elastomer Kit [122]. PDMS has been extensively employed as the elastomeric dielectric layer of the capacitive sensor for its great flexibility, biocompatibility, and mechanical properties [120]. Wei et al. [67] prepared their capacitive pressure sensor with a dielectric layer of porous polydimethylsiloxane-carbon conductive paste (PDMS-CCP) composite and the obtained sensor was soft and flexible to be used as a wearable sensor (Figure 2.21 (a)). Xie et al. [65] coated the PDMS layer on a napkin as the dielectric layer of their napkin-based wearable sensor (Figure 2.21 (b)). Kim et al. [70] spin-coated PDMS substrate on a hydrogel-crosslinking AgNW layer to obtain a transparent and stretchable capacitive sensor (Figure 2.21 (c)). Cui et al. [71] used carbon nanotubes/PDMS, which were treated by a surface functionalization process, a magnetron sputtering process and an O<sub>2</sub> plasma, as their dielectric material (Figure 2.21 (d)). Sharma et al. [78] directly applied PDMS as their dielectric material and mixed it with deionized water (DI) used to create a porous structure (Figure 2.21 (e)). During the curing process, a continuous centrifugal force was applied to this material, which created a gradient in pore size and porosity, which give this sensor the ability to detect force magnitude and force direction simultaneously and independently.

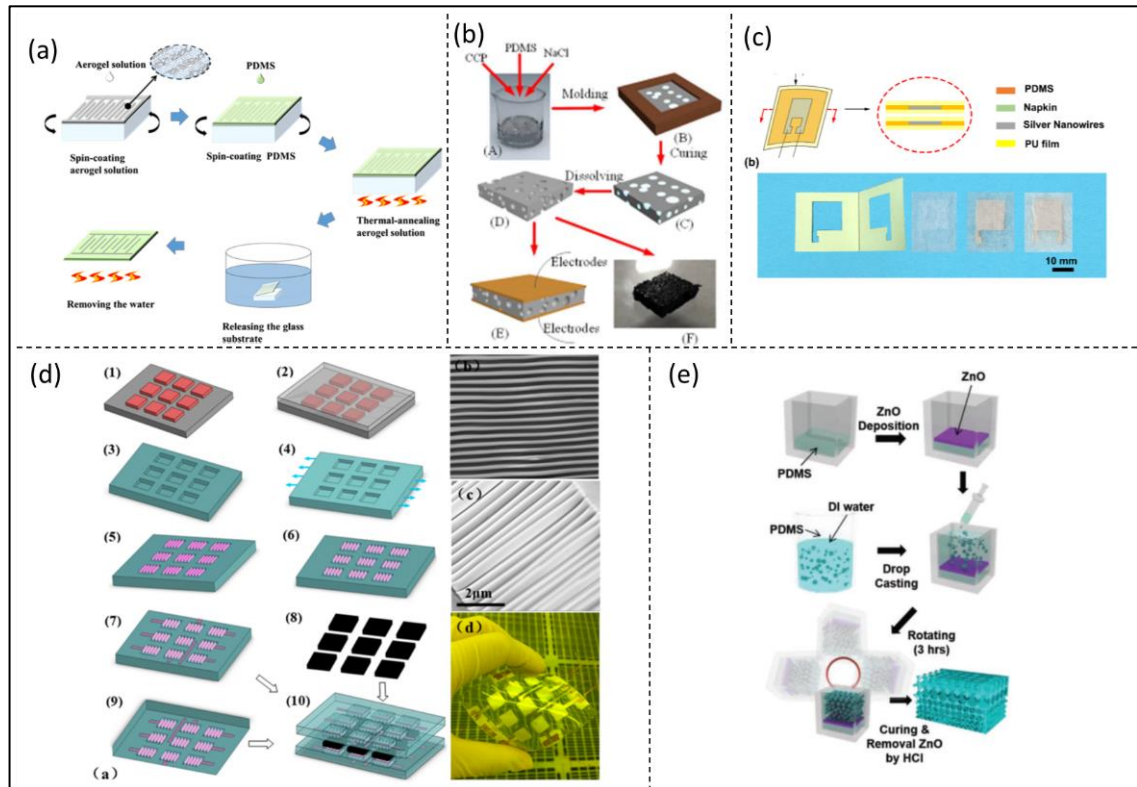


Figure 2.21 Present capacitive sensors using PDMS as the dielectric layer. (a) Wei et al. prepared PDMS-CCP as their dielectric layer (reprinted with permission from Ref. [67]); (b) Xie's napkin wearable sensor with a PDMS dielectric layer (reprinted with permission from Ref. [65]); (c) Kim used PDMS/AgNWs as dielectric layer (reprinted with permission from Ref. [70]); (d) Cui used carbon nanotubes/PDMS as their dielectric material (reprinted with permission from Ref. [71]); (e) Sharma prepared a PDMS dielectric layer (reprinted with permission from Ref. [78]).

Another well studied dielectric material is poly(vinylidene fluoride) (PVDF) [43, 77, 83, 84]. PVDF

and its copolymer (e.g. poly(vinylidene fluoride-co-hexafluoropropylene), P(VDF-HFP)) are highly used in membrane and fibre applications. It is used in the capacitive sensor due to its “excellent mechanical strength and resilience, high dielectric constant, and reliably maintenance of a specific electrospun fibre scaffold thickness” [43]. Sharma et al. [43] blended the MXenes ( $\text{Ti}_3\text{C}_2\text{Tx}$ ), a new class of conductive metal carbonitrides and carbides with high capacitance and excellent mechanical properties, with a PVDF-TrFE by an electrospinning process as their dielectric layer (Figure 2.22 (a)). Chhetry et al. [83] tried to build an electrical double layer (EDL) at the interface between the dielectric/electrolyte layer and the electrode layer. They utilized P(VDF-HFP) as the base material for the dielectric material and mixed it with different amounts of 1-ethyl-3-methylimidazolium bis(trifluoromethylsulfonyl)-imide [EMIM] [TFSI], an ionic liquid with a high dielectric constant (Figure 2.22 (b)). Cho et al. [84] prepared a P(VDF-HFP) mixed with [EMI][TfSA] as their dielectric layer (Figure 2.22 (c)). Lin et al. [77] prepared a core P(VDF-HFP) – shell (PDMS ionogel) nanofiber mat by electrospinning them with two channels and controlled flow rates of PDMS ionogel and PVDF-HFP solutions (Figure 2.22 (d)).

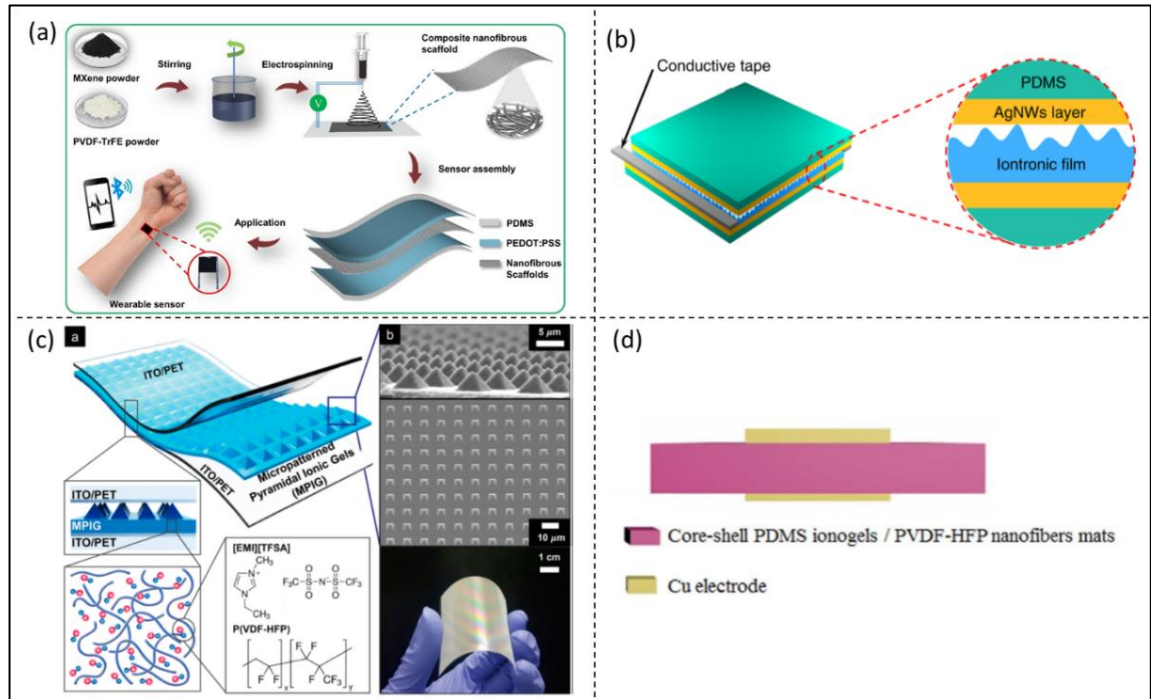


Figure 2.22 Present capacitive sensors using PVDF or related materials as the dielectric layer. (a) Sharma blended the MXenes ( $\text{Ti}_3\text{C}_2\text{Tx}$ ) with a PVDF-TrFE by an electrospinning process as their dielectric layer (reprinted with permission from Ref. [43]); (b) Chhetry mixed P(VdF-HFP) with [EMIM] [TFSI] (reprinted with permission from Ref. [83]); (c) Cho prepared a P(VDF-HFP) mixed with [EMI] [TfSA] (reprinted with permission from Ref. [84]); (d) Lin prepared a core(PVDF-HFP nanofiber) - shell(PDMS ionogel) nanofiber mat (reprinted with permission from Ref. [77]).

Polyurethane (PU) [85, 86] is used for the dielectric layer due to its excellent elasticity. PU polymer can be easily compressed and achieve high capacitance change. Zhao et al. [85] prepared the dielectric material of their capacitive sensor with an AgNW interior and a TPU exterior (Figure 2.23(a)). Liu et al. [123] mixed healable PU solution with a graphene suspension and after degassing the blend and casting it into a mould for film formation (Figure 2.23(b)). Yao et al. [86] use a



commercial PU sponge as the base material and coated graphene nanosheet as a conductive coating on the surface of PU (Figure 2.23(c)).

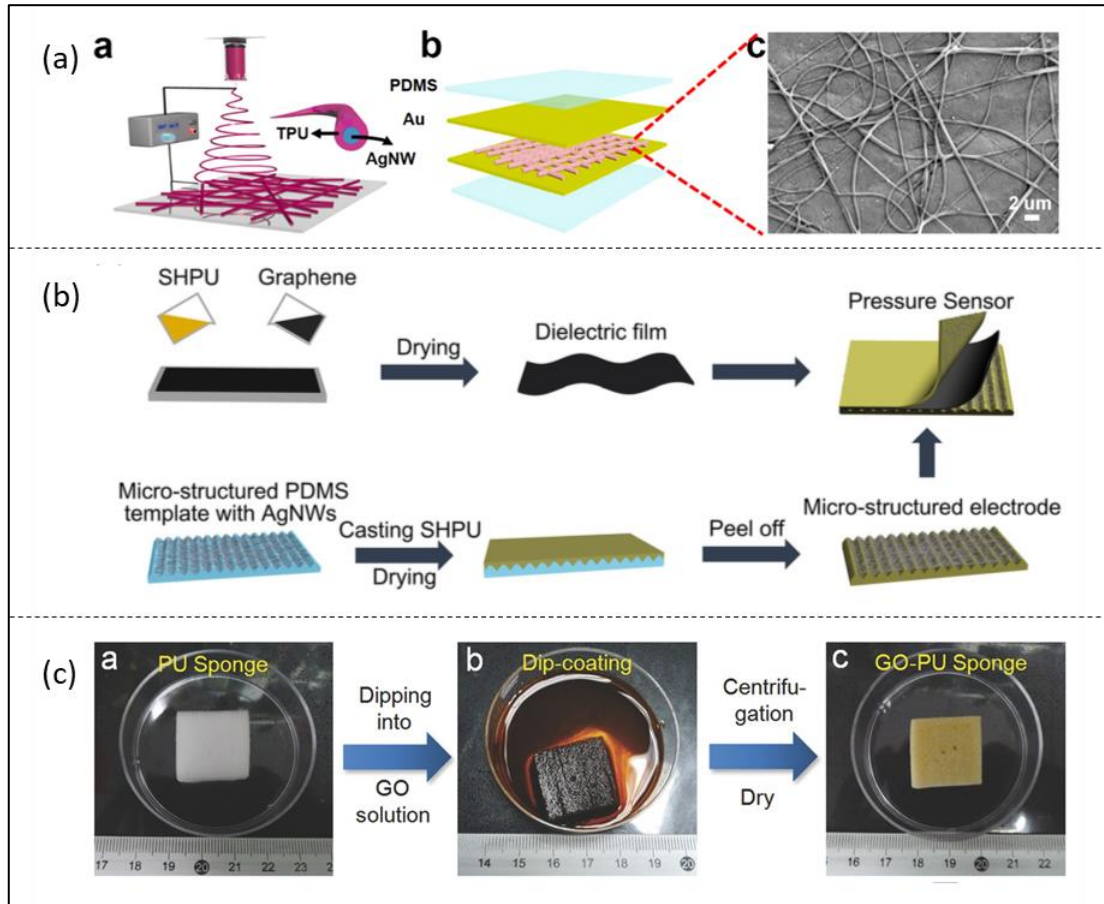


Figure 2.23 Present capacitive sensors using PU as the dielectric layer. (a) Zhao's sensor with an AgNW interior and a TPU exterior (reprinted with permission from Ref. [85]); Liu mixed HPU solution with a graphene suspension to prepare their dielectric film (reprinted with permission from Ref. [123]); Yao coated graphene nanosheet on a commercial PU sponge as the dielectric layer (reprinted with permission from Ref. [86]).

Other dielectric materials used in the present research are, e.g. Ecoflex [89, 90], hydrogel [91], polyethylene glycol terephthalate (PET) film [45, 46, 87], graphene oxide-enhanced foam-like paper, polyethylene [88], among many others.

### 2.3.3 Electrodes material

A suitable electrode, which has a constant conductivity, is a key component of capacitive sensors [70, 86]. The electrode material should deliver the electrical signal stably under different conditions, such as large deformation, hot and cold temperature, or dynamic load and static loads. Many electrode materials were used in present capacitive sensor studies, such as silver nanowire (AgNWs) [64, 65, 70, 71, 73, 78, 83, 107, 115] and copper (Cu) [46, 47, 74, 77, 79].

AgNWs has excellent electrical, optical and mechanical properties, and are known as an ideal electrode material for flexible sensor [70, 124]. AgNWs has been broadly applied in flexible electronics such as film heaters and solar cell [64, 124]. It can maintain very good electrical performance under dynamic load and large deformations due to its natural metal structure. Kim et



al. [70] embedded the AgNWs electrode onto the surface of the PDMS substrate and spin-coated silica aerogel solution on top of AgNWs to enhance the van der Waals interactions between the AgNWs and PDMS dielectric layer (Figure 2.24 (a)). Xie et al. [65] added AgNWs in ethanol solution to their PDMS dielectric layer and after the evaporation of the ethanol, the AgNWs conductive network formed (Figure 2.24 (b)). Li et al. [64] prepared an AgNWs film electrode for their PDMS capacitive sensor by airbrush spraying, spin-coating, and soak-coating, in which the airbrush spraying method fabricated AgNWs with high efficiency, good uniformity and adherence (Figure 2.24 (c)).

Cu electrode has the advantage of softness and high conductivity [46, 47]. Wang et al. [46] applied a Cu/Ni nanofiber network as their top and bottom electrodes. Chen et al. [47] used conductive copper tape as their external electrical connection to connect the pressure sensor array to the impedance analyzer.

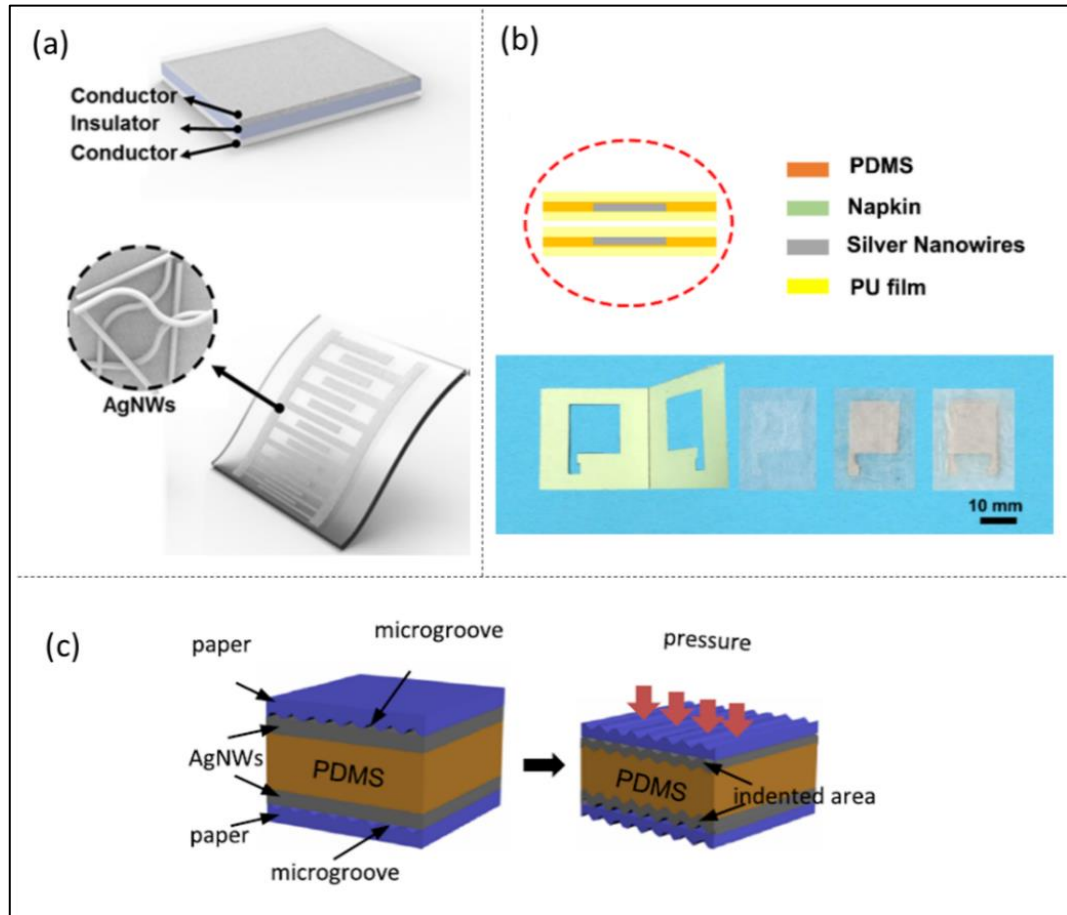


Figure 2.24 Present capacitive sensors using AgNWs as electrode layer. (a) Kim embedded the AgNWs electrode onto the surface of the PDMS substrate (reprinted with permission from Ref. [70]); (b) Xie added AgNWs in ethanol solution to their PDMS dielectric layer (reprinted with permission from Ref. [65]); (c) Li prepared an AgNWs film electrode for their PDMS capacitive sensor (reprinted with permission from Ref. [64]).

After explaining the dielectric and electrode material of the capacitive sensor in the recent studies, the performances of these sensors are collected in Table 2.3 and will be compared with the performances of the sensor in this topic.



Table 2.3 Recent studies on capacitive strain/pressure sensors with measuring pressure ranges mentioned.

Dielectric layer	Sensitivity	Response time (recover time)	Min detect limit (or range)	Reference
PDMS	0.124 kPa <sup>-1</sup> (0-15 kPa)	167 ms (117 ms)		[45]
PDMS	0.0098 kPa <sup>-1</sup> (1-5 kPa)	162 ms		[46]
PDMS	1.05 kPa <sup>-1</sup> (0.001-2 kPa)			[64]
CNTs/PDMS	2.9 kPa <sup>-1</sup> (0-450 Pa)			[66]
PDMS	1.1 kPa <sup>-1</sup> (< 4 Pa)	60ms		[67]
PU with graphene	1.9 kPa <sup>-1</sup> (<3 kPa)	<100 ms	10 Pa	[123]
PVDF-HFP	41 kPa <sup>-1</sup> (<0.4kPa)	<20 ms	max: 50 kPa	[84]
	0.055 kPa <sup>-1</sup> (0.5–10 kPa)	<200 ms (150 ms)		[108]
PDMS/PVDF-HFP	0.54 kPa <sup>-1</sup> (0.01-1.5 kPa)			[77]
PDMS	0.278 kPa <sup>-1</sup> (<2 kPa)	340 ms	38.82 Pa	[107]
Ecoflex-multiwalled CNT	6.42 kPa <sup>-1</sup> (0–2 kPa); 1.72 kPa <sup>-1</sup> (2–10 kPa)	<0.1 s		[89]
[PBVIm][TFSI]	0.49 kPa <sup>-1</sup> (0-0.2 kPa); 0.18 kPa <sup>-1</sup> (0.2-10 kPa)		20 Pa	[113]
Graphene oxide-enhanced foam-like paper	0.63 kPa <sup>-1</sup> (0-2 kPa)	180 ms (120 ms)		[115]
PDMS	0.16 kPa <sup>-1</sup> (<1 kPa); 0.04 kPa <sup>-1</sup> (0.75-2.5 kPa)			[72]
PLGA-PCL	0.863 ± 0.025 kPa <sup>-1</sup> (1-1.86 kPa)	251 ms (170 ms)	1.24 Pa	[125]
PDMS/AgNWs	0.31 kPa <sup>-1</sup> (< 1 kPa); 0.15 kPa <sup>-1</sup> (1-5 kPa)	50 ms (40 ms)		[78]
PDMS	0.26 kPa <sup>-1</sup> (<0.33 kPa); 0.01 kPa <sup>-1</sup> (0.33-250 kPa); 0.0009 kPa <sup>-1</sup> (250kPa-1MPa)		(1 Pa-250 kPa)	[47]
Carbonyl iron particles, CIP/PDMS	0.301 kPa <sup>-1</sup> (0-3 kPa); 0.023 kPa <sup>-1</sup> (2-100 kPa); 0.004 kPa <sup>-1</sup> (100-200 kPa)		1.2 Pa	[73]
Porous cellulose acetate (CA) film with [EMIM]·PF <sub>6</sub>	4.46 kPa <sup>-1</sup> (0.5 kPa); 0.312 kPa <sup>-1</sup> (0.5-10 kPa); 0.0143 kPa <sup>-1</sup> (10-120 kPa)	39 ms		[48]
40 wt% Porous PGS and 60 wt% EG	0.15 kPa <sup>-1</sup> (5% strain or 0-2.02 kPa); 0.20 kPa <sup>-1</sup> (10% strain or 0-4.33 kPa); 0.27 kPa <sup>-1</sup> (20% strain or 0-8.91 kPa)			This work

#### 2.3.4 Poly(glycerol sebacate) as Dielectric material

Poly(glycerol sebacate) (PGS) is a biocompatible and biodegradable elastomer first presented by Wang et al. in 2002 [126]. In their studies, to design a rubber-like elastomer owning good mechanical properties which could be achieved through covalent bond and hydrogen bonding, they chose glycerol (CH<sub>2</sub>(OH)CH(OH)CH<sub>2</sub>OH) as an alcohol monomer, and sebacic acid (HOOC(CH<sub>2</sub>)<sub>8</sub>COOH), which was approved to be safe in vivo. These two monomers reacted through the condensation polymerization to become PGS (Figure 2.25). The PGS has an excellent degradation property, easy synthesis process and good mechanical performance [127] and has been approved by the US Food and Drug Administration (FDA) for biomedical applications. Furthermore, PGS has a large elongation at break (large than 260%) and tailored Young's modulus

by controlling the curing temperature and time. For the wearable pressure/strain sensor application, the excellent elastomeric properties and good dielectric properties make the PGS a good candidate for capacitive pressure/strain sensor applications.

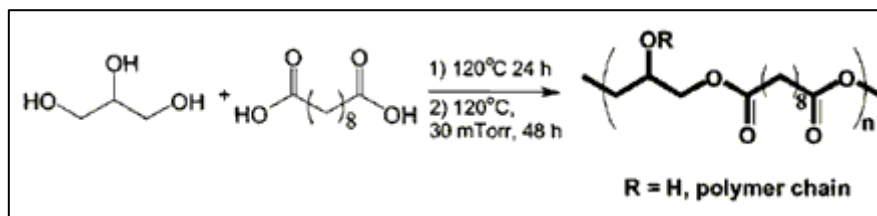


Figure 2.25 The sebacic acid and glycerol form PGS through condensation polymerization.

PGS has excellent elastomer properties and its samples of porous scaffold structure have a low tensile Young's Modulus of around  $88 \pm 9$  kPa [12]. Young's Modulus of PDMS and human skin are compared here. For PDMS. For different curing temperatures, curing time and post-process methods, Young's Modulus of PDMS fluctuates between 1 - 4 Mpa [128-131]. For human skin. Many researchers measured Young's Modulus of human skin from the back of cadavers and most of the results are from 75 – 100 Mpa [132-134]. In this way, compared with PDMS, the Young's Modulus of PGS is less than a quarter of that of PDMS, which means the wearable sensor made by PGS is softer and more comfortable to wear. Compared with human skin, the Young's Modulus of PGS is much lower, so it has a large potential for wearable sensor applications and replacing the present uncomfortable body parameters measurement devices.

PGS has great dielectric properties. A capacitor with a higher permittivity could store more electrons and have a better capacitance capacity. The permittivity is influenced by frequency. According to the previous work from my supervisor, Vitor Sencadas et al. [135] synthesised solid PGS samples without any porogen had a permittivity of 5.6 under the frequency of 100 kHz. While a porosity of 92% was achieved by mixing PGS and NaCl by a mass ratio of 1:10, its permittivity become around 1.22. The dielectric constants of other popular dielectric materials were searched to compare. PDMS has a permittivity in the range of 2.3 to 2.8 [136-139]. The permittivity of PVDF is around 10 [140]. PU has a permittivity of 4.6 [140]. Compared with these materials, the dielectric property of solid PGS with a constant of 5.6 is above medium and great. With the addition of porogen, the PGS sample with a porosity of 92% has a relatively low permittivity of 1.22. However, during the application process that the sample was compressed, the permittivity increased to 2.67 (74% porosity), which was as good as the dielectric properties of the PDMS.

Also, the great biodegradability of PGS makes it competent for the in vivo sensing mission. According to the work of Wang et al. [141], the degree of swelling for PGS was relatively low and the increase in water content of PGS implants was linear, which was desirable compared with the abruptly increasing water content for PLG, poly(DL-lactide-co-glycolide). Furthermore, PGS had a great ability to provide mechanical support in vivo that its mechanical strength gradually and slowly decreased and still kept a modulus of more than 50% after 35 days, compared with PLG which loses

its mechanical strength in a short time after implant (7 days).

According to the above discussion, the PGS has an excellent elastomer property, good dielectric behaviour and potential biodegradability. In this way, PGS was used as the base dielectric material in this study.

## **2.4 Outlook**

According to the above explanation, the capacitive pressure sensor is chosen as the main type of sensor studied in this thesis and the PGS was used as the dielectric layer of the sensor. Besides, two targets are required to be achieved. The first one is to achieve a comfortable wearing experience, in other words, a good elastomer property of the material. The Young's Modulus of the sensor is required to be low and that of the human skin is needed to be compared. The second is to improve the electromechanical performance, especially the sensitivity of the capacitive sensor, which is its drawback mentioned above. A material with a good (high) permittivity is required and other methods to improve its permittivity and sensitivity are needed to be searched and conducted.

## Chapter 3 Material Preparation and Characterization

### 3.1 Chemicals and Reagents Used

The chemical reagents and materials used in this thesis are listed in Table 3.1. All materials were used as received.

Table 3.1 List of chemical reagents and materials used in this thesis.

Reagent name	Company
Sebacic acid ( $\geq 99.5\%$ , ACS reagent)	Sigma-Aldrich
Glycerol ( $\geq 99\%$ )	Sigma-Aldrich
Ecoflex™ 00-30	Smooth on
Ethylene Glycol (99.8 %)	Sigma-Aldrich
Sylgard 184 Silicone elastomer	Dow

### 3.2 Material Preparation

PGS foam was prepared using condensation polymerization [126, 135] [126] in two steps, shown in Figure 3.1. The first step was to prepare the PGS pre-polymer. Equal molar ratios of sebacic acid and glycerol (50.5 g: 20.49 g) were added to a round flask and mixed. Then, the round flask was put into an oil bath at 120 °C for 24 hours, and argon pass through at a steady flow rate to ensure an inert atmosphere inside. During this step, an external thermocouple was used to keep the temperature at 120 °C. After, the pre-polymer was collected and stored in a beaker below -20 °C until further use.

The second step was to fabricate the PGS foam by manually mixing 6 grams of pre-polymer and 60 grams of porogen NaCl (mass ratio of 1:10). It was required to be thoroughly dispersed to avoid any porogen clumps. After being mixed, the mixture was spread in the polytetrafluoroethylene (PTFE) mould with a size of 100mm  $\times$  100mm  $\times$  5 mm and a piece of baking paper was covered over the mould and placed into a PHI compression press (Appendix A, Figure A.1). The ram force of the press was set to 10,000 – 12,000 pounds, and the compression process lasted for 15 mins. Then, the PGS sample was put in the drying vacuum oven (FAITHFUL, Appendix A, Figure A.2) at 120 °C, under a vacuum of 0.08 Pa for 96 hours to allow the pre-polymer to cure. The cured solid sample was immersed in deionized water under magnetic stirring (Corning Hot Plate Stirrer, Appendix A, Figure A.3) for 24 hours to remove the NaCl porogen. Further, the sample was stored at -32 °C in the fridge, and freeze-dried in the freeze dryer (TOPTION, Appendix A, Figure A.5) to remove the water present in the porous structure. After 24 hours, the sample can be collected from the dryer and is ready to be used. After, small foam cylinders of 13 mm diameter were cut to build the capacitive sensors.

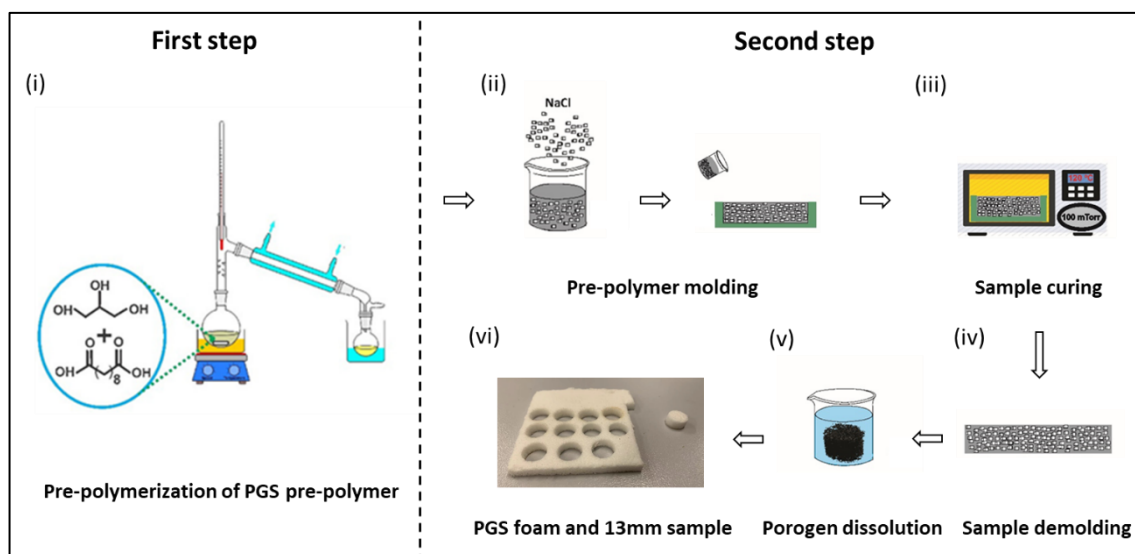


Figure 3.1 PGS foam preparation.

### 3.3 PGS Dry Sensor Assembly

To assemble the electrode material in the sensor and avoid liquid filler leakage in future experiments, an Ecoflex casing was used to assemble the sensor. A cylinder foam with a height of 6.2 mm and a diameter of 13 mm was used to assemble the PGS dry sensor.

First, the Ecoflex casing consisting of Ecoflex Bottom&Wall and the EcoflexCover was prepared as shown in Figure 3.2 (a) and (b). The 3D model, Inner Model and Base Model (Figure 3.2 (a)), of the Ecoflex Bottom&Wall were created by SolidWorks 2020 software, and the 3D printing work was done in a Flashforge Creator printer and polylactic acid (PLA) filament was used as the material for the 3D printing work.

According to the size of the sample mentioned above, the Inner Model used to shape the inside size for the Ecoflex Wall was set as a height of 9 mm, which is higher than the samples' height in order to pull the model out easier, and a diameter of 13 mm, which is similar to the samples' diameter. Then, it is the design for the Base Model. For the thickness of the Ecoflex Wall, it should not be too thin as the Ecoflex liquid was required to be manually inserted into this model with a syringe fitted with a needle with gauge 22, and it should not be too thick due to the softness properties of the wearable sensor, so the thickness of the Ecoflex Wall was set as 1.5 mm. The Ecoflex Bottom is required to be thin (around 1 mm), and also tolerance of height size is needed due to the addition of EG and bottom and top electrodes (around 0.3 mm increase). In this way, for the Base Model, the inside extrude cutting part was set as a diameter of 16 mm ( $= 13 \text{ mm} + 1.5 \times 2 \text{ mm}$ ) and a height of 7.5 mm ( $= 6.2 \text{ mm} + 1 \text{ mm} + 0.3 \text{ mm}$ ), and the size of the Base Model was set as a diameter of 20 mm and a height of 10 mm.

After the moulds (Base Mould and Inner Mould) were printed according to the above 3D models, the Ecoflex resin was prepared by mixing 5.0 g of Ecoflex Part A and 5.0 g of Part B (according to manufacturer instructions) in a paper cup and stirring them manually. In each step of later fabrication,

a new batch of fresh Ecoflex resin was mixed and poured, and the curing process took at least 6 hours. The mixing resin was poured into the Base Mould first to form the Ecoflex Bottom. After curing, the Inner Mould was put in the centre of the Ecoflex Bottom. The Ecoflex liquid was placed inside a syringe and then injected into the free space between the Base Mould and Inner Mould to form an Ecoflex Bottom&Wall according to Figure 3.2 (a). An Ecoflex Cover shown in Figure 3.2 (b) was prepared by pouring the liquid on a smooth surface, and the liquid flowed over the surface to an Ecoflex film. A proper size of this layer was cut as the Ecoflex Cover for each sensor.

Then, Silver Tape electrodes (MWRF Source company) were prepared and attached to the Ecoflex Bottom&Wall. The tapes were laser cut to the size shown in Figure 3.2 (c) by Versa Laser Device. To assemble the lower silver tape in the cured Ecoflex, an incision was created with a sharp scalpel to get the tape through (Figure 3.2 (d)).

Finally, the whole sensor was assembled by placing the silver tape on the top of the Ecoflex Bottom, followed by PGS foam, and then another silver tape was used as the top electrode, being everything enclosed by the Ecoflex Cover (Figure 3.2 (e)). The Ecoflex Bottom&Wall and Cover were cured together by Ecoflex. A photo image of the final sensor is shown in Figure 3.2 (f), and a schematic representation of each step of the sensor assembly is shown in Figure 3.2. The sizes of the PGS foam and the assembled sensor (with Ecoflex casing) are displayed in Table 3.2.

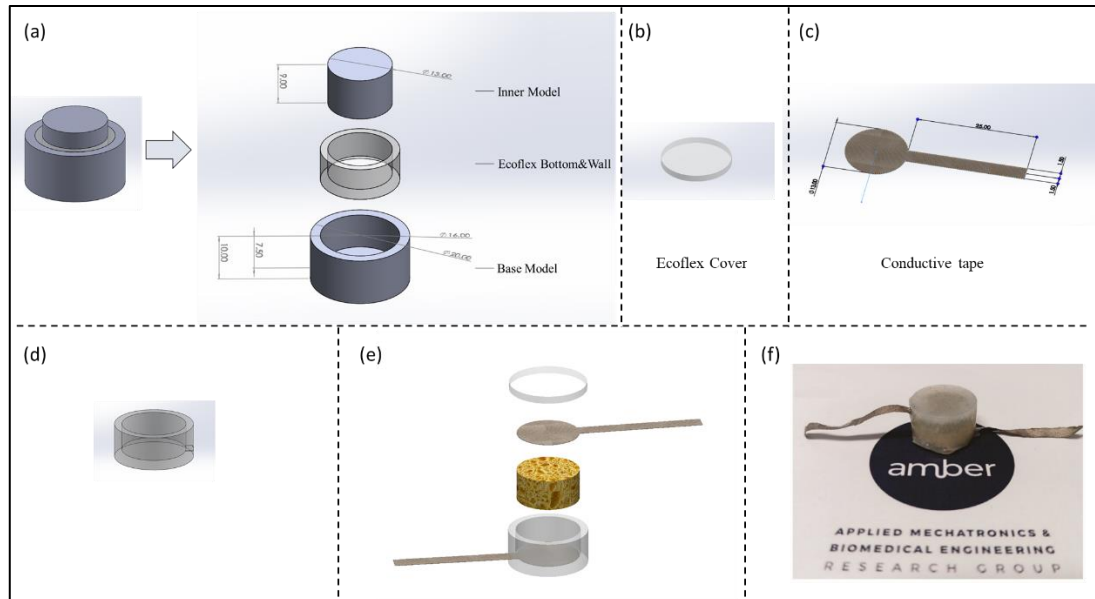


Figure 3.2 Sensor assembling process. (a) Fabrication of the Ecoflex bottom&wall; (b) Ecoflex cover; (c) Laser cutting the silver tapes; (d) Creating an incision on the Ecoflex wall; (e) Assembling (a) - (e); (f) the photo image of the PGS series sensor.



Table 3.2 The sizes of the PGS dry foam sample and PGS dry sensor.

Parameters	Value	
	PGS dry foam sample	PGS dry sensor
Radius, $r$ (mm)	6.5	7.8
Height (mm)	6	8.6

### 3.4 Material Characterization

The characterization of the PGS dry foam sample will be presented and discussed in this subchapter (Table 3.3). The morphology of the sample will be first presented to visualize its inner porous microstructure. Then, the mechanical and electrical characterization of the foam will be introduced.

Table 3.3 Material Characterization

Characterization	Measurement	Significance
Morphology	SEM	To show and analyse the microstructure of the sensor.
Porosity	Pycnometer	To show the ratio between air and base material
Mechanical	Young's Modulus	To quantify the softness of the sensor.
Electrical	Dielectric constant	The relative ability of the dielectric to store electrostatic energy in an electric field.

#### 3.4.1 Sample Morphology

The sample morphology was analysed through scanning electron microscope (SEM). Prior to the analysis, the sample was coated with a conductive thin layer of gold deposited by sputtering with a Smart Coater, from JEOL (Appendix A, Figure A.8). The SEM images were acquired with a JEOL benchtop scanning electron microscope (JCM-6000), using an accelerating voltage of 15 kV.

#### 3.4.2 Mechanical Behaviour

The mechanical behaviour of the PGS foam was assessed through a universal testing machine (EZ series, from Shimadzu, Appendix A, Figure A.12). Cylindrical samples with a height of 6.1 mm and a diameter of 13 mm were cut from the prepared foam and fitted between the platform of the universal testing machine and a pressure head connected with a 10 N load cell. The force and stroke volume applied to the PGS foam was evaluated at room temperature with a stroke speed of 5 mm/min. These mechanical properties are presented as the average and standard deviation of three measurements.

#### 3.4.3 Electrical Behaviour

The dielectric behaviour of the PGS foam was measured with an LCR meter from Zurich Instrument MFIA Impedance Analyzer fitted with a 16451B Dielectric Experiment Fixture from Keysight (Appendix A, Figure A.9). The measurements were performed at room temperature, in a frequency range between 1 kHz to 5 MHz.

### 3.5 Sensor Characterization

After studying the properties of the PGS foam, it was started the characterization of the assembled sensor. The electromechanical characterization of the sensor will be presented first, including Sensitivity and Gauge Factor, response time and recovery time, repeatability, long-term dynamic stability and static stability. After, the environmental behaviour will be introduced, including proximity and temperature sensitivity. Table 3.4 presents a summary of the characterization studies performed on the assembled sensors.

Table 3.4 Sensor Characterization

Characterization	Measurement	Significance
Electromechanical	Sensitivity (kPa <sup>-1</sup> ) and Gauge Factor	To quantify how accurate the sensor could monitor pressure or deformation.
	Response time and recovery time (s)	To quantify the time that the sensor is required to respond to a force or deformation.
	Repeatability	To show the sensor's capability to return the same signal in the load-unload experiment.
	Long-term dynamic stability	To show the sensor's capability to keep the same signal under a long-term dynamic load.
	Static stability	To show the sensor's capability to keep the same signal under a static load.
Environmental	Proximity	To quantify the distance that the sensor can detect an approaching object.
	Temperature sensitivity (°C)	To quantify the sensor's capability to measure the environment temperature.

#### 3.5.1 Electromechanical Behaviour

The electromechanical experiments show the performance of the sensor to convert the pressure or strain inputs to analyzable electrical signals.

In the electromechanical experiments, the sensor was placed between the compression plates of the universal testing machine, and at the same time, the sensor was connected to the LCR Meter (Figure 3.3). A computer was used to connect these two devices and collect and record the data generated during the electromechanical measurements. The capacitance data was obtained from the LCR meter and was post-processed to normalized change in capacitance,  $\Delta C/C_0$ , according to:

$$\frac{\Delta C}{C_0} = \frac{C_i - C_0}{C_0} \quad \text{Equation 3.1}$$

where  $C_0$  is the initial capacitance (the first capacitance data in the recorded file) and  $C_i$  is the real-time capacitance value. The mechanical signal, stroke and force, were obtained from the universal testing machine and were post-processed to strain and stress.

The universal testing machine and LCR Meter were set to the parameters shown in Table 3.5 during the electromechanical experiments.

Table 3.5 Electromechanical Parameters set for universal testing machine and LCR Meter.

	Parameters	Input Values
<b>Mechanical signal (universal testing machine)</b>	Load Cell	10 N
	Strain Speed	5 – 1000 mm/min
	Strain	5%, 10% or 20%
	Sampling time	10 msec, 1 msec
<b>Electrical signal (LCR Meter)</b>	Type	Compression
	Frequency	300 kHz
	Max Bandwidth	10 Hz
	$\Omega$ Suppression	80 dB
	Data Transfer Rate	1,000 or 100 Sa/s

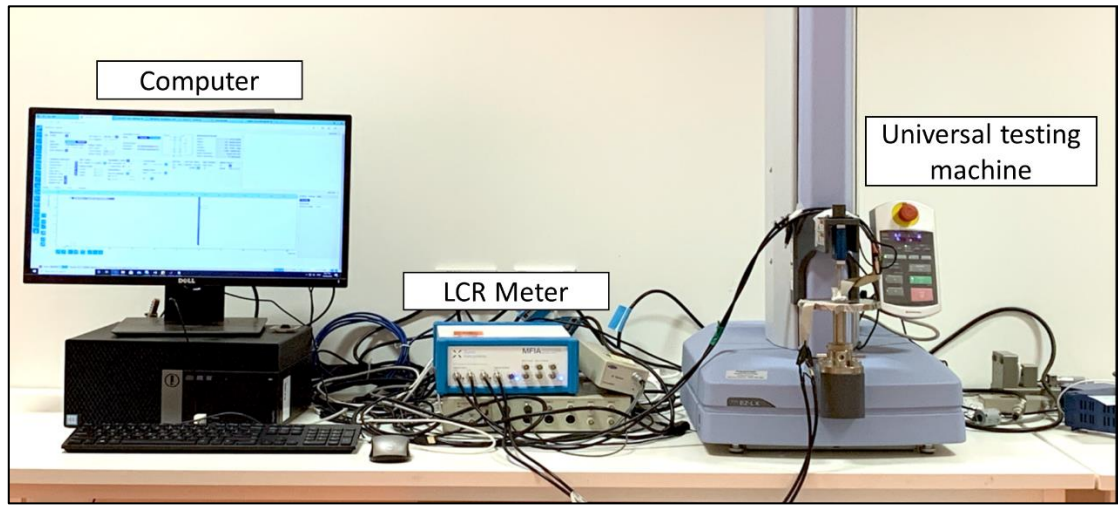


Figure 3.3 Sensor's electromechanical behaviour measured with a computer, LCR Meter and universal testing machine.

#### 3.5.1.1 Sensitivity and Gauge Factor

To measure the Sensitivity and Gauge Factor, load-unload experiments for 20 cycles were conducted (Figure 3.4). To know the sensitivities in different conditions, such as high-speed impact or mild deformation, the sensors underwent strains with load speeds of 5 mm/min, 10 mm/min, 20 mm/min, and 50 mm/min for 20 cycles, and at each speed, the sensor was compressed to the strains of 5% (mild deformation), 10% (medium) and 20% (large). All experiments were performed at room temperature.

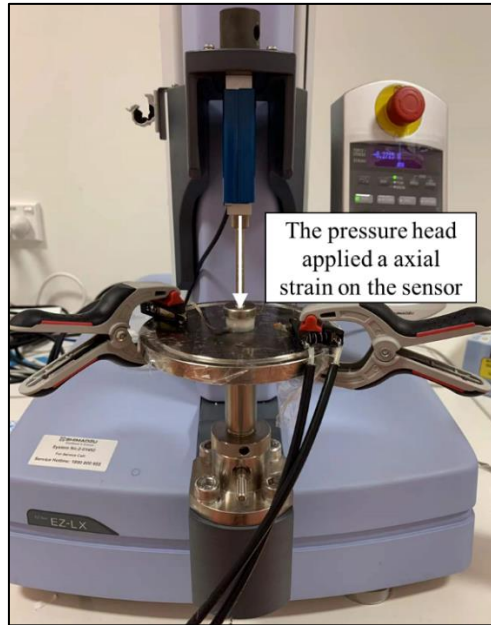


Figure 3.4 Sensor was put on the platform of the universal testing machine.

#### 3.5.1.2 Response Time and Recovery Time

Response time determines how fast the capacitive sensor could generate a  $\Delta C/C_0$  response when a force or a strain is applied. In this experiment, the sensor was compressed to 5% strain with a stroke speed of 1000 mm/min, held for 60 seconds, and recovered to the original state, while measuring  $\Delta C/C_0$  simultaneously. The response time in this experiment was measured by using the time when  $\Delta C/C_0$  rose to the highest point at the first turn minus the time when  $\Delta C/C_0$  started to increase, and the recovery time is measured by using the time when the  $\Delta C/C_0$  decreased to the lowest point at the second turn minus the time when  $\Delta C/C_0$  starts to decrease.

#### 3.5.1.3 Static Stability

Static stability indicates the ability that sensor performances to remain constant over time. The change in stability is also known as drift. For capacitive sensors, this can be attributed to viscoelasticity, creep or relaxation [69]. The stability experiment is significant to indicate whether the sensor can stay at the same base capacitance and avoid detectable drift while a static strain is applied for long-term static applications, only a stable sensor can return to a similar base capacitance while measuring the same condition.

The stability evaluation was measured by compressing the sensor to a 20% strain at a speed of 1000 mm/min and held for 3,600 seconds. The returned  $\Delta C/C_0$ , strain and stress were simultaneously recorded in this experiment.

#### 3.5.1.4 Repeatability and Long-term Dynamic Stability

Repeatability is used to describe the ability of a sensor to provide the same result, under the same circumstances, and give an indication of the electromechanical consistency of the sensor. Here, it

was investigated by applying a cyclic strain of 20% for 15 cycles and at the same time recording the sensor's  $\Delta C/C_0$ , strain and stress. A cycle of strain consists of applying a strain at a speed of 1000 mm/min, holding for 60 seconds, releasing and resting for 60 seconds, and repeating the input over the 15 cycles.

The long-term dynamic stability indicates whether the sensor could be used to accurately measure a dynamic load for long periods of time, and assess the sensor life-cycle. To demonstrate the dynamic stability, the sensors were submitted to 1,000 mechanical loading-unloading cycles. In each cycle, the pressure head fell down and compressed the sensor at a speed of 50 mm/min until reaching 20% strain and recover to the initial position. The  $\Delta C/C_0$  and stress were recorded during the measurement.

### **3.5.2 Environmental Behaviour**

#### **3.5.2.1 Proximity**

This performance was analyzed by different proximity distance experiments, and the process is shown in Figure 3.5. The capacitance signal and the stroke data were recorded by LCR Meter and the universal testing machine, respectively. The sensors were placed on the platform of the EZ Experiment device, and the pressure head was moved to a height that is just close to the top surface of the sensor to avoid touching the sensor. The pressure head was lifted for 200 mm, 80 mm, 50 mm, 30 mm or 20 mm. Then, the distance of the pressure head was set to zero and moved to 199.5 mm, 79.5 mm, 49.5 mm, 29.5 mm or 19.5 mm at a speed of 3 mm/s to test the proximity properties and avoid inertia leaded contact. When the pressure head arrived at its set position, it was kept for 60 s and then it go back to the zero distance position. Three cycles were conducted in each distance proximity experiment and there was a 60 s interval between each cycle. The capacitance and the distances were recorded during these experiments.

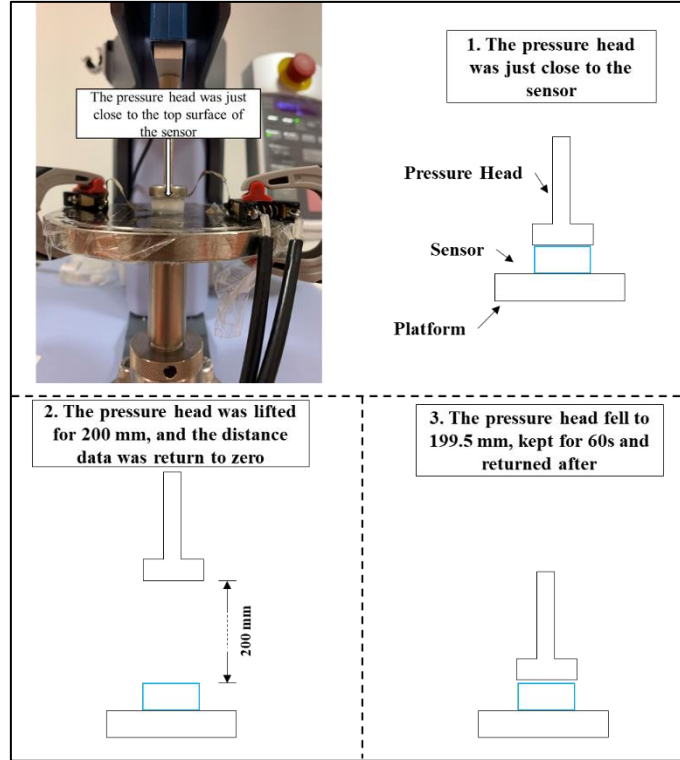


Figure 3.5 Proximity measurement: the pressure head is moved just close to the top surface of the sensor and the proximity experiment process.

### 3.5.2.2 Temperature Sensitivity

Besides tactile sensation caused by the mechanical force, the feeling caused by the temperature change is also a significant somatosensory signal. The wearable sensor owing temperature monitoring function could monitor temperature variations when it touches a surface, and this property can find applications in soft robotic devices, or human body temperature monitoring.

The PGS<sub>40</sub>/EG<sub>60</sub> sensor was placed into a heated vacuum dessicator (Vacuum-Temp, JP Selecta) (Appendix A, Figure A.13) to evaluate its temperature sensitivity. The sensor's capacitance of 25 °C, was used as a reference to calculate the  $\Delta C/C_0$  value. The temperature started from 25 °C and rose to 70 °C with a temperature increase step of 5 °C. Each time it rose to a higher temperature, it was required to remain at that temperature for 5 mins to ensure homogenous temperature distribution in the sensor, before the capacitance measurement was recorded.

## Chapter 4 Results and Discussion

In this chapter, the material characterization of PGS foam is presented first. Then, the electromechanical behaviour of the PGS sensors is discussed. After the performance of the PGS filled with ethylene glycol, a liquid with high dielectric properties are systematically assessed and compared with the ones obtained for the PGS dry sensor, to understand the effect of the high dielectric liquid on the overall sensor electromechanical behaviour.

### 4.1 PGS Foam Characterization

#### 4.1.1 Morphology

The SEM image of PGS foam morphology is shown in Figure 4.1. The sample reveals an interconnected porous morphology consisting of large pores ( $\approx 300 \mu\text{m}$ ) as a major part and small voids in the walls of the large pores. The large pores were formed after the porogen (NaCl) was mixed in the PGS and dissolved in the deionized water after curing, while the formation of small voids could be attributed to the evaporation of water, which resulted from the curing of the PGS foam at  $120^\circ\text{C}$  [135, 142, 143].

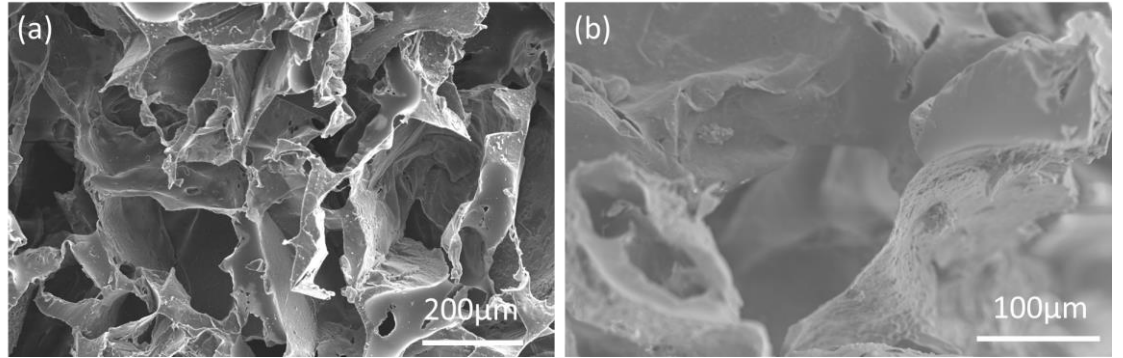


Figure 4.1 SEM image of the PGS foam. (a) The overall morphology of the PGS foam and (b) detail of the pore walls.

#### 4.1.2 Mechanical Behaviour

After obtaining the stroke volume and the force from the universal testing machine, the strain, stress, and Young's Modulus of PGS foam were evaluated.

The strain ( $\epsilon$ ) of the PGS sample is calculated by:

$$\epsilon = \frac{\Delta l}{l} = \frac{\text{stroke of the pressure head}}{\text{the initial height of the sensor}} \quad \text{Equation 4.1}$$

where the  $\Delta l$  is the displacement and  $l$  is the initial height of the sample.

The stress ( $\sigma$ ) of the sensor was calculated using the equation:

$$\sigma = \frac{F}{A} \quad \text{Equation 4.2}$$

where, F is the force measured by the load cell of the universal testing machine, and A is the contact surface area of the sample ( $A = \pi r^2$ ).

The Young's Modulus, E, can be calculated through:

$$E = \frac{\varepsilon}{\sigma} \quad \text{Equation 4.3}$$

The results under 60% strain are displayed in Figure 4.2. The PGS foam showed a linear stress-strain curve up to 30% with an average Young's Modulus of  $8.7 \pm 0.3$  kPa, which was softer than many present popular dielectric materials like PDMS ( $E = 1 - 4$  MPa [129-131]), Ecoflex ( $E = \sim 60$  kPa [144]), or even human skin with an E between 75 – 100 Mpa [132-134]. This low Young Modulus could be attributed to the high porosity of PGS foam (around 92%), leading to a soft structure.

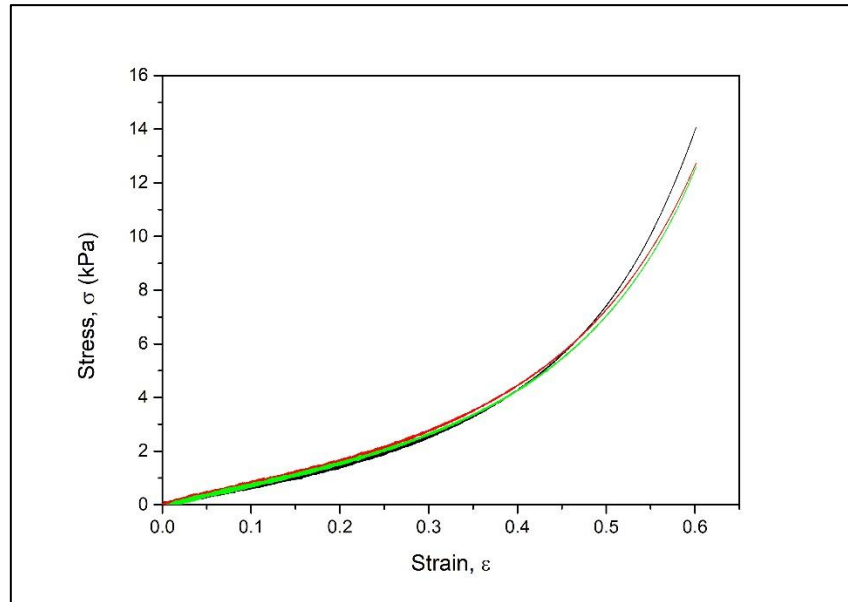


Figure 4.2 Stress-strain curve for 3 independent experiments.

#### 4.1.3 Electrical Behaviour

The dielectric spectroscopy of the PGS foam sample and PGS foam added 60% EG solution sample is shown in Figure 4.3 (a). The relative permittivity decreases with increasing frequency due to the reduced contribution of free space charge at higher frequencies [145]. By replacing the air ( $\varepsilon_{air} = 1$  [135, 146]) with EG ( $\varepsilon_{EG} = 37$  [147]), the dielectric constant of the samples at 300 kHz increase from 4.2 to 7.7 (Figure 4.3 (b)). This increasing could be expected as the high porosity (92%) of the foam allows a large volume of high dielectric constant liquid to replace the air voids, leading to an overall increase in the sample dielectric constant.



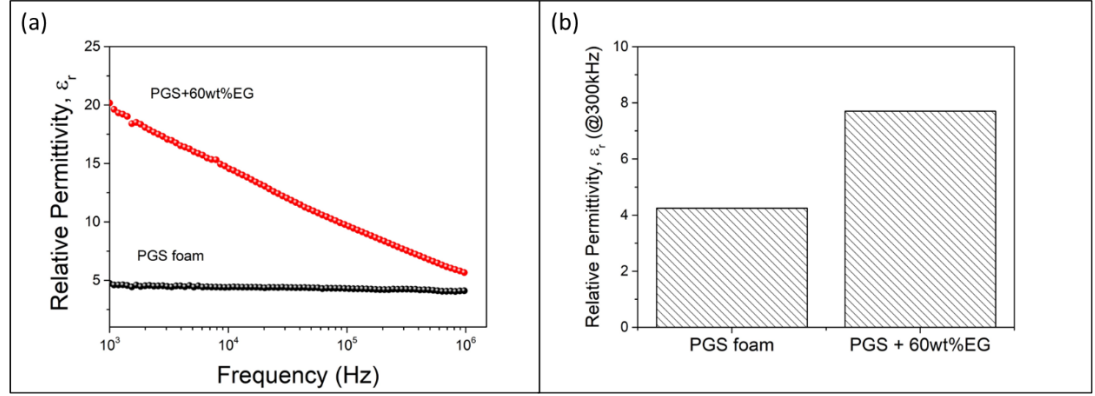


Figure 4.3 Relative permittivity ( $\epsilon_r$ ) of the PGS and the PGS<sub>40</sub>/EG<sub>60</sub> sensor (a) at different frequencies and (b) at 300 kHz.

## 4.2 PGS Dry Sensor Characterization

### 4.2.1 Capacitance Change Signal in Load-unload Electromechanical Experiments

As a signal in the Sensitivity and GF behaviour, the normalized capacitance change was analyzed separately to reflect the sensor's capability to follow the mechanical input and return a reliable electrical signal while measuring the deformation or stress.

The load-unload experiment results of the PGS dry sensor under different strains and load speed conditions are shown in Figure 4.4. The PGS dry sensor showed a  $\Delta C/C_0$  signal with good repeatability and low noise for high deformations ( $\epsilon = 20\%$ ), where the  $\Delta C/C_0$  reached around 46%. However, for the mild strains (5% strain), despite the signal retrieved from the sensor could follow the mechanical input, it presented some degree of noise, suggesting that the PGS dry sensor had a good performance for high deformations, but could not be used to detect small strains. The  $\Delta C/C_0$  of the PGS dry sensor at all conditions is shown in Appendix B, Figure B.1.

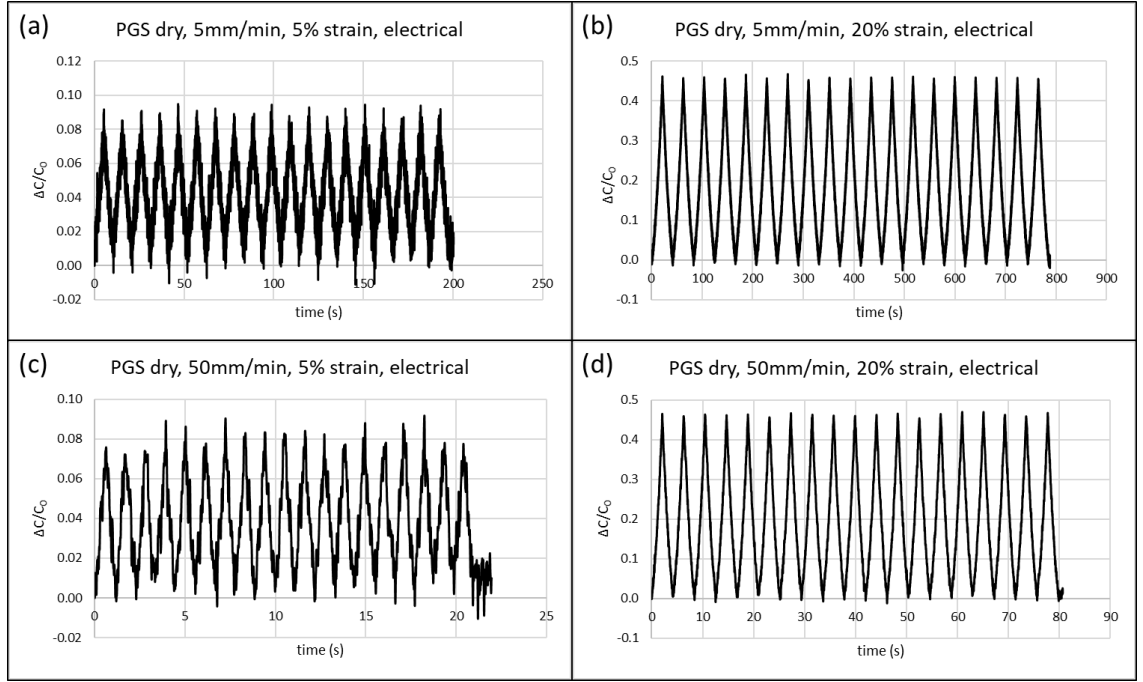


Figure 4.4 The  $\Delta C/C_0$  of the PGS dry sensor under (a) 5 mm/min, 5% strain; (b) 5 mm/min, 20% strain; (c) 50 mm/min, 5% strain; (d) 50 mm/min, 20% strain.

#### 4.2.2 Sensitivity and Gauge Factor

Sensitivity ( $S$ ) and Gauge Factor ( $GF$ ), which represent the magnitude of capacitance generated by the same applied stress or strain, respectively, are significant indicators that whether is sufficiently sensitive to detect the mild pressure/strain and present it accurately. For a parallel plate capacitance sensor, sensitivity was described as the slope of  $\Delta C/C_0$  versus applied stress ((Equation 4.4, Figure 4.5 (a)), and the Gauge factor is the slope of  $\Delta C/C_0$  versus applied strain (Equation 4.5, Figure 4.5 (b)). The  $\Delta C/C_0$  data and the stress or strain data in the first cycle of the load-unload experiment were used to calculate the  $S$  and  $GF$ .

$$S = \frac{\Delta C/C_0}{\sigma} = \frac{\Delta C}{C_0} \cdot \frac{A}{F} \quad \text{Equation 4.4}$$

$$GF = \frac{\Delta C/C_0}{\varepsilon} \quad \text{Equation 4.5}$$

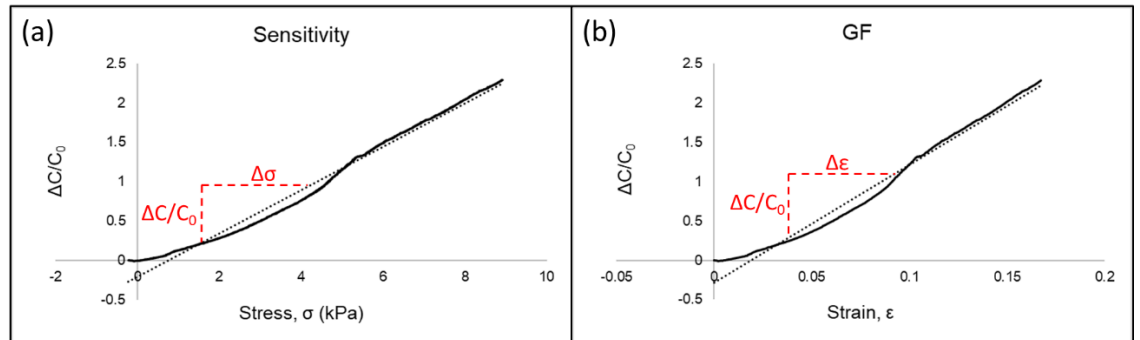


Figure 4.5 (a) Sensitivity and (b) GF of capacitive sensors.

The PGS dry sensor showed an average  $S$  of  $0.042 \text{ kPa}^{-1}$  and an average  $GF$  of  $1.59$  under  $5\%$  strain, besides, those two parameters under  $10\%$  and  $20\%$  strain are also shown in Figure 4.7 (a) and (b). Both the  $S$  and  $GF$  of the dry sensor showed good behaviour in the  $20\%$  strain measurement and a relatively rough signal in the  $5\%$  strain measurement (Appendix B, Figure B.3 and Figure B.4).

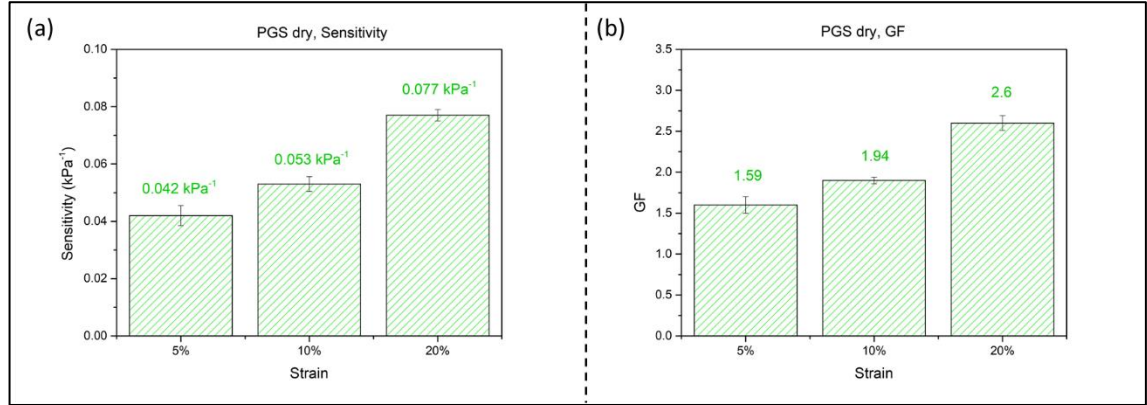


Figure 4.6 (a) Sensitivity, and (b) GF of the PGS dry sensor with strains of  $5\%$ ,  $10\%$ , and  $20\%$ .

#### 4.2.3 Static and Dynamic Electromechanical Behaviour

The static and dynamic electromechanical behaviour of the PGS dry sensor, including, response time and recovery time, repeatability, static stability, and long-term dynamic stability are present in Figure 4.7.

The response time and recovery experiment showed that electrical response could accurately follow the input mechanical solicitation and return to the original base capacitance after removing a  $5\%$  strain (Figure 4.7 (a)). The measured response time is  $272\text{ms}$ , and the recovery time is  $271 \text{ ms}$ . The stability experiment after applying  $20\%$  strain over  $3600\text{s}$  showed a small drift of  $1.4\%$  in the value of the  $\Delta C/C_0$  at the end of the experiment (Figure 4.7 (b)). The repeatability experiment showed that the sensor could return an approximate  $\Delta C/C_0$  signal range while measuring the same strain/pressure, but the measured signal at the  $20\%$  strain showed some fluctuation, which was required to be improved (Figure 4.7 (c)). Its long-term dynamic stability was stable with no observable change or drift (Figure 4.7 (d)).

Due to the limited value of  $GF$  and  $S$  and some level of noise observed in the electromechanical performance of the PGS dry sensor, it is proposed a novel sensor where the air, with a dielectric constant  $\approx 1$  [135, 146], is replaced by ethylene glycol, a liquid with a high dielectric permittivity ( $\epsilon_{EG} = 37$  [147]).

In this way, to improve the performance of the PGS sensor, a high dielectric constant liquid, EG solution, was added to the PGS dry foam.

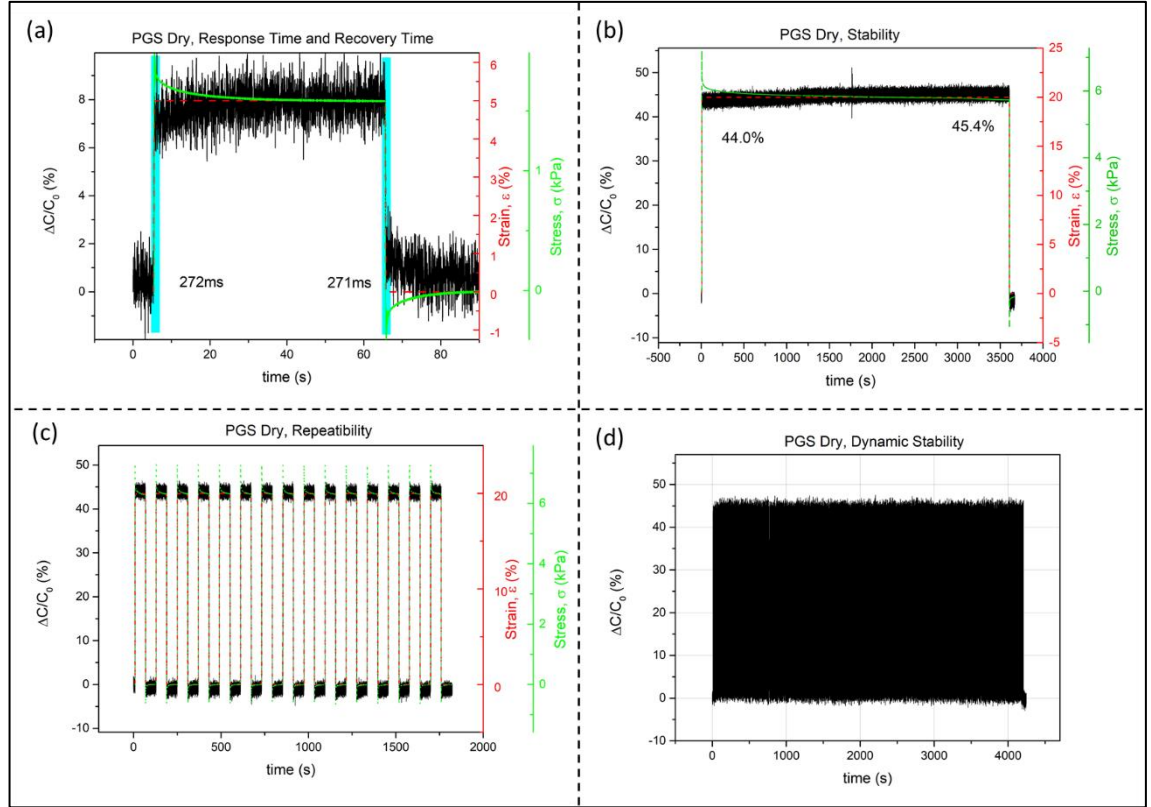


Figure 4.7 The static electromechanical behaviour, (a) Response time and recovery time, (b) Static Stability, and dynamic electromechanical behavior, (c) Repeatability, and (d) Long-term dynamic stability.

### 4.3 PGS/EG Sensor Characterization

To improve the performance of the PGS dielectric material, a 99.8% EG solution with a dielectric constant of 37 (at 20°C) [147] was added as a high dielectric constant filler into the PGS foam.

EG solution was poured into a beaker and one 13 mm PGS cylinder sample was fully immersed in the EG solution and was pressed with a tweezer to squeeze the air out and replaced with EG. Then, the beaker was put into a vacuum oven to create a vacuum environment to fill the porous microstructure with EG. By weighing, 86% by weight of ethylene glycol was in the mixture of PGS/EG (0.124g PGS: 0.764g EG). A schematic representation of the assembled sensor is presented in Figure 4.8.

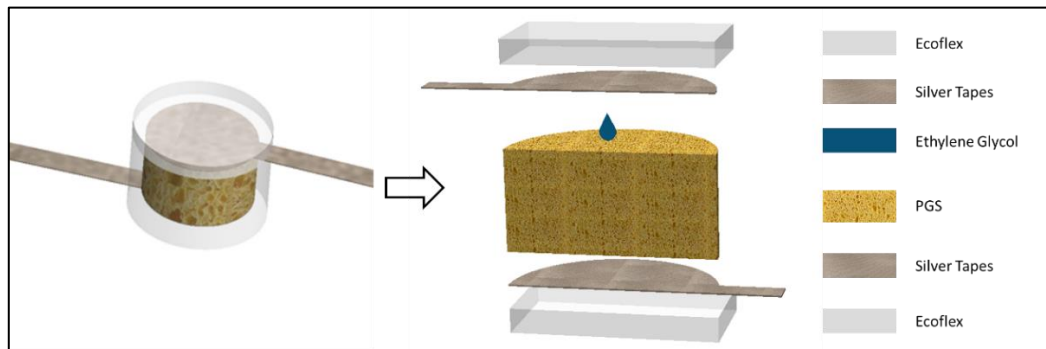


Figure 4.8 The assembling of the PGS/EG sensor.

### 4.3.1 Capacitance Change Signal in Load-unload Electromechanical Experiment

The same load-unload experiment was conducted on PGS/EG sensor. The  $\Delta C/C_0$  results under different strains and load speed conditions are shown in Figure 4.9.

Compared with the PGS dry sensor, PGS/EG sensor showed clear  $\Delta C/C_0$  signals under mild deformation (Figure 4.9 (a) and (c)) with less noise. The  $\Delta C/C_0$  reached around 47.4% and 7.0% for 20% strain and 5% strain, respectively. In this way, the addition of EG here did not improve the  $\Delta C/C_0$  value, but it enhanced the quality of the  $\Delta C/C_0$  signal acquired under mild deformation conditions.

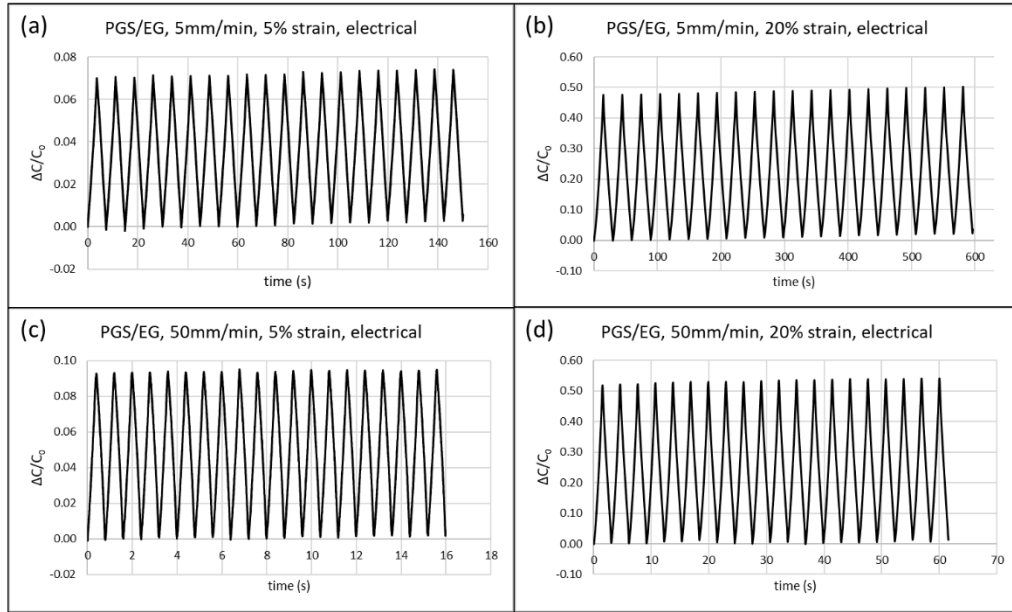


Figure 4.9 The  $\Delta C/C_0$  of the PGS/EG sensor under (a) 5 mm/min, 5% strain; (b) 5 mm/min, 20% strain; (c) 50 mm/min, 5% strain; (d) 50 mm/min, 20% strain.

### 4.3.2 Sensitivity and Gauge Factor

The PGS/EG sensor showed an average  $S$  of  $0.11 \text{ kPa}^{-1}$  and an average  $GF$  of 1.8 under 5% strain, which improved separately 2.6 times and 1.1 times when compared to the PGS dry sensor, besides, those two parameters under 10% and 20% strain are also shown in Figure 4.7 (a) and (b). Compared with those of the PGS dry sensor, the PGS/EG sensor showed a clear  $\Delta C/C_0$  signal.

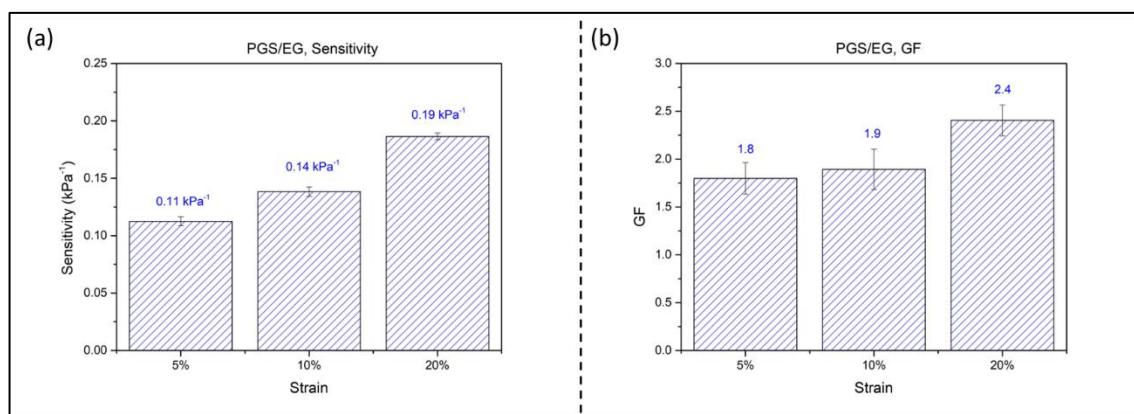


Figure 4.10 (a) Sensitivity, and (b) GF of the PGS/EG sensor with strains of 5%, 10% and 20%.

### 4.3.3 Static Stability

The static stability experiment of the PGS/EG sensor is shown in Figure 4.11. When a 20% strain was applied and kept for 3600s, the  $\Delta C/C_0$  signal started from 21.5% and increased to 22.9% 3600s (Figure 4.11), representing a 1.4% drift, which is relatively large compared with its started  $\Delta C/C_0$ . This drift could be attributed to the “Plasticizer Liquid Caused Drift” mentioned in subchapter 2.2.7.2. Ethylene glycol is used as a plasticizer agent for multiple polymers, where the molecule of the EG occupies the space between the polymer chains, and facilitates their mobility [148-150], which results in a decrease of the stress for a constant applied strain.

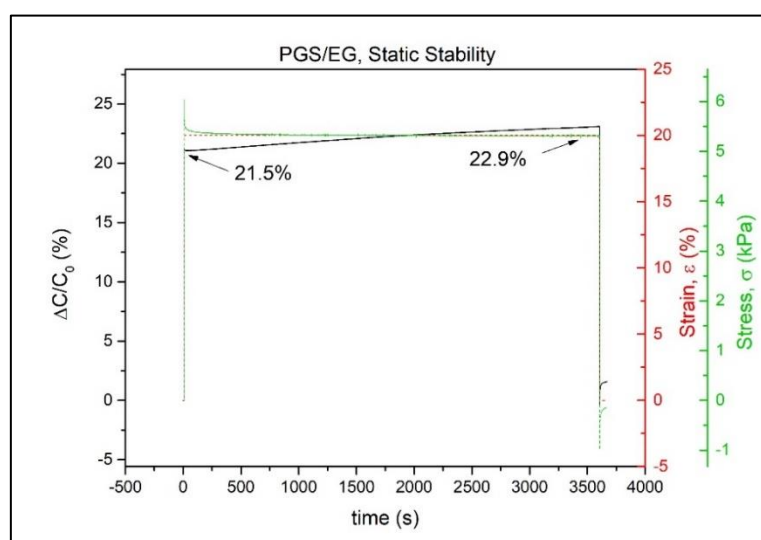


Figure 4.11 The static stability of the PGS/EG sensor.

#### 4.3.3.1 Assessment of the Drift Issue Origins

To solve the drift issue and study the effect of the EG on the electromechanical performance of the sensor, the amount of EG solution added to the PGS sensor was required to be controlled and analysed, and the optimal weight percent was needed to be studied. Four different weight percentage of EG of 0 wt%, 40 wt%, 60 wt%, and 80 wt%, based on the weight of PGS (0 g, 0.082 g, 0.185 g,

0.494 g of EG solution, respectively, based on PGS sample with 0.124g) were mixed with the PGS foams and assembled as the PGS<sub>x</sub>/EG<sub>100-x</sub> sensors, and the static stability experiments of these sensors were conducted.

According to the results shown in Figure 4.12, the  $\Delta C/C_0$  of all four sensors still show a gradual upward trend over time, but the drifts were similar when compared with the PGS/EG sensor. The drift of  $\Delta C/C_0$  difference for dry sensors was 1.4%, for PGS<sub>60</sub>/EG<sub>40</sub> sensor was 1.4%, for PGS<sub>40</sub>/EG<sub>60</sub> sensor was 4.1% and for PGS<sub>20</sub>/EG<sub>80</sub> sensor was 1.5%.

Among these sensors, the PGS<sub>40</sub>/EG<sub>60</sub> sensor showed the highest normalized  $\Delta C/C_0$  of around 220.0%, compared to 46.0% for the dry sensor, 75.0% for the PGS<sub>60</sub>/EG<sub>40</sub>, and 23.0% for PGS<sub>20</sub>/EG<sub>80</sub> sensor (Figure 4.12 (e)). This  $\Delta C/C_0$  of around 220.0% was consistent with the  $\Delta C/C_0$  of around 225.0% in its 20% strain cyclic measurement (see Appendix B, Figure B.2). The PGS<sub>40</sub>/EG<sub>60</sub> sensor had a larger absolute drift, but the percentage change of the drift was relatively low (the percentage change was 1.9% for PGS<sub>40</sub>/EG<sub>60</sub> sensor, compared to 2.2% for the dry sensor, 1.4% for the PGS<sub>60</sub>/EG<sub>40</sub> and 6.4% for PGS<sub>20</sub>/EG<sub>80</sub> sensor, as shown in Figure 4.12 (f)), which was quite acceptable within a duration of one hour, especially compared to the ones reported by Sun's [69], where a clear drift of around 7.0% (0.80 pF/11.5 pF) was observed after only 15s of static pressure.

In this way, the PGS<sub>40</sub>/EG<sub>60</sub> sensor was chosen as the ideal PGS<sub>x</sub>/EG<sub>100-x</sub> sensor to conduct the other measurements.

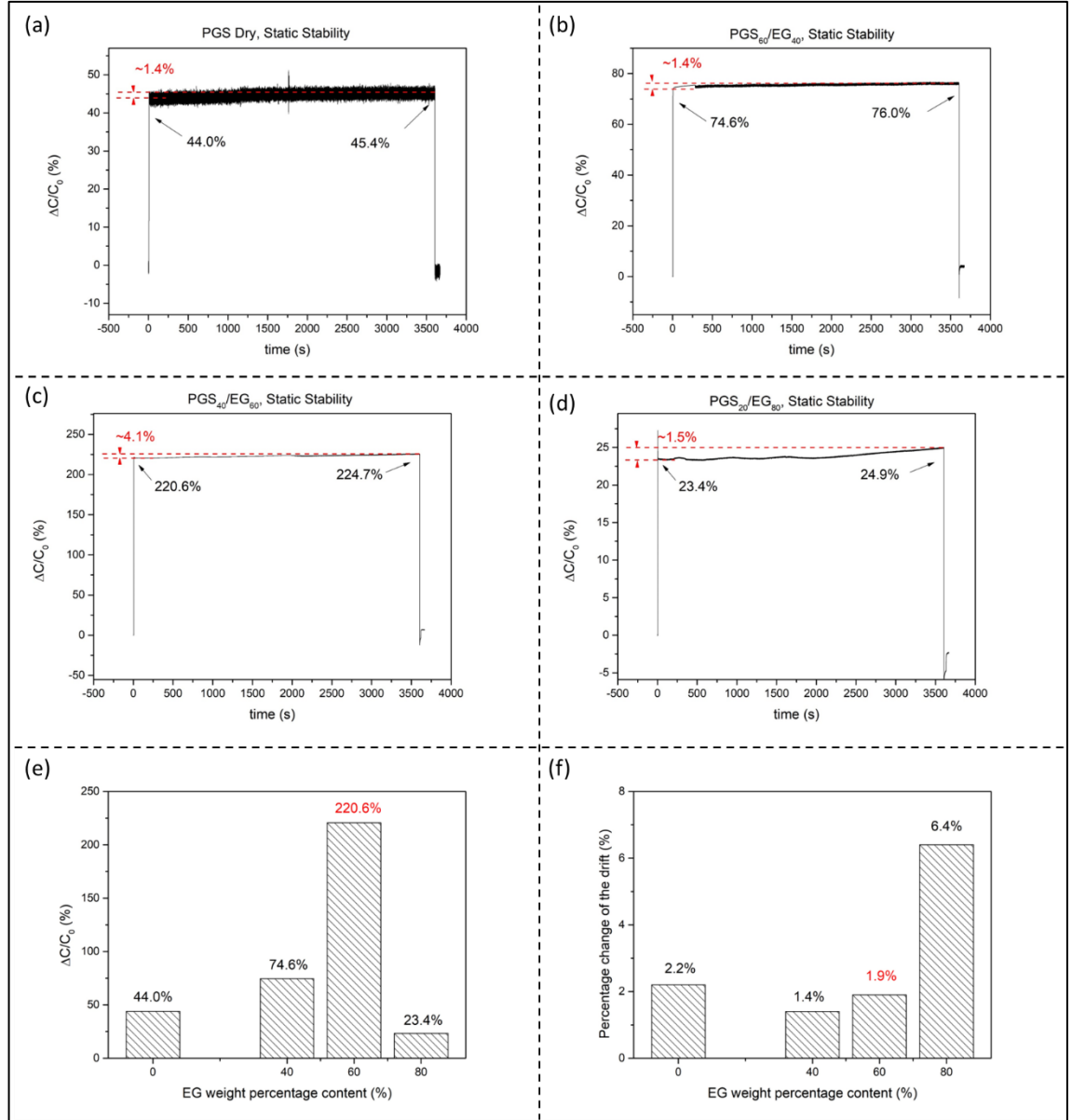


Figure 4.12 The stability of PGS sensors. (a) PGS dry sensor; (b) PGS<sub>60</sub>/EG<sub>40</sub> sensor; (c) PGS<sub>40</sub>/EG<sub>60</sub> sensor; (d) PGS<sub>20</sub>/EG<sub>80</sub> sensor. (e) Maximum  $\Delta C/C_0$  of these four sensors, (f) Maximum percentage change of the drift of these four sensors.

#### 4.3.3.2 Ecoflex Casing Influence

The Ecoflex casing was also considered as the possible reason for the  $\Delta C/C_0$  drift as its viscoelastic behaviour might cause a gradual rebound during the compression period. A control experiment where the Ecoflex cases were changed by PDMS, a popular dielectric substrate used for capacitive sensors due to its elastomeric mechanical properties, was conducted.

The PDMS casing was prepared by mixing the base material and curing material of SYLGARD™ 184 Silicone Elastomer Kit [122] with a ratio of 10:1 under room temperature for 48 hours and using the same casing preparing method and sizes shown in subchapter 3.3. Due to its remarkable performance, the PGS with 60wt% EG was used as the dielectric material (abbreviate as PDMS case sensor).



PDMS is an elastomer with a relatively high Young's Modulus compared with Ecoflex and its stress for an applied strain of 20% exceeded the maximum load of the load cell of the universal testing machine (10 N), so instead, it was applied 5% strain for both sensors, based in PDMS and Ecoflex casing to evaluate the influence of the casing material in the electromechanical stability of the sensors. According to the results gathered, the PDMS casing sample had a drift in the capacitance change from 18.1% to 21.2% (Figure 4.13 (a)), and the stress decreased from 17.4 kPa to 16.1 kPa [148-150] (Figure 4.13 (b)).

To compare this result with that of the sensor with Ecoflex casing (abbreviated as Ecoflex casing sensor), a stability experiment for the Ecoflex case sensor was also conducted in the same conditions stated for the PDMS case sensor. The results showed the same trend (Figure 4.13 (c) and (d)), with a drift in the capacitance change signal from 26.3% to 29.4%, representing around 3% in the  $\Delta C/C_0$ , while the stress decreased from 2.1 kPa down to 1.9 kPa. The obtained results showed that the material chosen to build the case of the sensor did not influence significantly the electromechanical behavior, with both sensors (PDMS case sensor and Ecoflex case sensor) presenting a drift of 3% after 3600 s of static load, suggesting that this behaviour is probably due to the plasticizing effect of EG, that facilitates the mobility and relaxation of the polymer chains [148-150].

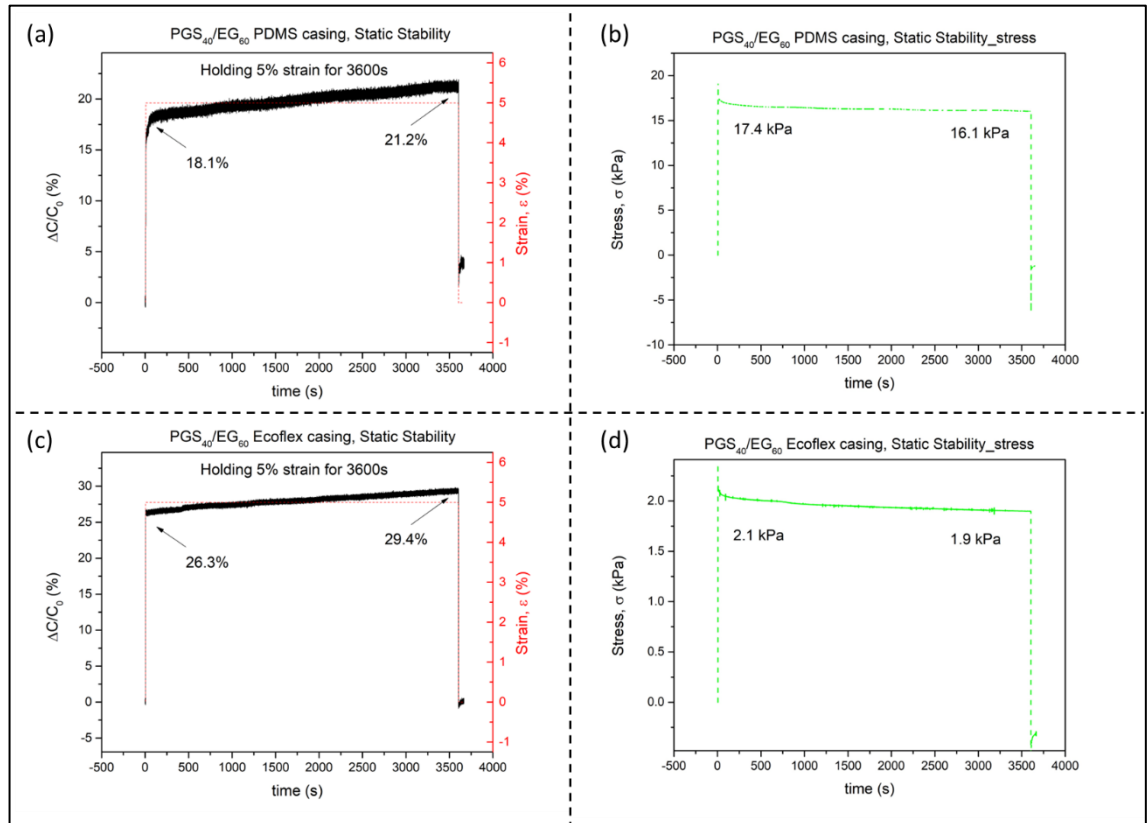


Figure 4.13 The static stability experiment of the PDMS casing sensor, (a)  $\Delta C/C_0$  and strain, (b) Stress; and the Ecoflex casing sensor, (c)  $\Delta C/C_0$  and strain, (d) Stress;

## 4.4 PGS<sub>40</sub>/EG<sub>60</sub> Sensor Characterization

Due to the outstanding performance observed for the PGS<sub>40</sub>/EG<sub>60</sub> sensor, it was chosen to explore the electromechanical properties and environmental properties. In this subchapter, all electromechanical behaviour of the PGS<sub>40</sub>/EG<sub>60</sub> sensor is presented and discussed and compared with the behaviour of the PGS dry sensor to understand the effect of 60wt% EG added to the PGS foam. Furthermore, the environmental properties, including proximity and temperature sensitivity are discussed.

### 4.4.1 Capacitance Change Signal in Load-unload Electromechanical Experiment

The load-unload experiment results for the PGS<sub>40</sub>/EG<sub>60</sub> sensor and the PGS dry sensor are shown in Figure 4.14. The incorporation of 60wt% EG improved the electrical signal output signal of the sensor, with great repeatability in all the conditions tested (different stroke speeds and applied strains). The sensor could reach the same  $\Delta C/C_0$  value in each cycle, with an outstanding performance increase in the  $\Delta C/C_0$ . The PGS<sub>40</sub>/EG<sub>60</sub> sensor had around 240.0%  $\Delta C/C_0$  in 20% strain experiment, 90.0%  $\Delta C/C_0$  in 10% strain experiment, and 30.0%  $\Delta C/C_0$  in 5% strain experiment. The  $\Delta C/C_0$  measurements of the PGS<sub>40</sub>/EG<sub>60</sub> sensor under all conditions are shown in Appendix B, Figure B.2.

When a mild deformation was applied to the sensor ( $\varepsilon = 5\%$ ), the  $\Delta C/C_0$  output signal showed a remarkable increase, from 0.09 for the dry sensor, up to 0.33 for the PGS<sub>40</sub>/EG<sub>60</sub> sensor, representing an improvement in the electromechanical performance of more than 3-fold (Figure 4.14 (a) and (c)), which is a promising feature for applications where smooth movements are involved like a heart beating or breathing patterns.

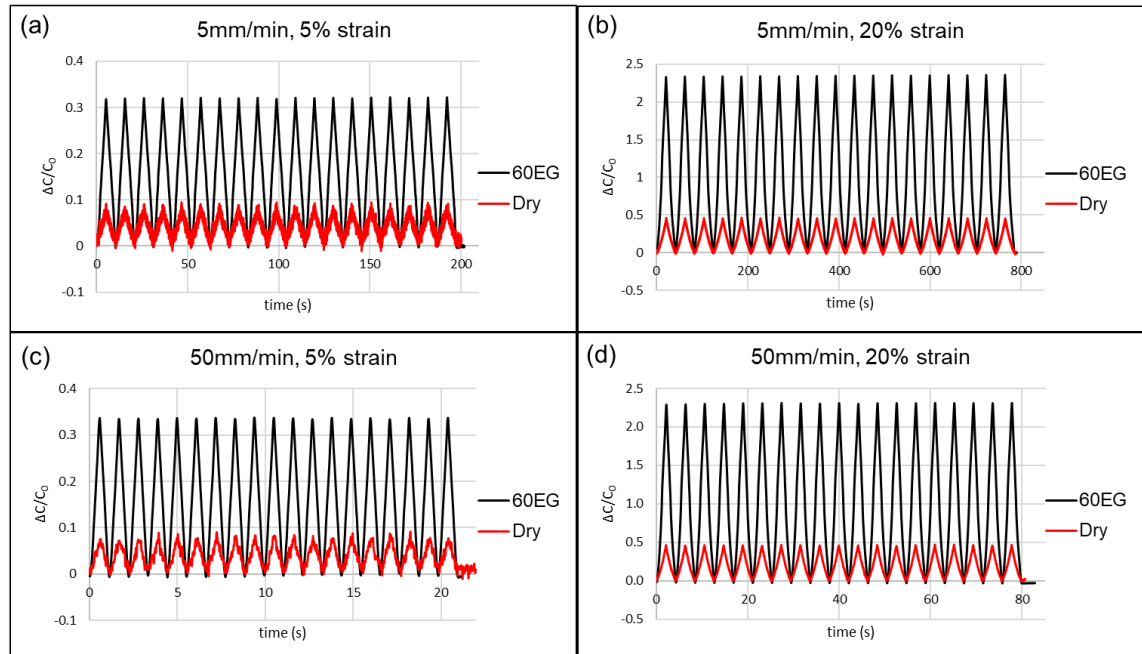


Figure 4.14 The  $\Delta C/C_0$  of the PGS<sub>40</sub>/EG<sub>60</sub> sensor vs. the PGS dry sensor under (a) 5 mm/min, 5% strain; (b) 5 mm/min, 20% strain; (c) 50 mm/min, 5% strain; (d) 50 mm/min, 20% strain.

#### 4.4.2 Sensitivity and Gauge Factor

S and GF of the PGS<sub>40</sub>/EG<sub>60</sub> sensor under all conditions were summarized in Figure 4.15 and Figure 4.16, compared with those of the PGS dry sensor. According to the result, the addition of 60wt% EG improves the electromechanical performance under all strain conditions as can be seen by the remarkable increase in S and GF.

The linearity,  $R^2$ , of the S and GF curves demonstrates the fitting relationship between the  $\Delta C/C_0$  and stress or strain. High  $R^2$  indicated the ability of the sensor to precisely measure the deformation or the pressure. The incorporation of the 60wt% EG improved the S and GF performance from 95% to around 98% in the high and medium strain experiment (Appendix B, Figure B.5 and Figure B.6). For the mild strain experiments, these curves for the PGS<sub>40</sub>/EG<sub>60</sub> sensor both showed clear fitting relationships with a high  $R^2$  of around 99%, which indicated that the addition of 60wt% EG, clearly improves the sensor reliability and performance.

The PGS<sub>40</sub>/EG<sub>60</sub> sensor showed an average S of 0.27 kPa<sup>-1</sup> and an average GF of 15.0 under 5% strain, which improved separately 3.5 times and 4.9 times when compared to the PGS dry sensor. This enhanced the capability of the sensor to accurately measure mild deformations or pressures. The S and GF showed an increasing trend with the increasing strain volume. The S and GF of those sensors under all speed conditions are shown in Appendix B, Figure B.5 and Figure B.6. Under different force speeds or deformation speeds, the PGS<sub>40</sub>/EG<sub>60</sub> sensor showed an excellent capability to return the base capacitance, which is a desirable feature for sensor applications like pulse or heart beating, that is associated with smooth deformation, and required sensors with great sensitivity or gauge factor.

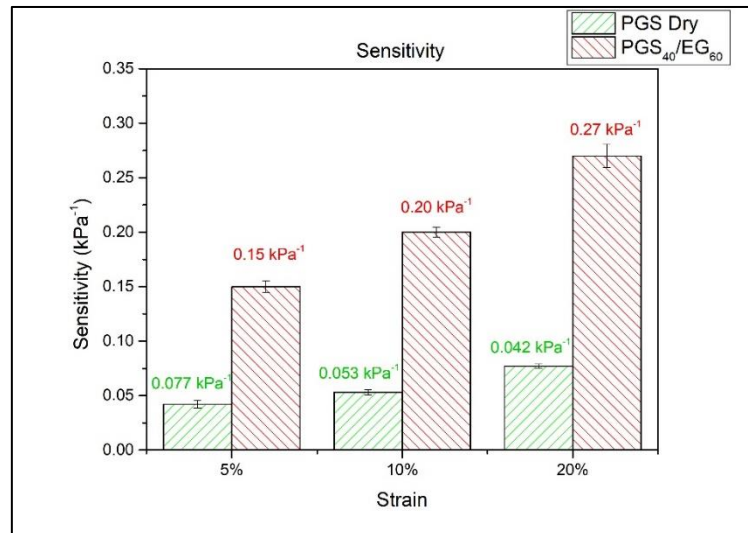


Figure 4.15 S of the PGS dry sensor and PGS<sub>40</sub>/EG<sub>60</sub> sensor with strains of 5%, 10% and 20%.

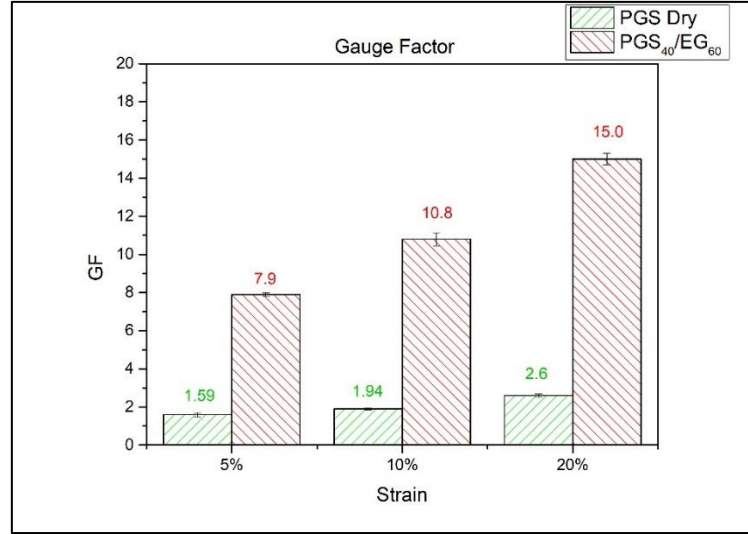


Figure 4.16 GF of the PGS dry sensor and PGS<sub>40</sub>/EG<sub>60</sub> sensor with strains of 5%, 10% and 20%.

Compared with the present wearable sensors, where a decrease in the sensitivity when the stress range is increasing (Table 2.3) was observed, this behaviour was attributed to the larger stress required to cause the same change in the electrical signal output [115]. As opposed to the present capacitive sensors, our sensor showed an opposite trend in that its sensitivity increased with the stress increasing. This could be attributed to the increasing relative permittivity. When the stress is increasing, the PGS porous sample was compressed and the porosity is decreased, which causes the increase in relative permittivity [135]. In this way, the capacitance value increased, and so did the sensitivity.

#### 4.4.3 Response Time and Recovery Time

The response and recovery time measures the time needed by the sensor to react and return an electrical ( $\Delta C/C_0$ ) signal when the strain/pressure signal was applied and released. This time delay happens in all polymer-based sensors due to the viscoelastic nature of the polymer material [50]. A 90% time constant is commonly used as the standard response time, and the human skin presents a response between 30 - 50ms [48]. During the development of new sensors for wearable applications, these values should be considered to mimic the skin properties.

As shown in Figure 4.17, after applying and removing a 5% strain, the response time and recovery time of the PGS<sub>40</sub>/EG<sub>60</sub> sensor were 209 ms and 230 ms respectively, which is similar to those of the present capacitive sensors (Table 2.3).

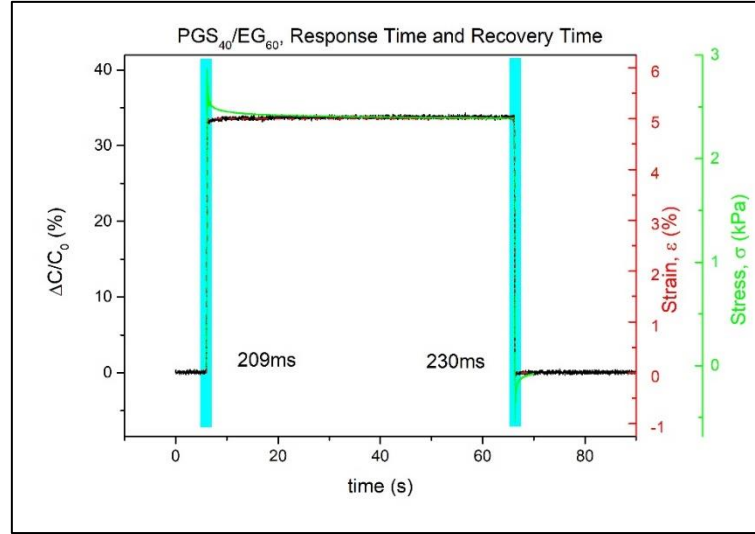


Figure 4.17 The response and recovery time of the PGS<sub>40</sub>/EG<sub>60</sub> sensor (Represented by blue bars widened for ease of display).

#### 4.4.4 Repeatability

In the repeatability experiment with applying 20% strain in each cycle (Figure 4.18), the PGS<sub>40</sub>/EG<sub>60</sub> sensor showed almost the same  $\Delta C/C_0$  after each individual cycle with an average  $\Delta C/C_0$  value of 237.2 % and a standard deviation of 0.8%, and the  $\Delta C/C_0$  could return to their initial base values when the strain was released. The  $\Delta C/C_0$  data during the repeatability experiment is shown in Appendix B, Table B.2.

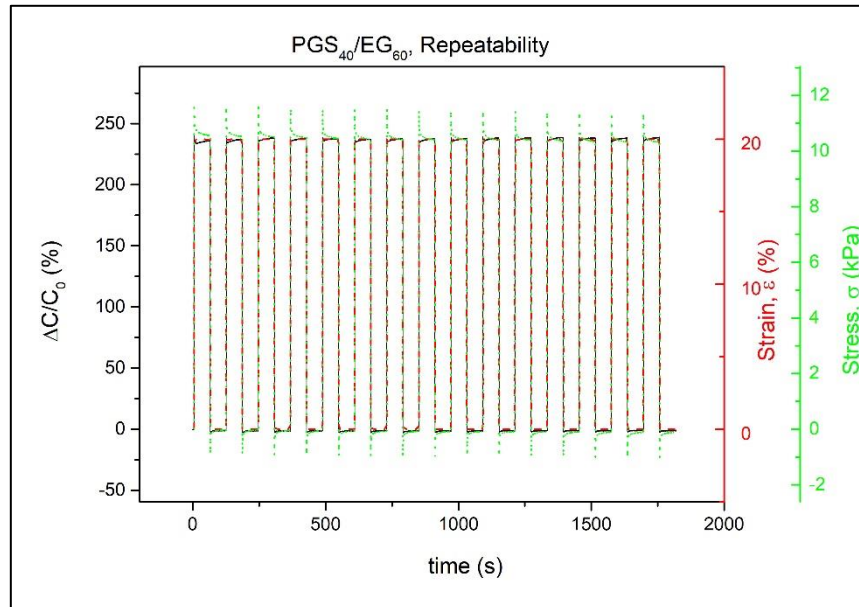


Figure 4.18 The repeatability experiment of the PGS<sub>40</sub>/EG<sub>60</sub> sensor.

#### 4.4.5 Long-term dynamic stability

As shown in Figure 4.19 (a), the PGS<sub>40</sub>/EG<sub>60</sub> sensor presented a stable electromechanical behaviour and  $\Delta C/C_0$  was increased by 4.7%, after 1000 dynamic cycles with 20% strain applied. The stress

also suffered a small decrease, from 10.6 kPa down to 10.3 kPa, which was due to the viscoelastic nature of the polymers used, the plasticizing effect of the EG, and some mechanical energy that was lost through heat due to the mechanical hysteresis of the polymeric materials.

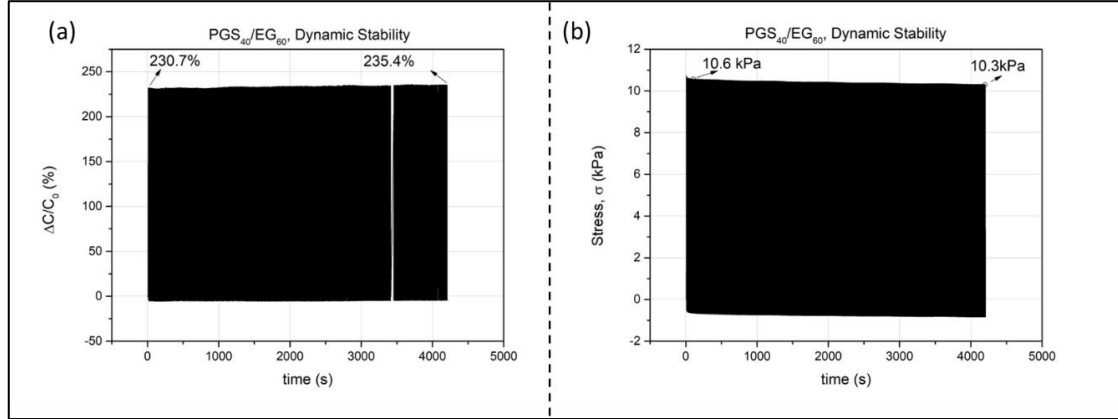


Figure 4.19 The dynamic stability experiment of the PGS<sub>40</sub>/EG<sub>60</sub> sensor, (a) The  $\Delta C/C_0$  vs. time curve; (b) The stress vs. time curve.

#### 4.4.6 Environmental Behaviour

##### 4.4.6.1 Proximity

For the proximity experiments (200 mm, 80 mm and 50 mm proximity experiments), an initial average capacitance (the average of the capacitance value at the first five seconds), was used as  $C_0$  due to the inaccurate individual  $C_0$ . To show the relationship between distance and  $\Delta C/C_0$ , the normalized change in capacitance was preceded by the negative sign to become the decreased  $\Delta C/C_0$ , which is  $-\Delta C/C_0$ , so that it has the same increasing trend as the distance. The  $\Delta C/C_0$  curve and distance curve were combined by matching both the start point and end point of the 60 s rest period.

During the proximity experiments (Figure 4.20 (a), (c), and (e)), the capacitance value was decreased during the approaching of the pressure head as mentioned in subchapter 2.2.7.1. The maximum  $-\Delta C/C_0$ s were 11.9%, 11.9%, and 11.6% for 200 mm, 80 mm, and 50 mm proximity experiments, respectively, while the pressure head almost touched the sensor. These  $-\Delta C/C_0$ s were almost the same which demonstrated their good proximity repeatability.

To describe the proximity behaviour of the sensor, a concept of “proximity point” is needed as a criterion to determine whether the sensor presented a sufficient signal change to be considered to have detected an approaching item. The proximity point here was set as a  $-\Delta C/C_0$  of 0.5%, which means that during the item approaching process, when the  $-\Delta C/C_0$  signal of the sensor reached 0.5%, it is considered that the sensor detects the approaching item, and the current distance between the approaching item and sensor is the “proximity distance”.

The proximity distance was calculated by the initial distance between the pressure head and sensor minus the distance that the pressure head moved ( $-\Delta C/C_0$  signal rise to 0.5%). For instance, in the 200 mm proximity experiment, when the  $-\Delta C/C_0$  signal rise to 0.5%, the pressure head moved 154.8

mm, so the proximity distance is  $(200 - 154.8) \text{ mm} = 45.2 \text{ mm}$ . According to the results shown in Figure 4.20 (b), (d), and (f), the proximity distances were 45.2 mm, 41.8 mm, and 32.5 mm for 200 mm, 80 mm, and 50mm experiments, separately. These results demonstrated the sensor's good proximity, that the sensor can detect approaching items from around 40 mm distance.

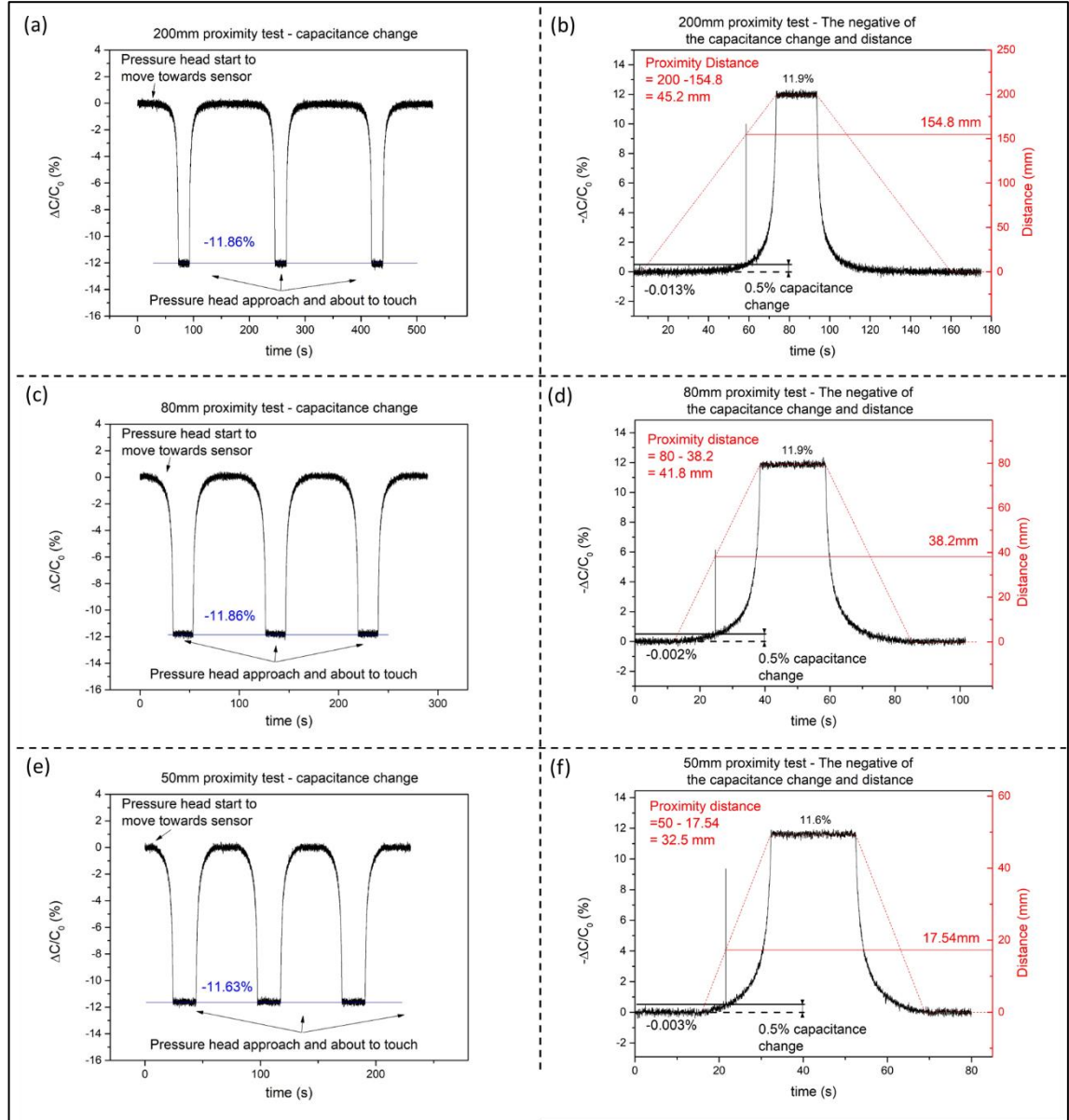


Figure 4.20 Capacitance change in proximity experiment, (a) 200mm proximity experiment; (c) 80mm proximity experiment; (e) 50mm proximity experiment. The negative of the capacitance change combined with distance, (b) 200mm proximity experiment; (d) 80mm proximity experiment; (f) 50mm proximity experiment.

#### 4.4.6.2 Temperature Sensitivity

Figure 4.21 shows the  $\Delta C/C_0$  value change over the set temperature between 25 – 70 °C. When the temperature increases, the value of the  $\Delta C/C_0$  increases linearly with a relationship of:

$$\frac{\Delta C}{C_0} = 0.62 \cdot T - 14.83 \quad \text{Equation 4.6}$$



which means that a 1°C temperature increase could cause a  $\Delta C/C_0$  increase of 0.62%. The results showed that it could be possible to use the developed sensor to monitor body temperature to detect early signs of body temperature changes like fever, for instance.

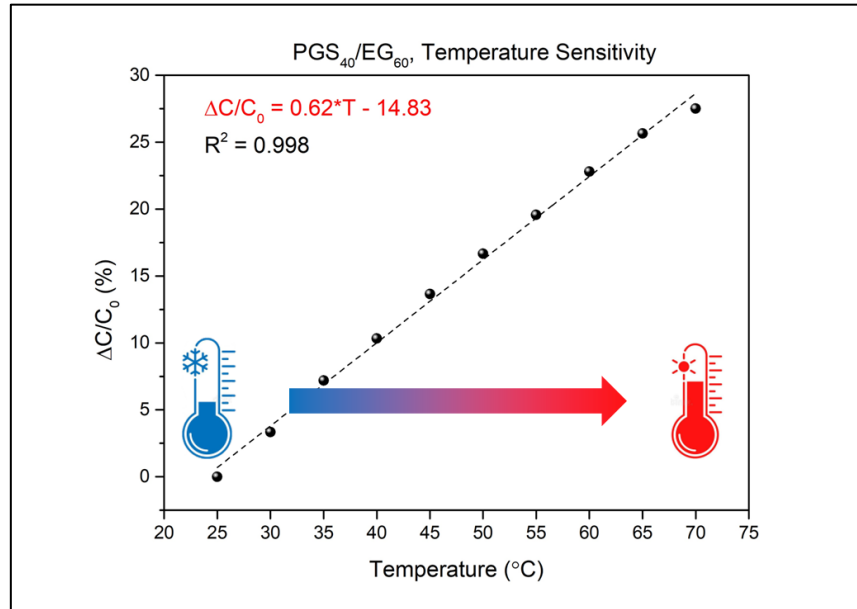


Figure 4.21 The change of  $\Delta C/C_0$  over the temperature.



## Chapter 5 Sensor's Potential for Wearable Applications

The capacitive sensor can transform the pressure/mechanical input into an electrical signal, which means many mechanical signals, such as deformation, and pressure can be measured by this type of sensor. Up to now, many capacitive sensors were studied to monitor human motion or detect physiological signals by attaching the sensor to different parts of the body. In this chapter, several demonstrations of the PGS<sub>40</sub>/EG<sub>60</sub> capacitive sensor are introduced, like finger bending monitoring, breathing, heart beating measurement, proximity, temperature monitoring, and weight measurement detection are presented (Figure 5.1). The choice for the PGS<sub>40</sub>/EG<sub>60</sub> capacitive sensor was due to its outstanding sensitivity and gauge factor revealed by this device, as discussed in Chapter 4.

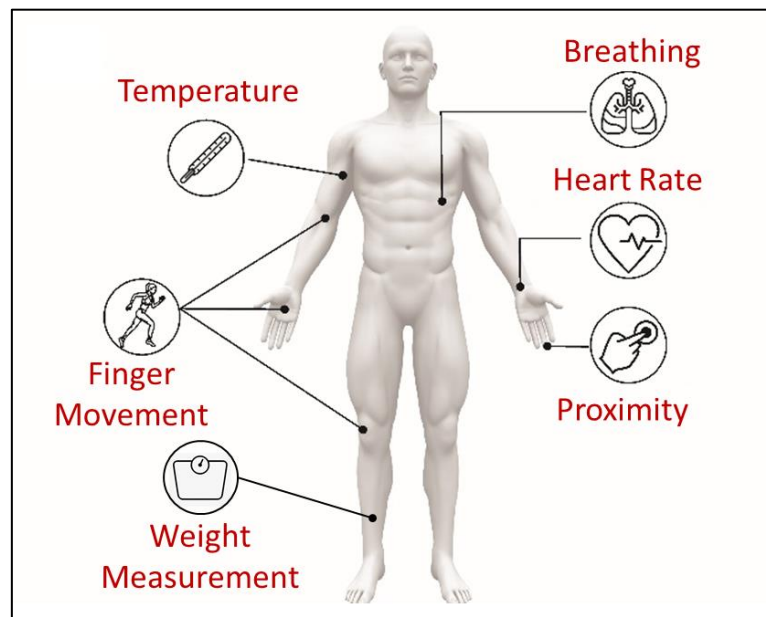


Figure 5.1 Sensor's potential for wearable application.

### 5.1 Finger Bending Monitoring

With the help of the capacitive sensor to monitor the human body movement, the user could monitor their body to know the arm moving pattern and leg walking and running gestures and speed during different sports, rehabilitation, or other activities. Patients and clinicians could use these devices to monitor and diagnose the causes of limb injuries and the degree of the trauma to the body, or this body movement information could be transferred and used to achieve a virtual action or remote control.

Here, the sensor was attached to the index finger of the left hand of the volunteer as shown in Figure 5.2 (a) – (d) and the bending movement was monitored to show up the performance of the PGS<sub>40</sub>/EG<sub>60</sub> sensor. The index finger was bent to different angles to simulate different actions of fingers during daily life actions. The change of  $\Delta C/C_0$  over time during the finger bending process is shown in Figure 5.2 (e). While the finger bent to 41°, 51°, 58°, and 73°, the sensor presented

$\Delta C/C_0$  of 85.8%, 142.0%, 183.9%, and 331.4%. By fitting these two data (Figure 5.2 (f)), a relationship of “bending angle =  $7.72 \cdot (\Delta C/C_0) - 244.65$ ” was obtained with an  $R^2$  of 98.8%.

This sensor could accurately measure the finger bending angle by converting the pressure resulting from the finger bending movement, to an analyzable  $\Delta C/C_0$ . This performance could find diverse applications in the biomedical field. For instance, the sensor can be worn by patients with fractures to monitor the movement of the body and provide information if secondary trauma happens and avoid it in the future, or even people could wear it in daily life, and clinicians could have enough information about how the body trauma happened and have a measurement of the healing process. Further, the sensor revealed features for virtual reality applications, where the action of fingers and movement could be recorded and projected into computer animations, and remote control applications.

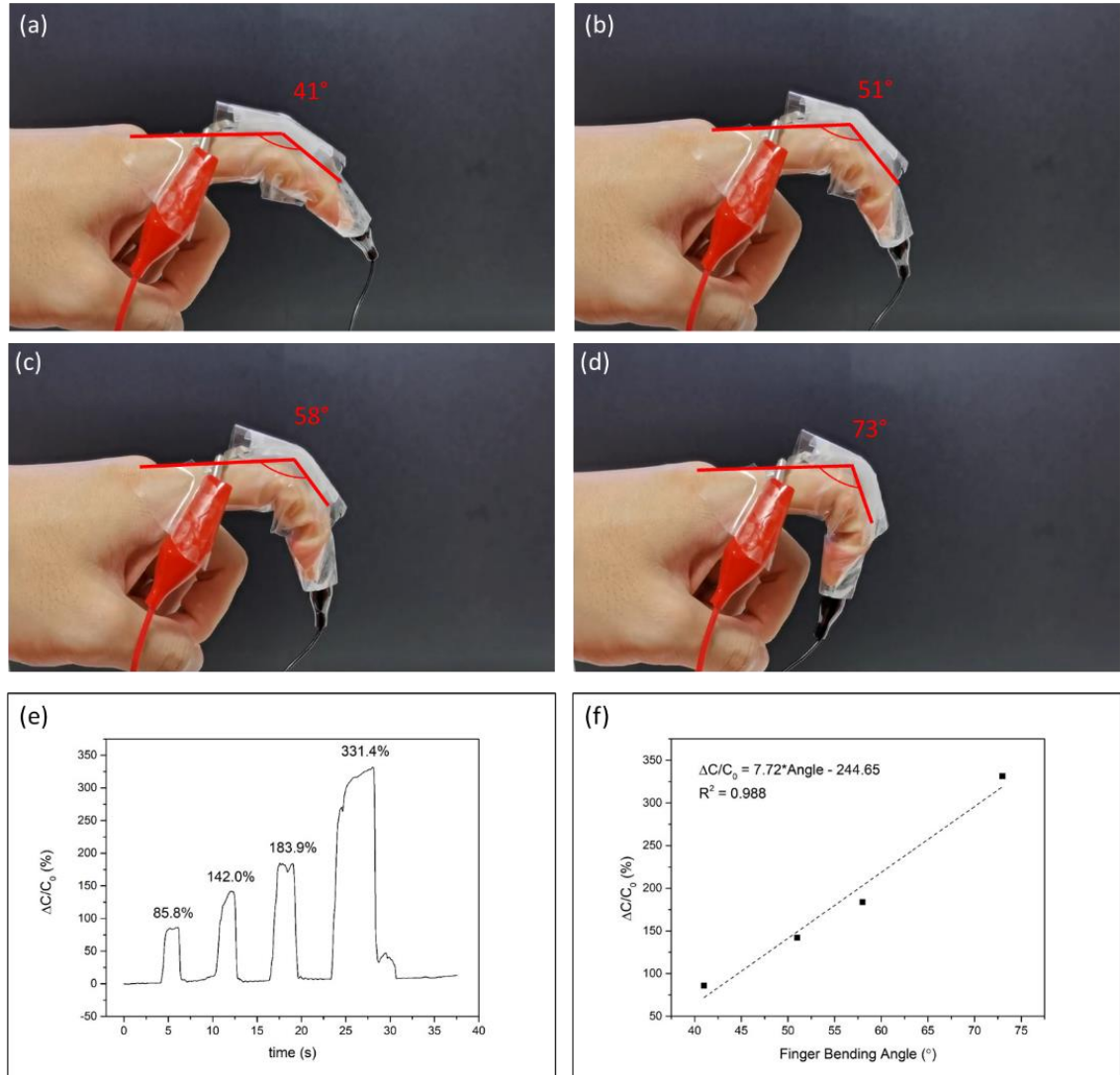


Figure 5.2 Finger bending to degrees of (a) 41°, (b) 51°, (c) 58°, (d) 73° while recording (e)  $\Delta C/C_0$  vs. time; (f)  $\Delta C/C_0$  vs. Finger Bending Angle.

## 5.2 Breathing Measurement

Human pulmonary respiratory patterns, including inhaling and exhaling time, and breathing rate, can be obtained by wearable sensors. This information could help to monitor respiratory function and provide information about the potential respiratory-related disease. Due to the Hawthorne effect (that the peoples' behaviour might change while knowing they are studied or observed in the field or laboratory [151]), the user of the traditional breathing measurement devices like the spirometer might show a different respiratory pattern during their measurement period, and this can raise issues during the diagnosis of the respiratory condition. The soft and comfortable wearable sensors could let the user ignore the existence of sensors and behave as usual, with minimal interference in daily activities, over long periods of time and monitor the breathing pattern continuously.

The sensor was attached to the skin above the 10<sup>th</sup> ribs of a volunteer (which has the biggest degree of fluctuation during breathing) to record the chest heaves (Figure 5.3 (a)). When the inhaling happened, the chest was filled with air and expanded, thus, applying pressure to the sensor that was observed by an increase in the  $\Delta C/C_0$ , and vice versa, the normalized capacitance change decreased while exhaling, associated with the chest contraction movement. Figure 5.3 (b) shows the change in  $\Delta C/C_0$  as the volunteer breath over different breathing activities.

During the breathing activities, eight normal breaths were taken, then a deep breath and hold, three deep breaths, followed by a breath-holding, and finally a slow inhalation and exhalation. The normal breathing showed a clear  $\Delta C/C_0$  of around 0.69%. The first seven normal breaths were recorded in around 31.9 seconds, which can be converted to around 13 breaths per minute. This data was in the range of the normal respiratory rate for a healthy adult (around 12-20 breaths per minute) [152]. For the normal breath pattern in the recorded data, one breath cycle had an inhalation and exhalation period taking around 1.6 seconds, a rest period taking around 2.9 seconds, and one whole breath cycle taking around 4.5 seconds (Figure 5.3 (b), average data of the first seven breath cycles expelled one max data and one min data). During the deep breathing period, the  $\Delta C/C_0$  increased to around 4.36%. Besides, in the deep-breath & hold step and slow breath step, the sensor clearly showed the expansion and contraction of the chest, suggesting that the sensor could record the change of lung volume during the respiratory process.

In the future, it could be designed as a wearable sensor to monitor breath activities and provide information about lung volume performance, which can help people notice the possible symptoms of respiratory diseases and get prompt treatment.

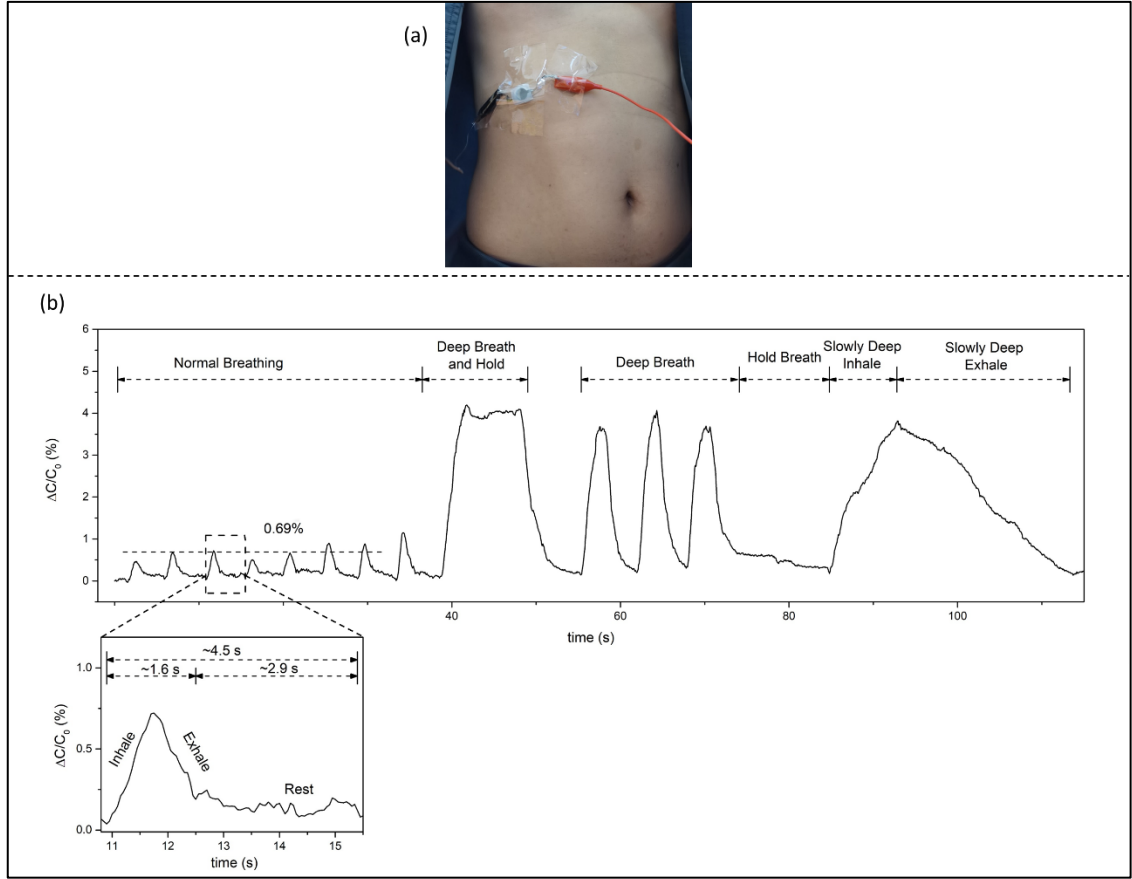


Figure 5.3 Breathing measurement. (a) The PGS<sub>40</sub>/EG<sub>60</sub> sensor was attached to the skin above the 10<sup>th</sup> ribs of the volunteer and (b) measured the breath action and partial enlargement of one breath cycle.

### 5.3 Heart Beating Measurement

The pulse is one of the most significant physiological signals to monitor early signs of stress, or physical activity performance and detect potential diseases like a stroke. Three groups of parameters related to heart conditions will be discussed here, which are three peaks of the pulse, the radial augmentation index (A<sub>Ir</sub>), and the stiffness index (SI). The pulse cycle presents up to three peaks, the percussion peak (P-peak), tidal peak (T-peak), and diastolic peak (D-peak) (Figure 5.4), representing the systolic and diastolic blood pressure, the late systolic augmentation [45].

Another useful parameter is the A<sub>Ir</sub> [48, 84, 113, 153], which is related to arterial stiffness [45] and vascular aging [153]. Refer to the work (Figure 5.4) from Katsuhiko Kohara et al. [153], and replace the blood pressure value (SBP and DBP value in Figure 5.4) with the capacitive value (CSBP and CDBP), the A<sub>Ir</sub> could be calculated by:

$$A_{Ir} = \frac{CSBP2 - CDBP}{CSBP1 - CDBP} \quad \text{Equation 5.1}$$

where CDBP = capacitance value of diastolic pressure, CSBP2 = the second peak (T-peak) systolic blood pressure or tidal peak, and CSBP1 = the first peak (P-peak) systolic blood pressure or percussion peak.

The stiffness index could be related to age and heart health. As we get older, the stiffness of the arteries increases, which is also a symptom of patients with heart-related diseases, e.g. coronary artery disease, myocardial infarction, and heart failure [154]. The SI can be measured by the time interval between the P-peak and T-peak ( $\Delta T_{DVP}$ ) and it is also directly related to the height ( $h$ ) of the volunteer according to:

$$SI = \frac{h}{\Delta T_{DVP}} \quad \text{Equation 5.2}$$

This signal could be retrieved by attaching the sensor to the neck, wrist, or other pulse-sensitive places, and monitoring the smooth movements of the skin to determine the pulse.

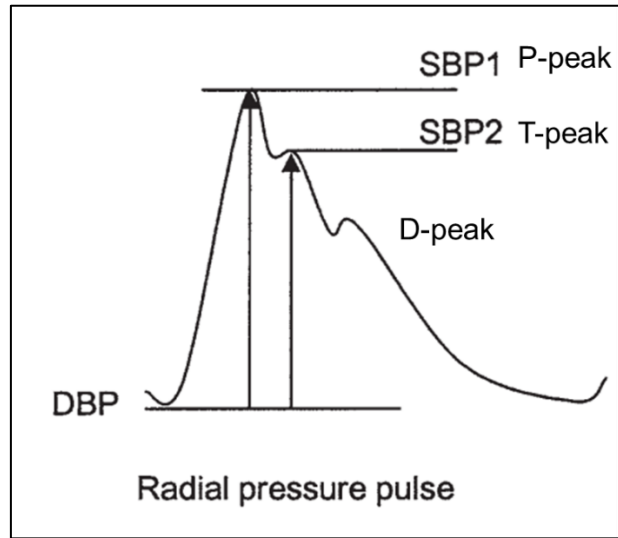


Figure 5.4 Radial augmentation index (reprinted with permission from Ref. [153]), where SBP2 and SBP1 represent the systolic blood pressure of the second peak and first peak, and DBP was the diastolic blood pressure.

To measure the heart beating, the PGS<sub>40</sub>/EG<sub>60</sub> sensor was placed on the right wrist of a volunteer where the strongest pulse was located, and the index and middle fingers of the left hand give a pressing force to the sensor to simulate the Pulse Diagnosis process. A 17.5 s period of the change of  $\Delta C/C_0$  over time of the sensor was intercepted in Figure 5.5 to show the pulse measuring process. The sensor record a pulse of 66 beats per minute (bpm). The pulse waveform showed one clear pressure peak (percussion peaks, P-peak) and one rough peak (tidal peaks, T-peak). According to Equation 5.1, an AIr of 77% and a time delay of 266 ms between P-peak and T-peak ( $\Delta T_{DVP} = t_2 - t_1$ ), were obtained using the data from the 3<sup>rd</sup> cycle, and this data is in the reasonable range of a male ( $69.5 \pm 16.3$  [155]). According to Equation 5.2, a SI of 7.0 m/s was calculated, and this data had a slight difference from one reported in the literature ( $4.33 \pm 1.27$  m/s for age 18-29 and  $5.38 \pm 1.73$  m/s for age 30-39 [156])

During the measurements, the PGS<sub>40</sub>/EG<sub>60</sub> sensor was required to be located in the position of a clear pulse, and pressure was needed to be applied to the sensor to ensure good contact between the sensor and the volunteer skin. The measured  $\Delta C/C_0$  signal can be related to pulse as long as the contact between the pressure sensor and the body is consistently maintained [44]. The mislocation

or uneven pressure could cause an unrecognized or fluctuating signal. Nevertheless, while the PGS<sub>40</sub>EG<sub>60</sub> sensor was utilized correctly, it could detect the mild deformations of the human skin caused by the pulse. It could detect two peaks of a pulse which could be used to calculate the A<sub>Ir</sub> and SI parameters. This performance shows the outstanding performance of the sensor to be used as a wearable heart beating device in the healthcare field.

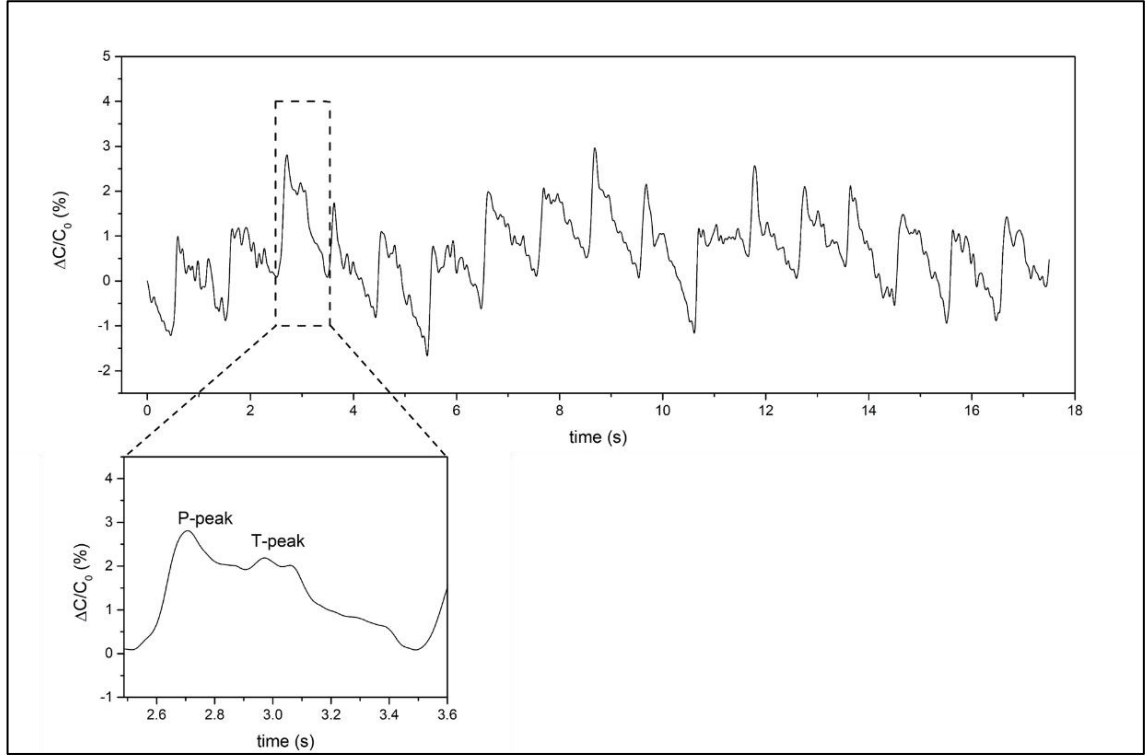


Figure 5.5 The 17.5 s pulses recorded from the volunteer and partial enlargement of one pulse cycle.

## 5.4 Proximity

The function of proximity can let the sensor “see” the approaching items, which is important for soft robotic and human-machine interface applications. The current robots can apply force to grab or lift items, but they are also required to know the distance between them and the items to know when to start applying force to conduct the grabbing action, and also avoid collision with the surrounding objects and people and a sensor with the function of measuring proximity could be a useful tool for this application.

The proximity performance was measured by moving the human finger up and down over the PGS<sub>40</sub>/EG<sub>60</sub> sensor. Figure 5.6 showed the change of  $\Delta C/C_0$  during the finger movement over time. According to the result, the sensor could detect the finger from 30 mm ( $\Delta C/C_0$  had a clear decrease on 30 mm), and this fitted the result of the proximity behaviour in subchapter 4.4.6.1. When the finger moved from 30 mm above the sensor to almost touching the sensor, the  $\Delta C/C_0$  had a sharp decrease with an (absolute value) increasing slope. The sensor can accurately detect a rapid movement without visible delay, and even the trembling of the volunteer’s finger during measuring

can be shown clearly.

This result could endow next generation robots with a more friendly and smarter performance. Owning the ability to both detect force and proximity could also handle the problem of combining many different sensors with different functions which causes a redundancy volume and burden. Other than the robot application, this proximity function could also be used in beverage production (detect the volume of liquid inside the vessel or bottle), and proximity switch, among many other potential applications.

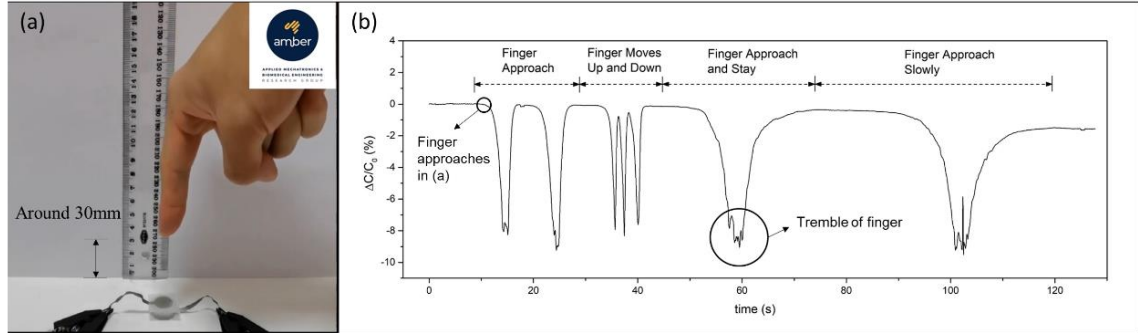


Figure 5.6 Proximity. (a) The sensor could detect the approaching of the finger of around 30mm. (b) The  $\Delta C/C_0$  during the proximity experiment.

## 5.5 Temperature Monitoring

The wearable sensor with a temperature monitoring function could identify the temperature change of the attached surface. In this way, real-time temperature change could be monitored and recorded such as body temperature, long-time working devices that require a controlled temperature, and irregular high temperatures or low temperatures could be detected and warn users or the product managers on time.

The PGS<sub>40</sub>/EG<sub>60</sub> sensor was attached to an empty beaker at a room temperature of around 20°C. To mimic the temperature change, moderate amounts of cold water ( $\cong 0^\circ\text{C}$ , ice-water mixture) and hot water (the T at the pouring moment was around 100 °C as it was boiling water stored in a thermos) were separately poured into the beaker. The PGS<sub>40</sub>/EG<sub>60</sub> sensor at room temperature showed a stable capacitance of 5.34 pF, and this was used as the  $C_0$  for all the data processing in this subchapter. Figure 5.7 (a) presents that after the cold water pouring (a cube of ice was put into the cold water to keep the temperature at 0°C), the  $\Delta C/C_0$  of the sensor kept decreasing, and after 500 s, the  $\Delta C/C_0$  decreased to -13.8%, from which the temperature could be calculated as  $1.6^\circ\text{C}$  ( $\frac{-13.8\%+14.833\%}{0.62\%}^\circ\text{C}$ ) by using Equation 4.6. Then, the cold water was removed and the empty beaker was placed to rest for a while to let it recover to room temperature., and the  $\Delta C/C_0$  during this process recovered from -14.2% to -9.3%, as shown in Figure 5.7 (b). The calculated temperature before and after recovery was 1.0 °C and 8.9 °C, which indicated the temperature of the beaker wall didn't recover to room temperature, and this was due to the low thermal conductivity of the glass and the slow thermal convection heating of air.

Finally, boiled water was poured into the beaker as shown in Figure 5.7 (c). The sensor could monitor the temperature increase until reaching a maximum change in  $\Delta C/C_0$ , followed by a decrease due to the heat exchange between the hot water and the environment. The  $\Delta C/C_0$  of the sensor increased from around -9% to 22% within 340 s due to the increased temperature, and according to Equation 4.6, it corresponds to around 60 °C.

The PGS<sub>40</sub>/EG<sub>60</sub> sensor has an excellent temperature measurement ability. According to the above demonstration, after building the relationship between its  $\Delta C/C_0$  with the temperature, it can measure the temperature with great accuracy. It can be applied in many temperature monitoring situations, such as enabling the robot or prosthetic hand to detect and distinguish hot or cold surfaces, avoiding component damage, and mimicking the somatosensation of human skin that senses the temperature change. The sensor could be attached to the human body and monitor the temperature and raise alarms to prevent heatstroke in summer, patients with a fever could be monitored in real-time so a timely diagnosis and treatment could be performed.

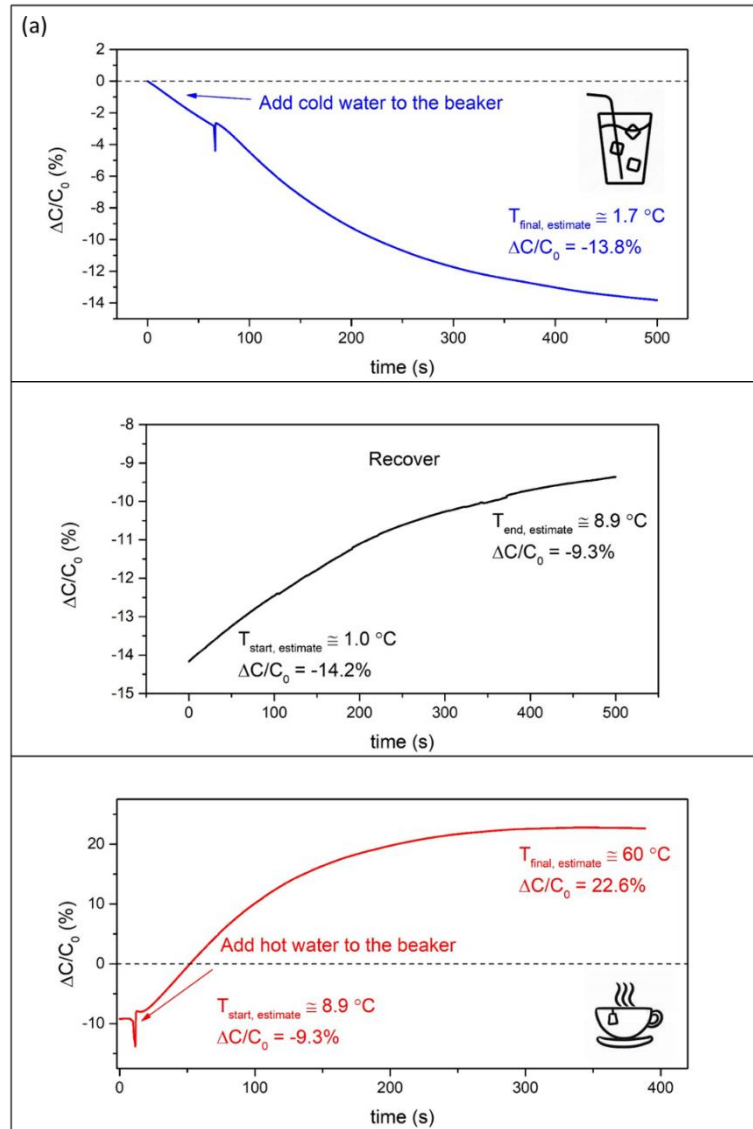


Figure 5.7 The  $\Delta C/C_0$  change of the surface of the beaker, (a) After pouring cold water; (b) Recover; (c) After pouring hot water.



## 5.6 Weight Measurement Performance

Detecting the weight of an item directly or indirectly is significant for a robotic devices with a grasping function. The robot is required to obtain the weight information and apply the proper pressure to grab or lift it. This weight information is needed to be accurate so the robot will not apply too much stress to crash the item or too small force which is not enough to grab the item and could drop.

To demonstrate the ability of this sensor to measure the mechanical signal, such as strain or pressure, a commercial load cell was used as a reference. In this way, comparing this capacitive sensor with the commercial cell is a good method to demonstrate its accuracy. A platform and a hanger made of poly(methyl methacrylate) (PMMA) were prepared with the help of a milling machine. The PGS<sub>40</sub>/EG<sub>60</sub> sensor and the load cell (TE Connectivity [157]) were mounted in the rings on opposite sides of the hanger (Figure 5.8 (b)) to avoid dislocation of the two devices, and also to make sure the volunteer could apply equal force on them by setting them at the same height. After being installed a hook was placed on the bottom of the platform for further weight placements (Figure 5.8 (a)). A height indicator board was placed on the platform and 10 cm was marked on it. The setup used for PGS<sub>40</sub>/EG<sub>60</sub> sensor vs. load cell comparison system is shown in Figure 5.9.

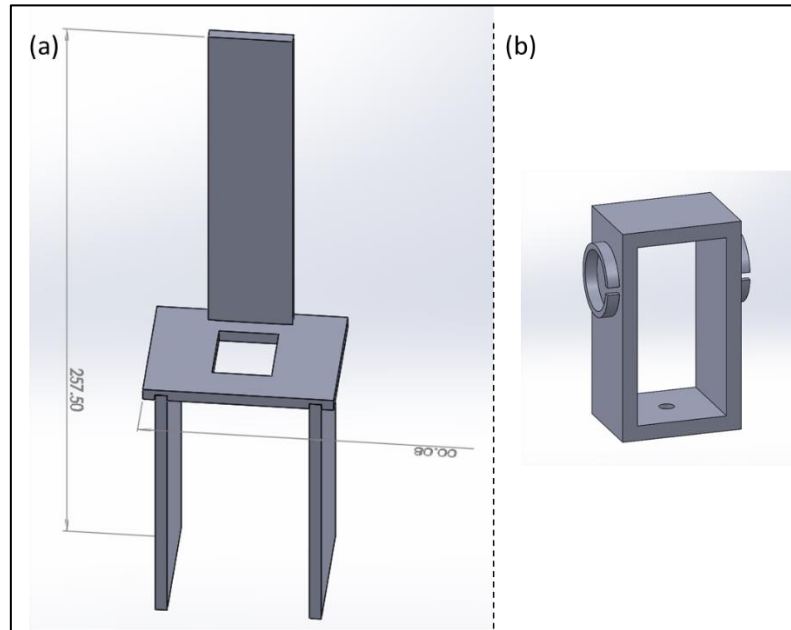


Figure 5.8 The 3D model of (a) a PTFE platform and (b) a PTFE hanger.

The volunteer clamped the weight with their fingertip (the position that can apply maximum force) of the thumb and forefinger and lifted it to the 10 cm mark of the platform. During the lifting period, the volunteer would lift the bare hanger, the hanger hung with a weight of 20g, 50g, 100g, and 200g in turn. After each lifting action finished, the hanger was placed on the platform. During the lifting process, the normal force ( $F$ ) of the index finger and thumb clamping is converted into an upward frictional force ( $f$ ) through the surface between the hanger and finger, which helped the volunteer lift the hanger (Equation 5.3). Due to the increase in weights, the normal force required to lift the

hanger increased. In this way, the normal force could be measured by the  $\Delta C/C_0$  of the capacitive sensor and compared with the signal retrieved by the commercial load cell:

$$f = \mu \times F \quad \text{Equation 5.3}$$

According to the result (Figure 5.10 (a)), the capacitive sensor and load cell presented increasing values with the increasing weight hung on the hanger. To demonstrate the accuracy of the capacitive sensor, the fitting curves of the  $\Delta C/C_0$  vs. weight, load cell value vs. weight and  $\Delta C/C_0$  value vs. load cell value were shown in Figure 5.10 (b). In Figure 5.10 (b), both the capacitive sensor and load cell showed great accuracy, or weight sensitivity, while measuring the weight of the hanger. The fitting curve of the load cell signal vs. weight was  $\frac{\Delta C}{C_0} = 0.00195 \cdot W + 0.179$ , which showed an  $R^2$  of 0.997 and demonstrates the good accuracy of the commercial load cell. For the capacitive sensor, the fitting curve of  $\Delta C/C_0$  vs. weight ( $W$ ) was  $\frac{\Delta C}{C_0} = 1.625 \cdot W + 94.938$ , which means the  $\Delta C/C_0$  value increased 1.625% with 1 gram of the weight increased. The  $R^2$  of 0.988 demonstrates the good fitting relationship between  $\Delta C/C_0$  vs. weight. In this way, the PGS<sub>40</sub>/EG<sub>60</sub> sensor had a weight measurement ability that is close to the commercial load cell and had a potential for wearable applications to measure the force feedback from prosthetic hands or other soft robotics grasping systems.

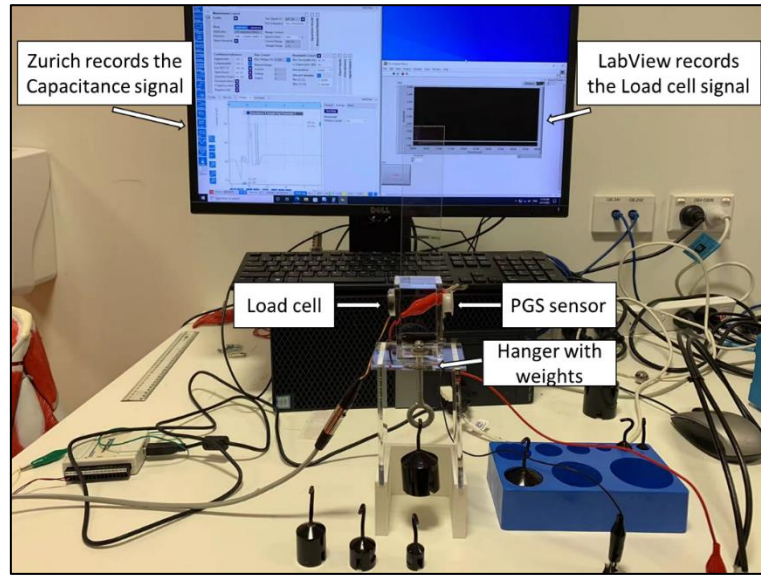


Figure 5.9 The PGS sensor vs. Load cell comparison system.

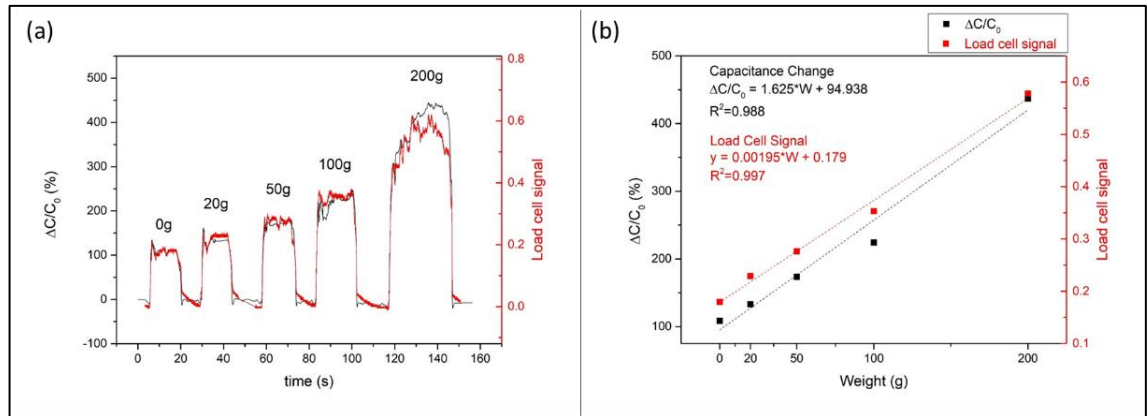


Figure 5.10 (a) The change of  $\Delta C/C_0$  and load cell signal with different weights; (b) The fitting of  $\Delta C/C_0$  and Load cell signal with weights.

## Chapter 6 Conclusions and Recommendations for Future Work

### 6.1 Conclusion

This thesis is focused on the synthesis of the PGS elastomeric foams, and their morphological, electrical, mechanical characterization, and electromechanical performance as capacitive sensors. The PGS was prepared by the polycondensation reaction of equal molar ratios of sebacic acid and glycerol, and a porous scaffold was created after salt was leached in deionized water. Furthermore, The PGS foam was cut into cylindrical samples and assembled between two silver tape electrodes in an Ecoflex casing.

Then, a systematic assessment of the PGS foam was performed to understand its properties. The PGS foam revealed an interconnected porous morphology consisting of large pores generated by the porogen and small voids in the walls of the large pores, its Young's modulus was  $8.7 \pm 0.3$  kPa which was soft than human skin and achieve the comfortable sensor objective of this study. The dielectric constant of PGS was 4.2 (at 300kHz), which was increased up to 7.7 when 60wt% EG solution was added. The overall performance of the PGS foam revealed interesting features to be used in wearable sensor applications.

The electromechanical behaviour of the assembled sensors was evaluated. For the PGS dry sensor, most of its electromechanical performances were good while measuring large deformations or large pressure, but showed some noise while measuring mild deformations ( $\epsilon \leq 5\%$ ). In this way, EG solution, as a high dielectric constant liquid ( $\epsilon_r = 37$ ), was mixed into PGS foam and a PGS/EG was assembled. The new sensor could present a clear signal and could clearly measure the strain and stress inputs with great accuracy, even for mild deformations. However, in its one-hour stability experiment, a small drift trend of around 3% was observed. To deal with this problem, several samples with small amounts of filler (40 wt%, 60 wt% and 80 wt% of EG) were prepared and the electromechanical performance was systematically characterized. The PGS<sub>40</sub>/EG<sub>60</sub> sensor was selected due to it has a higher  $\Delta C/C_0$  performance and good mild deformation detecting ability, showing the highest GF of 15 and sensitivity of  $0.27 \text{ kPa}^{-1}$ , which were 3.5-fold and 5.7-fold higher than those of the PGS dry sensor. In the response and recovery time measurement, the PGS<sub>40</sub>/EG<sub>60</sub> sensor has a fast response and recovery time of 209 ms and 230 ms, respectively. This performance was similar to most of the capacitive sensors reported in the literature.

In the electromechanical repeatability, the PGS<sub>40</sub>/EG<sub>60</sub> sensor could reach the same  $\Delta C/C_0$  values in the 15 load-unload quasi-static cycling experiments, and its  $\Delta C/C_0$  value drift of  $\Delta C/C_0$  value was negligible. In the static stability performance, the PGS<sub>40</sub>/EG<sub>60</sub> sensor had a relatively small percentage change of  $\Delta C/C_0$  drift of 1.89%. During the dynamic stability evaluation, a good performance was observed with a small change in the  $\Delta C/C_0$  maximum, from 230.7% to 235.4%.

The multifunctionality of the developed sensors was assessed by measuring different parameters

like proximity and temperature. The PGS<sub>40</sub>/EG<sub>60</sub> sensor could detect the metal pressure head of the universal testing machine from a far distance of around 40 mm in the proximity experiment. In the temperature measurement, the sensor could measure the external temperature from 25°C to 70°C with a relationship between the  $\Delta C/C_0$  value and the temperature of  $\frac{\Delta C}{C_0} = 0.62 \cdot T - 14.83$  and an  $R^2$  of 0.997, which enables it to mimic skin somatosensation and distinguish hot from cold surfaces, like the human hand.

Finally, six demonstrations for possible applications of the PGS<sub>40</sub>/EG<sub>60</sub> sensor were presented (Chapter 5). In finger bending monitoring, the sensor was attached to the index finger of the volunteer's left hand and it measured the angle of the index finger accurately with a relationship of “bending angle =  $7.72 \cdot (\Delta C/C_0) - 244.65$ ”. In the breathing measurement, the sensor could present the  $\Delta C/C_0$  value that varied with the fluctuation of the chest during breathing. It showed the lung volume of different breathing conditions, such as normal breathing, deep breath, and slowly inhalation and exhalation. The breath pattern and relative parameters can also be obtained by the sensor. In the hearting beating measurement, the sensor showed pulses with clear percussion peaks and rough tidal peaks. The information of two peaks could be used to know the AIr and SI of users and analyze their heart and blood vessel conditions. In proximity demonstration, the sensor could detect a finger approaching from around 30 mm, and the ups and downs or slow movements of the finger can be clearly monitored. In temperature measurement, the sensor detected the temperature of a beaker wall accurately, and the temperature can be obtained by combining its  $\Delta C/C_0$  value with the previous  $\Delta C/C_0$  value vs. the temperature equation. In the weight measurement, the ability of the sensor to measure the weight was compared with a commercial load cell. Both the sensor and load cell showed up an excellent performance in recognizing the force/weight hung on the hanger and the sensor presented a relationship between the  $\Delta C/C_0$  and the weight of  $\frac{\Delta C}{C_0} = 1.625 \cdot W + 94.938$ ,

After the addition of EG, the PGS/EG sensor achieved excellent sensitivity, rapid response time and recovery time, great repeatability, good static stability and long-term dynamic stability, and excellent proximity and temperature sensitivity behaviour. These excellent performances empower the sensor to monitor the finger bending action, breathing, heart beating, measure weight, sense temperature change and achieve proximity function.

## 6.2 Recommendations for Future Work

Despite the simple fabrication, excellent performances, and great demonstrations of porous flexible wearable PGS<sub>40</sub>/EG<sub>60</sub> capacitive sensor provided in this thesis, there are still some drawbacks in materials and engineering aspects that need to be improved to achieve an outstanding device.

The materials of the sensor are discussed first. From the external part of the sensor's structure to the internal part, the casing, the base material, the sensor's microstructure, and the filler or high dielectric material can be improved or further explored. The casing used is the Ecoflex elastomer,

which has a low Young modulus and could seal very well to avoid liquid leakage. However, the thickness of the Ecoflex casing in this project is around 1.5 mm, which is relatively thick causing some lag issues with the thermal properties of the sensor (Chapter 5.5). The heat insulation of the Ecoflex casing can be seen when it was used to measure the temperature change in Chapter 5.5. It took the PGS<sub>40</sub>/EG<sub>60</sub> sensor more than 500 s to decrease from around 18 °C to nearly 0 °C, 500 s to recover from 0 °C to 9.4 °C, and 300 s from 9.4 s to 60 °C (Figure 6.1). Due to the thin thickness of the wall of the beaker which is attributed to very fast heat conduction between the internal surface and external surface of the beaker, the external surface of the beaker could reach the same or close temperature as the inside hot or cold water in a short time. However, the time required for the sensor to reach its  $\Delta C/C_0$  value corresponding to the temperature is measured in hundreds of seconds. This could be attributed to the thick casing wall and its good heat insulation and the big volume occupied by the sensor. In the future, more types of casings are required to be studied, and new designs need to be explored to reduce the thermal insulation between the surface to be measured and the device.

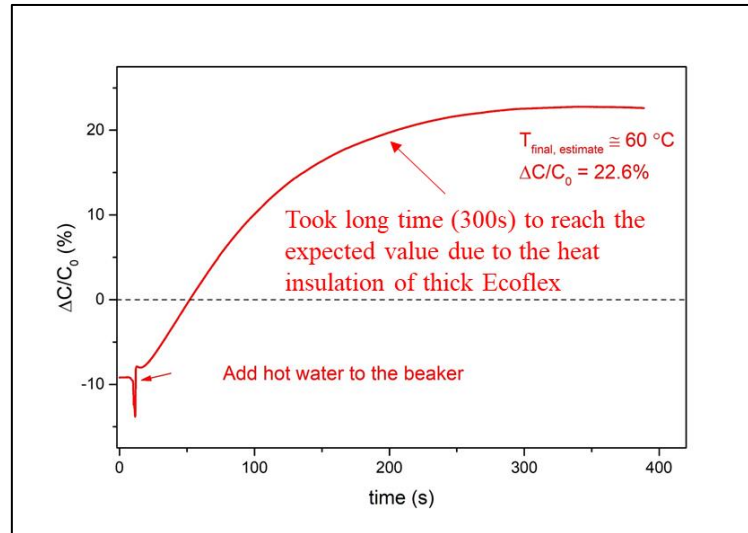


Figure 6.1 The material (casing) issue. Heat insulation of the thick Ecoflex case.

The PGS is an excellent dielectric material and can still be used as the base material. After the EG is added to the foam for a period, the PGS sample underwent a slight degradation as shown in Figure 6.2, (a) and (b). This degradation caused a slightly unstable capacitance signal (Figure 6.2 (c)). By preparing control experiments to study the origin of such behaviour, the effects of filler (EG) (Figure 6.3 (b)) and electrodes (silver tape) (Figure 6.3 (c)) were separately assessed (Figure 6.3), and this degradation could be attributed to the presence of silver tape that promoted oxidization of PGS over time. More studies and solutions to this issue are required in future developments.

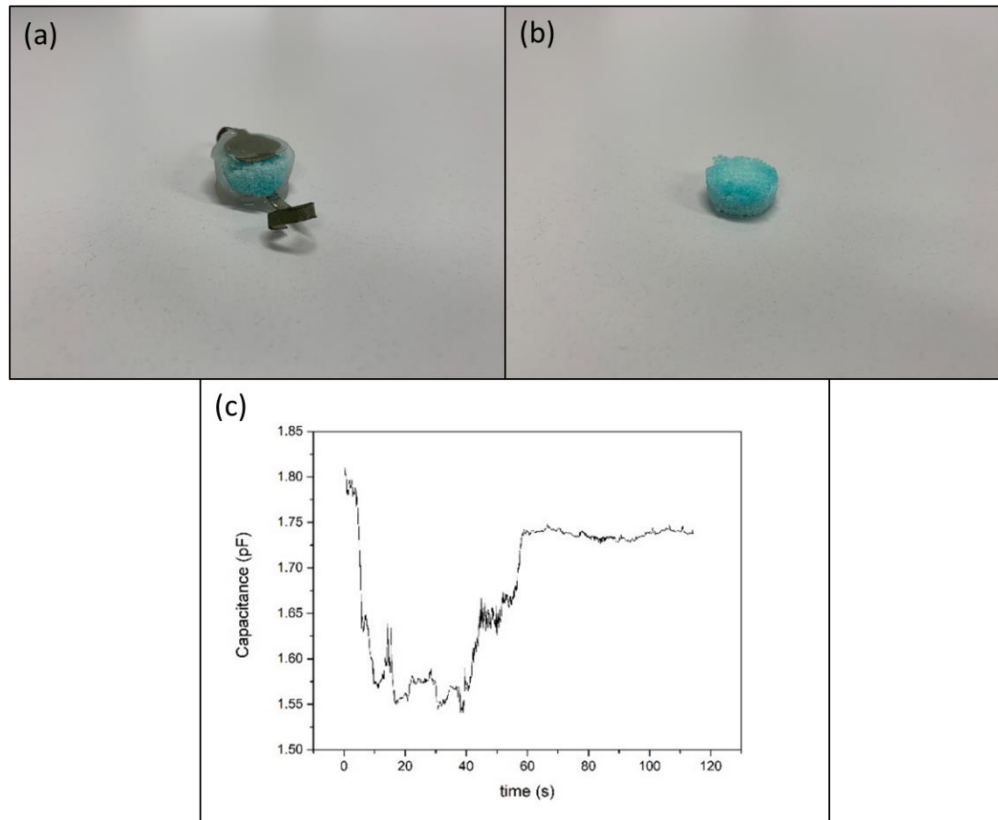


Figure 6.2 (a) The oxidization of PGS foam in sensor; (b) Oxidized PGS foam. (c) Unstable capacitance signal after slight oxidation occurs.

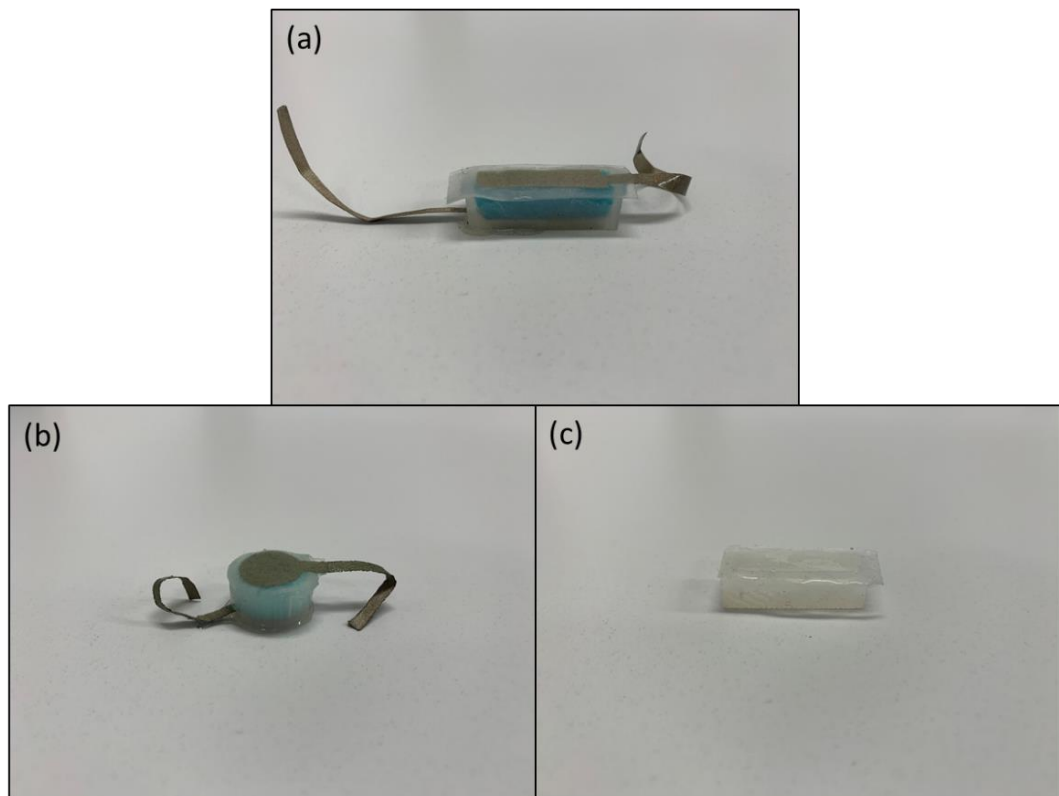


Figure 6.3 Oxidation controlled experiments of PGS sensor, (a) Oxidization happened. PGS sensor with full EG and silver tapes; (b) Oxidization happened. PGS dry sensor with silver tapes; (c) No oxidation. PGS sensor with full EG.

Besides the base material, the microstructure is needed to be studied. In Chapter 2.2.6.1, varieties of microstructures and processing methods are introduced, some microstructures such as hemisphere [78], pyramids-shape [76], and rose petal morphologies [108], and the methods, such as templating method, phase separation method and gas foaming could be explored for the preparation of the sensors to improve performance and achieve different applications. The most inside part can be the high dielectric filler filled in the base material. Many filler materials have been mentioned in Chapter 2.2.6.2, like the solid filler, carbon CNT [66, 69, 71, 89], carbon conductive paste (CCP) [67], graphene [115], etc, and ionic liquids. The background performance improvement mechanism of these fillers will be required to be studied more thoroughly, and these fillers could be potentially used to improve the performance of the PGS sensor in future studies.

The ultimate goal of engineering is to bring the materials to the market and to benefit people. The application of this PGS sensor is also needed to be considered. As mentioned in subchapter 4.3.3 and Chapter 5, the performances of this sensor showed up a multifunction that could measure the mechanical force or deformation, temperature and proximity. The sensor could measure these parameters accurately when measured individually, however, when both parameters are present, the sensor might lose its accuracy for one or both of the parameters. For example, while the temperature was measured in Figure 5.7, the addition of ice and hot water caused the proximity phenomenon, and when the deformation and proximity are measured separately, they also influence each other (in Figure 6.4 (a), the proximity experiment, the touch of the finger by mistake caused an obvious  $\Delta C/C_0$  increase; in Figure 6.4 (b), the weight measurement, the approach of the finger causing proximity).

This phenomenon could be seen as a function collaboration, e.g. screen with both the proximity and pressure sensing functions could unlock the screen when the finger is approaching and sense the touch of the finger. If an individual function is expected to be achieved without interaction, there are two possible solutions. One is to apply this sensor to independent performance applications and reduce the influence of other parameters. Or, the degree of each performance's influence is required to be studied and one whole signal of all parameters can be decoded into individual parameter signals. Both of the solutions need to be explored in future studies.

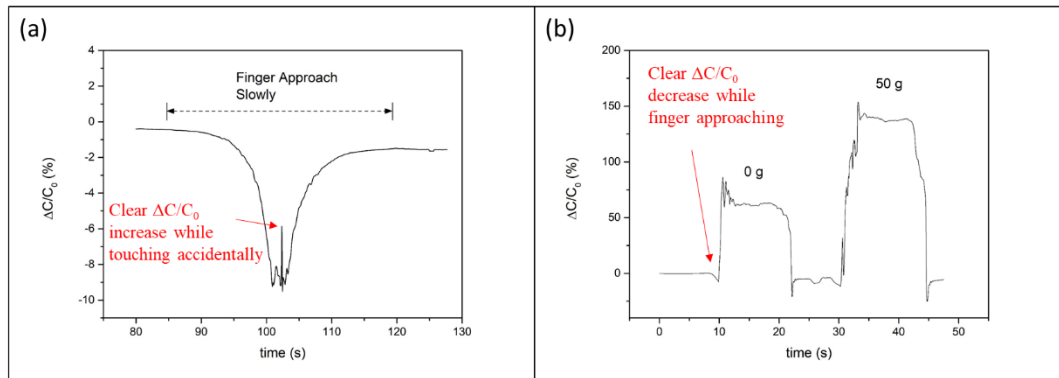


Figure 6.4 The interference between proximity and mechanical force, (a) A clear  $\Delta C/C_0$  increase while touching accidentally during proximity; (b) A clear  $\Delta C/C_0$  decrease while finger approaching during force experiment.



## References

1. Haaland, M. *Study shows Gen Z is more concerned about their health than Boomers*. 2022 [cited 2022 14/06]; Available from: <https://nypost.com/2020/07/07/gen-z-more-concerned-about-their-health-than-boomers-according-to-study/>.
2. Staff, H. *71% of Consumers Would Use Health Monitoring Devices If Data Was Clinically Accurate*. 2016 [cited 2022 14/06]; Available from: <https://hitconsultant.net/2016/02/03/31696/>.
3. Shirzadfar, H., et al., *Heart beat rate monitoring using optical sensors*. International Journal of Biosensors & Bioelectronics, 2018. **4**(2): p. 48-54.
4. Berger, A., *Oscillatory blood pressure monitoring devices*. Bmj, 2001. **323**(7318): p. 919.
5. Mirvis, D.M. and A.L. Goldberger, *Electrocardiography*. Heart Disease. A Textbook of Cardiovascular Medicine, 6th ed. Philadelphia: WB Saunders, 2001: p. 82-128.
6. Clinic, C. *Electromyograms*. 2016 12/06/2016 [cited 2022 14/02]; Available from: <https://my.clevelandclinic.org/health/articles/4825-electromyograms>.
7. Kumari, P., L. Mathew, and P. Syal, *Increasing trend of wearables and multimodal interface for human activity monitoring: A review*. Biosensors and Bioelectronics, 2017. **90**: p. 298-307.
8. Turki, A.F., et al. *An investigation of heartrate sensing accuracy by wrist-worn fitness tracking devices*. in 2019 41st annual international conference of the IEEE Engineering in Medicine and Biology Society (EMBC). 2019. IEEE.
9. Wang, L., et al., *Bio-Multifunctional Smart Wearable Sensors for Medical Devices*. Advanced Intelligent Systems, 2019. **1**(5): p. 1900040.
10. Gao, Y., et al., *Flexible hybrid sensors for health monitoring: materials and mechanisms to render wearability*. Advanced Materials, 2020. **32**(15): p. 1902133.
11. Vogt, L., et al., *Poly (glycerol sebacate) in biomedical applications—a review of the recent literature*. Advanced Healthcare Materials, 2021. **10**(9): p. 2002026.
12. Yan, Y., et al., *Processing, characterisation and electromechanical behaviour of elastomeric multiwall carbon nanotubes-poly (glycerol sebacate) nanocomposites for piezoresistive sensors applications*. Composites Science and Technology, 2017. **142**: p. 163-170.
13. Hayes, A. *Wearable Technology*. 2021 [cited 2022 24/06]; Available from: <https://www.investopedia.com/terms/w/wearable-technology.asp>.
14. BuiltIn. *What is Wearable Technology?* [cited 2022 24/06]; Available from: <https://builtin.com/wearables>.
15. Yasar, K. *Wearable technology*. 2022 May 2022 [cited 2022 24/06]; Available from: <https://www.techtarget.com/searchmobilecomputing/definition/wearable-technology>.
16. Hernandez, A. *IoT Wearables – Wearable Technology*. [cited 2022 30/06]; Available from: <http://www.infiniteinformationtechnology.com/iot-wearables-wearable-technology>.
17. Harito, C., et al., *The development of wearable polymer-based sensors: Perspectives*. Journal of The Electrochemical Society, 2020. **167**(3): p. 037566.
18. Burke, E., *Precision Heart Rate Training*. Human Kinetics Pub. Inc., 1998.
19. Jayathilaka, W.A.D.M., et al., *Significance of nanomaterials in wearables: a*

- review on wearable actuators and sensors. *Advanced Materials*, 2019. **31**(7): p. 1805921.
20. Pelletier, S.G., *Technology in academic medicine: Medicine takes a closer look at Google Glass*. 2015.
  21. Guze, P.A., *Using technology to meet the challenges of medical education*. Transactions of the American clinical and climatological association, 2015. **126**: p. 260.
  22. Lu, L., et al., *Wearable health devices in health care: narrative systematic review*. JMIR mHealth and uHealth, 2020. **8**(11): p. e18907.
  23. Jackson, M.M., et al. *FIDO-facilitating interactions for dogs with occupations: wearable dog-activated interfaces*. in *Proceedings of the 2013 international symposium on wearable computers*. 2013.
  24. Siddall, A.G., et al., *Validity of energy expenditure estimation methods during 10 days of military training*. Scandinavian journal of medicine & science in sports, 2019. **29**(9): p. 1313-1321.
  25. Rutherford, J.J., *Wearable technology*. IEEE Engineering in Medicine and Biology Magazine, 2010. **29**(3): p. 19-24.
  26. Pang, C., C. Lee, and K.Y. Suh, *Recent advances in flexible sensors for wearable and implantable devices*. Journal of Applied Polymer Science, 2013. **130**(3): p. 1429-1441.
  27. Bennett, H., *The Six Million Dollar Man* 1974: American Broadcasting Company.
  28. Hammock, M.L., et al., *25th anniversary article: the evolution of electronic skin (e-skin): a brief history, design considerations, and recent progress*. Advanced materials, 2013. **25**(42): p. 5997-6038.
  29. Kershner, I., *Star Wars Episode V: The Empire Strikes Back*. 1980: 20th Century Fox.
  30. Lumelsky, V., M. Shur, and S. Wagner, *Sensitive skin* IEEE Sensors J. 2001.
  31. Someya, T., et al., *Conformable, flexible, large-area networks of pressure and thermal sensors with organic transistor active matrixes*. Proceedings of the National Academy of Sciences, 2005. **102**(35): p. 12321-12325.
  32. Nie, B., et al., *Bio-inspired flexible electronics for smart E-skin*. Acta Biomaterialia, 2021.
  33. Lacour, S.P., et al., *Stretchable gold conductors on elastomeric substrates*. Applied physics letters, 2003. **82**(15): p. 2404-2406.
  34. Zhu, M., et al., *Highly shape adaptive fiber based electronic skin for sensitive joint motion monitoring and tactile sensing*. Nano Energy, 2020. **69**: p. 104429.
  35. Katerinopoulou, D., et al., *Large-area all-printed temperature sensing surfaces using novel composite thermistor materials*. Advanced Electronic Materials, 2019. **5**(2): p. 1800605.
  36. Viventi, J., et al., *Flexible, foldable, actively multiplexed, high-density electrode array for mapping brain activity in vivo*. Nature neuroscience, 2011. **14**(12): p. 1599-1605.
  37. Kim, D.-H., et al., *Materials for multifunctional balloon catheters with capabilities in cardiac electrophysiological mapping and ablation therapy*. Nature materials, 2011. **10**(4): p. 316-323.
  38. Tee, B.C., et al., *An electrically and mechanically self-healing composite with pressure-and flexion-sensitive properties for electronic skin applications*. Nature nanotechnology, 2012. **7**(12): p. 825-832.
  39. Fan, F.-R., et al., *Transparent triboelectric nanogenerators and self-powered pressure sensors based on micropatterned plastic films*. Nano letters, 2012. **12**(6):

- p. 3109-3114.
40. Yamada, T., et al., *A stretchable carbon nanotube strain sensor for human-motion detection*. Nature nanotechnology, 2011. **6**(5): p. 296-301.
  41. Mattmann, C., F. Clemens, and G. Tröster, *Sensor for measuring strain in textile*. Sensors, 2008. **8**(6): p. 3719-3732.
  42. Omer, R.M.D. and N.K. Al-Salihi. *HealthMate: Smart wearable system for health monitoring (SWSHM)*. in *2017 IEEE 14th International Conference on Networking, Sensing and Control (ICNSC)*. 2017. IEEE.
  43. Sharma, S., et al., *Wearable capacitive pressure sensor based on MXene composite nanofibrous scaffolds for reliable human physiological signal acquisition*. ACS applied materials & interfaces, 2020. **12**(19): p. 22212-22224.
  44. Kim, J., et al., *Soft wearable pressure sensors for beat-to-beat blood pressure monitoring*. Advanced healthcare materials, 2019. **8**(13): p. 1900109.
  45. Jung, Y., et al., *A highly sensitive and flexible capacitive pressure sensor based on a porous three-dimensional PDMS/microsphere composite*. Polymers, 2020. **12**(6): p. 1412.
  46. Wang, J., et al., *Capacitive pressure sensor with wide-range, bendable, and high sensitivity based on the bionic komochi konbu structure and Cu/Ni nanofiber network*. ACS applied materials & interfaces, 2019. **11**(12): p. 11928-11935.
  47. Chen, S., B. Zhuo, and X. Guo, *Large area one-step facile processing of microstructured elastomeric dielectric film for high sensitivity and durable sensing over wide pressure range*. ACS applied materials & interfaces, 2016. **8**(31): p. 20364-20370.
  48. Yang, J., et al., *Ionic liquid-activated wearable electronics*. Materials Today Physics, 2019. **8**: p. 78-85.
  49. Ashworth, T., *Impedance Characterization of Wearable Capacitive Sensors*, in *Zurich Instruments*. 2021.
  50. Amjadi, M., et al., *Stretchable, skin-mountable, and wearable strain sensors and their potential applications: a review*. Advanced Functional Materials, 2016. **26**(11): p. 1678-1698.
  51. Li, Y., W. Chen, and L. Lu, *Wearable and biodegradable sensors for human health monitoring*. ACS Applied Bio Materials, 2020. **4**(1): p. 122-139.
  52. Fiorillo, A., C. Critello, and S. Pullano, *Theory, technology and applications of piezoresistive sensors: A review*. Sensors and Actuators A: Physical, 2018. **281**: p. 156-175.
  53. Georgopoulou, A. and F. Clemens, *Piezoresistive elastomer-based composite strain sensors and their applications*. ACS Applied Electronic Materials, 2020. **2**(7): p. 1826-1842.
  54. Park, J., et al., *Giant tunneling piezoresistance of composite elastomers with interlocked microdome arrays for ultrasensitive and multimodal electronic skins*. ACS nano, 2014. **8**(5): p. 4689-4697.
  55. Jian, M., et al., *Flexible and highly sensitive pressure sensors based on bionic hierarchical structures*. Advanced Functional Materials, 2017. **27**(9): p. 1606066.
  56. Safari, A. and E.K. Akdogan, *Piezoelectric and acoustic materials for transducer applications*. 2008: Springer Science & Business Media.
  57. Mason, W.P., *Piezoelectricity, its history and applications*. The journal of the Acoustical Society of America, 1981. **70**(6): p. 1561-1566.
  58. Heywang, W., K. Lubitz, and W. Wersing, *Piezoelectricity: evolution and future of a technology*. Vol. 114. 2008: Springer Science & Business Media.
  59. Dagdeviren, C., et al., *Conformable amplified lead zirconate titanate sensors with*

- enhanced piezoelectric response for cutaneous pressure monitoring. *Nature communications*, 2014. **5**(1): p. 1-10.
60. Zhong, Q., et al., *Paper-Based Active Tactile Sensor Array*. *Advanced Materials*, 2015. **27**(44): p. 7130-7136.
  61. Abacus, A. *Capacitive vs piezoresistive vs piezoelectric pressure sensors*. [cited 2022 23/05]; Available from: <https://www.avnet.com/wps/portal/abacus/solutions/technologies/sensors/pressure-sensors/core-technologies/capacitive-vs-piezoresistive-vs-piezoelectric/>.
  62. Harrington, R.F., *Introduction to electromagnetic engineering*. 2003: Courier Corporation.
  63. Zheng, Y.N., et al., *A Wearable Capacitive Sensor Based on Ring/Disk-Shaped Electrode and Porous Dielectric for Noncontact Healthcare Monitoring*. *Global Challenges*, 2020. **4**(5): p. 1900079.
  64. Li, W., et al., *High-performance paper-based capacitive flexible pressure sensor and its application in human-related measurement*. *Nanoscale research letters*, 2019. **14**(1): p. 1-7.
  65. Xie, L., et al., *Low-cost and highly sensitive wearable sensor based on napkin for health monitoring*. *Sensors*, 2019. **19**(15): p. 3427.
  66. Guo, Z., et al., *Printed and flexible capacitive pressure sensor with carbon nanotubes based composite dielectric layer*. *Micromachines*, 2019. **10**(11): p. 715.
  67. Wei, P., et al., *Flexible capacitive pressure sensor with sensitivity and linear measuring range enhanced based on porous composite of carbon conductive paste and polydimethylsiloxane*. *Nanotechnology*, 2019. **30**(45): p. 455501.
  68. Sarwar, M.S., et al., *Bend, stretch, and touch: Locating a finger on an actively deformed transparent sensor array*. *Science advances*, 2017. **3**(3): p. e1602200.
  69. Yoon, S.G., B.J. Park, and S.T. Chang, *Highly sensitive piezocapacitive sensor for detecting static and dynamic pressure using ion-gel thin films and conductive elastomeric composites*. *ACS applied materials & interfaces*, 2017. **9**(41): p. 36206-36219.
  70. Kim, S.-R., J.-H. Kim, and J.-W. Park, *Wearable and transparent capacitive strain sensor with high sensitivity based on patterned Ag nanowire networks*. *ACS applied materials & interfaces*, 2017. **9**(31): p. 26407-26416.
  71. Cui, J., et al., *Flexible pressure sensor with Ag wrinkled electrodes based on PDMS substrate*. *Sensors*, 2016. **16**(12): p. 2131.
  72. Thouti, E., et al., *Tunable flexible capacitive pressure sensors using arrangement of polydimethylsiloxane micro-pyramids for bio-signal monitoring*. *Sensors and Actuators A: Physical*, 2020. **314**: p. 112251.
  73. Zhou, Q., et al., *Tilted magnetic micropillars enabled dual-mode sensor for tactile/touchless perceptions*. *Nano Energy*, 2020. **78**: p. 105382.
  74. Li, S., et al., *Capacitive pressure sensor inlaid a porous dielectric layer of superelastic polydimethylsiloxane in conductive fabrics for detection of human motions*. *Sensors and Actuators A: Physical*, 2020. **312**: p. 112106.
  75. Kim, Y., S. Jang, and J.H. Oh, *Fabrication of highly sensitive capacitive pressure sensors with porous PDMS dielectric layer via microwave treatment*. *Microelectronic Engineering*, 2019. **215**: p. 111002.
  76. Luo, S., et al., *Tunable-sensitivity flexible pressure sensor based on graphene transparent electrode*. *solid-state electronics*, 2018. **145**: p. 29-33.
  77. Lin, M.-F., et al., *Core-shell nanofiber mats for tactile pressure sensor and nanogenerator applications*. *Nano Energy*, 2018. **44**: p. 248-255.
  78. Sharma, V.V., et al., *3D Multiscale Gradient Pores Impregnated with Ag*

- Nanowires for Simultaneous Pressure and Bending Detection with Enhanced Linear Sensitivity*. Advanced Materials Technologies, 2020. **5**(4): p. 1901041.
79. Wang, X., et al., *Development of a flexible and stretchable tactile sensor array with two different structures for robotic hand application*. RSC advances, 2017. **7**(76): p. 48461-48465.
  80. Nguyen, Q., et al., *An integrated flexible capacitance sensor for monitoring microvalve actuation*. Sensors and Actuators B: Chemical, 2019. **282**: p. 171-176.
  81. Tavakoli, M., et al., *Autonomous Selection of Closing Posture of a Robotic Hand Through Embodied Soft Matter Capacitive Sensors*. Ieee Sensors Journal, 2017. **17**(17): p. 5669-5677.
  82. Rocha, R.P., et al., *Fabrication and characterization of bending and pressure sensors for a soft prosthetic hand*. JOURNAL OF MICROMECHANICS AND MICROENGINEERING, 2018. **28**(3).
  83. Chhetry, A., et al., *Ultrasensitive interfacial capacitive pressure sensor based on a randomly distributed microstructured iontronic film for wearable applications*. ACS applied materials & interfaces, 2018. **11**(3): p. 3438-3449.
  84. Cho, S.H., et al., *Micropatterned pyramidal ionic gels for sensing broad-range pressures with high sensitivity*. ACS applied materials & interfaces, 2017. **9**(11): p. 10128-10135.
  85. Zhao, S., et al., *3D dielectric layer enabled highly sensitive capacitive pressure sensors for wearable electronics*. ACS applied materials & interfaces, 2020. **12**(28): p. 32023-32030.
  86. Yao, H.B., et al., *A flexible and highly pressure-sensitive graphene-polyurethane sponge based on fractured microstructure design*. Advanced Materials, 2013. **25**(46): p. 6692-6698.
  87. Jing, X., et al., *Highly transparent, stretchable, and rapid self-healing polyvinyl alcohol/cellulose nanofibril hydrogel sensors for sensitive pressure sensing and human motion detection*. Sensors and Actuators B: Chemical, 2019. **295**: p. 159-167.
  88. Lei, Z., et al., *A bioinspired mineral hydrogel as a self-healable, mechanically adaptable ionic skin for highly sensitive pressure sensing*. Advanced Materials, 2017. **29**(22): p. 1700321.
  89. Choi, J., et al., *Synergetic effect of porous elastomer and percolation of carbon nanotube filler toward high performance capacitive pressure sensors*. ACS applied materials & interfaces, 2019. **12**(1): p. 1698-1706.
  90. Yao, S., et al., *A novel finger kinematic tracking method based on skin-like wearable strain sensors*. IEEE Sensors Journal, 2018. **18**(7): p. 3010-3015.
  91. Zhang, Z., et al., *Highly transparent, self-healable, and adhesive organogels for bio-inspired intelligent ionic skins*. ACS applied materials & interfaces, 2020. **12**(13): p. 15657-15666.
  92. Kou, H., et al., *Wireless flexible pressure sensor based on micro-patterned Graphene/PDMS composite*. Sensors and Actuators A: Physical, 2018. **277**: p. 150-156.
  93. Pang, Y., et al., *Flexible, highly sensitive, and wearable pressure and strain sensors with graphene porous network structure*. ACS applied materials & interfaces, 2016. **8**(40): p. 26458-26462.
  94. Xu, F., et al., *Recent developments for flexible pressure sensors: A review*. Micromachines, 2018. **9**(11): p. 580.
  95. Xu, M., et al., *Facile fabrication of a flexible linbo3 piezoelectric sensor through hot pressing for biomechanical monitoring*. ACS applied materials & interfaces,

2017. **9**(40): p. 34687-34695.
96. Callister, W.D. and D.G. Rethwisch, *Materials science and engineering: an introduction*. Vol. 9. 2018: Wiley New York.
  97. R. Chen, N.M. *Dielectric Polarization*. 2021 [cited 2022 27/04]; Available from: [https://eng.libretexts.org/Bookshelves/Materials\\_Science/Supplemental\\_Modules\\_\(Materials\\_Science\)/Optical\\_Properties/Dielectric\\_Polarization](https://eng.libretexts.org/Bookshelves/Materials_Science/Supplemental_Modules_(Materials_Science)/Optical_Properties/Dielectric_Polarization).
  98. Britannica. *dielectric loss*. 2016 [cited 2022 07/07]; Available from: <https://www.britannica.com/science/dielectric-loss>.
  99. Musikant, S., *Encyclopedia of Physical Science and Technology*. 2003.
  100. Wu, G., et al., *Design of carbon sphere/magnetic quantum dots with tunable phase compositions and boost dielectric loss behavior*. Chemical Engineering Journal, 2018. **333**: p. 519-528.
  101. Wang, Y., et al., *Reduced graphene oxide (RGO)/Mn<sub>3</sub>O<sub>4</sub> nanocomposites for dielectric loss properties and electromagnetic interference shielding effectiveness at high frequency*. Ceramics International, 2016. **42**(1): p. 936-942.
  102. Wang, H., et al., *Permittivity, loss factor and Cole-Cole model of acrylic materials for dielectric elastomers*. Results in Physics, 2021. **29**: p. 104781.
  103. Pérez, A.T. and M. Hadfield, *Low-cost oil quality sensor based on changes in complex permittivity*. Sensors, 2011. **11**(11): p. 10675-10690.
  104. Sperling, L.H., *Introduction to physical polymer science*. 2005: John Wiley & Sons.
  105. Maxwells-Equations.com. *Displacement Current Density - The Partial Derivative of D*. 2012 [cited 2022 28/04]; Available from: <https://www.maxwells-equations.com/math/partial-electric-flux.php>.
  106. Salerno, A., et al., *Design of porous polymeric scaffolds by gas foaming of heterogeneous blends*. Journal of Materials Science-Materials in Medicine, 2009. **20**(10): p. 2043-2051.
  107. Chhetry, A., H. Yoon, and J.Y. Park, *A flexible and highly sensitive capacitive pressure sensor based on conductive fibers with a microporous dielectric for wearable electronics*. Journal of Materials Chemistry C, 2017. **5**(38): p. 10068-10076.
  108. Mahata, C., et al., *Biomimetic-inspired micro-nano hierarchical structures for capacitive pressure sensor applications*. Measurement, 2020. **151**: p. 107095.
  109. Zhao, L., et al., *Biomimetic-inspired highly sensitive flexible capacitive pressure sensor with high-aspect-ratio microstructures*. Current Applied Physics, 2021. **31**: p. 29-37.
  110. Danesh, E., S.R. Ghaffarian, and P. Molla-Abbasi, *Non-solvent induced phase separation as a method for making high-performance chemiresistors based on conductive polymer nanocomposites*. Sensors and Actuators B-Chemical, 2011. **155**(2): p. 562-567.
  111. Ishigami, T., et al., *Solidification Behavior of Polymer Solution during Membrane Preparation by Thermally Induced Phase Separation*. Membranes, 2014. **4**(1): p. 113-122.
  112. Freemantle, M., *An introduction to ionic liquids*. 2010: Royal Society of chemistry.
  113. Wang, Z., et al., *Flexible and washable poly (ionic liquid) nanofibrous membrane with moisture proof pressure sensing for real-life wearable electronics*. ACS applied materials & interfaces, 2019. **11**(30): p. 27200-27209.
  114. Huang, X., et al., *High-k polymer nanocomposites with 1D filler for dielectric and energy storage applications*. Progress in Materials Science, 2019. **100**: p. 187-



- 225.
115. Liu, Y.-Q., et al., *Directly drawing high-performance capacitive sensors on copying tissues*. *Nanoscale*, 2018. **10**(36): p. 17002-17006.
  116. Walker, G., *A review of technologies for sensing contact location on the surface of a display*. *Journal of the Society for Information Display*, 2012. **20**(8): p. 413-440.
  117. Yao, S. and Y. Zhu, *Wearable multifunctional sensors using printed stretchable conductors made of silver nanowires*. *Nanoscale*, 2014. **6**(4): p. 2345-2352.
  118. Cheng, Y., et al., *Stretchable electronic skin based on silver nanowire composite fiber electrodes for sensing pressure, proximity, and multidirectional strain*. *Nanoscale*, 2017. **9**(11): p. 3834-3842.
  119. Chaurasia, S., R. Singh, and S. Chandra, *Thermal stability, complexing behavior, and ionic transport of polymeric gel membranes based on polymer PVdF-HFP and ionic liquid, [BMIM][BF<sub>4</sub>]*. *The Journal of Physical Chemistry B*, 2013. **117**(3): p. 897-906.
  120. Wang, Z., *Polydimethylsiloxane mechanical properties measured by macroscopic compression and nanoindentation techniques*. 2011.
  121. Yoo, J.Y., et al., *Industrial grade, bending-insensitive, transparent nanoforce touch sensor via enhanced percolation effect in a hierarchical nanocomposite film*. *Advanced Functional Materials*, 2018. **28**(42): p. 1804721.
  122. DOW. SYLGARD™ 184 Silicone Elastomer Kit. [cited 2022 22/05]; Available from: <https://www.dow.com/en-us/pdp.sylgard-184-silicone-elastomer-kit.01064291z.html#overview>.
  123. Liu, F., et al., *An omni-healable and highly sensitive capacitive pressure sensor with microarray structure*. *Chemistry—A European Journal*, 2018. **24**(63): p. 16823-16832.
  124. Amjadi, M., et al., *Highly stretchable and sensitive strain sensor based on silver nanowire–elastomer nanocomposite*. *ACS nano*, 2014. **8**(5): p. 5154-5163.
  125. Khalid, M.A.U., et al., *A highly sensitive biodegradable pressure sensor based on nanofibrous dielectric*. *Sensors and Actuators A: Physical*, 2019. **294**: p. 140-147.
  126. Wang, Y., et al., *A tough biodegradable elastomer*. *Nature Biotechnology*, 2002. **20**(6): p. 602-606.
  127. Boutry, C.M., et al., *A sensitive and biodegradable pressure sensor array for cardiovascular monitoring*. *Advanced Materials*, 2015. **27**(43): p. 6954-6961.
  128. DOW. SYLGARD™ 184 Silicone Elastomer Kit. [cited 2022 04/21]; Available from: <https://www.dow.com/en-us/pdp.sylgard-184-silicone-elastomer-kit.01064291z.html?productCatalogFlag=1#overview>.
  129. Kim, M., B.-U. Moon, and C.H. Hidrovo, *Enhancement of the thermo-mechanical properties of PDMS molds for the hot embossing of PMMA microfluidic devices*. *Journal of Micromechanics and Microengineering*, 2013. **23**(9): p. 095024.
  130. Cutroneo, M., et al., *Pulsed Laser Deposition and Laser-Induced Backward Transfer to Modify Polydimethylsiloxane*. *Coatings*, 2021. **11**(12): p. 1521.
  131. Fohlerova, Z., et al., *SiO<sub>2</sub>-Decorated Parylene C Micropillars Designed to Probe Cellular Force*. *Advanced Materials Interfaces*, 2021. **8**(6): p. 2001897.
  132. Annaidh, A.N., et al., *Characterization of the anisotropic mechanical properties of excised human skin*. *Journal of the mechanical behavior of biomedical materials*, 2012. **5**(1): p. 139-148.
  133. Gallagher, A., A. Ní Annaidh, and K. Bruyère. *Dynamic tensile properties of human skin*. in *IRCOBI Conference 2012, 12-14 September 2012, Dublin (Ireland)*. 2012. International Research Council on the Biomechanics of Injury.

134. Ottenio, M., et al., *Strain rate and anisotropy effects on the tensile failure characteristics of human skin*. Journal of the mechanical behavior of biomedical materials, 2015. **41**: p. 241-250.
135. Sencadas, V., et al., *Low-hysteresis and ultrasensitive microcellular structures for wearable electronic applications*. ACS Applied Materials & Interfaces, 2020. **13**(1): p. 1632-1643.
136. Du, P., X. Lin, and X. Zhang. *Dielectric constants of PDMS nanocomposites using conducting polymer nanowires*. in *2011 16th International Solid-State Sensors, Actuators and Microsystems Conference*. 2011. IEEE.
137. Brandrup, J., et al., *Polymer handbook*. Vol. 89. 1999: Wiley New York.
138. Shivashankar, H., et al., *Investigation on dielectric properties of PDMS based nanocomposites*. Physica B: Condensed Matter, 2021. **602**: p. 412357.
139. MIT. *Material: PDMS (polydimethylsiloxane)*. [cited 2022 25/04]; Available from: <https://www.mit.edu/~6.777/matprops/pdms.htm>.
140. Singh, M., et al., *Nanoscale Strategies to Enhance the Energy Storage Capacity of Polymeric Dielectric Capacitors: Review of Recent Advances*. Polymer Reviews, 2021: p. 1-50.
141. Wang, Y., Y.M. Kim, and R. Langer, *In vivo degradation characteristics of poly (glycerol sebacate)*. Journal of Biomedical Materials Research Part A: An Official Journal of The Society for Biomaterials, The Japanese Society for Biomaterials, and The Australian Society for Biomaterials and the Korean Society for Biomaterials, 2003. **66**(1): p. 192-197.
142. Sencadas, V., C. Tawk, and G. Alici, *Environmentally friendly and biodegradable ultrasensitive piezoresistive sensors for wearable electronics applications*. ACS Applied Materials & Interfaces, 2020. **12**(7): p. 8761-8772.
143. Sencadas, V., et al., *Low-Hysteresis and Ultrasensitive Microcellular Structures for Wearable Electronic Applications*. ACS Applied Materials & Interfaces, 2020.
144. Yoon, J., J. Lee, and J. Hur, *Stretchable supercapacitors based on carbon nanotubes-deposited rubber polymer nanofibers electrodes with high tolerance against strain*. Nanomaterials, 2018. **8**(7): p. 541.
145. Li, P., et al., *Reduced leakage current, enhanced ferroelectric and dielectric properties of (La, Fe)-codoped Bi<sub>0.5</sub>Na<sub>0.5</sub>TiO<sub>3</sub>-based thin films*. Ceramics International, 2015. **41**: p. S344-S348.
146. Sencadas, V., et al., *Low-Hysteresis and Ultrasensitive Microcellular Structures for Wearable Electronic Applications*. ACS Applied Materials & Interfaces, 2021. **13**(1): p. 1632-1643.
147. Sengwa, R.J., K. Kaur, and R. Chaudhary, *Dielectric properties of low molecular weight poly(ethylene glycol)s*. Polymer International, 2000. **49**(6): p. 599-608.
148. Yu, Y., et al., *Plasticizing effect of poly (ethylene glycol) s with different molecular weights in poly (lactic acid)/starch blends*. Journal of Applied Polymer Science, 2015. **132**(16).
149. Pivsa-Art, W., et al., *The effect of poly (ethylene glycol) as plasticizer in blends of poly (lactic acid) and poly (butylene succinate)*. Journal of Applied Polymer Science, 2016. **133**(8).
150. Zhou, T., et al., *Poly (ethylene glycol) plasticized poly (vinyl alcohol)/poly (acrylamide-co-diallyldimethylammonium chloride) as alkaline anion-exchange membrane for potential fuel cell applications*. Synthetic metals, 2013. **167**: p. 43-50.
151. Bellisle, F., *10 - The value of studying laboratory meals*, in *Context*, H.L. Meiselman, Editor. 2019, Woodhead Publishing. p. 209-225.



152. Rowden, A. *What is a normal respiratory rate based on your age?* 2021 21/12/2021 [cited 2022 05/05]; Available from: <https://www.medicalnewstoday.com/articles/324409>.
153. Kohara, K., et al., *Radial augmentation index: A useful and easily obtainable parameter for vascular aging*. American Journal of Hypertension, 2005. **18**(1): p. 11S-14S.
154. Nichols, W.W., *Clinical measurement of arterial stiffness obtained from noninvasive pressure waveforms*. American Journal of Hypertension, 2005. **18**(S1): p. 3S-10S.
155. Kohara, K., et al., *Radial augmentation index: A useful and easily obtainable parameter for vascular aging*. American Journal of Hypertension, 2005. **18**(S1): p. 11S-14S.
156. Uejima, T., et al., *Age-specific reference values for carotid arterial stiffness estimated by ultrasonic wall tracking*. Journal of human hypertension, 2020. **34**(3): p. 214-222.
157. Element14. *FX29K0-100A-0010-L*. 2022 [cited 2022 17/02]; Available from: <https://au.element14.com/sensor-solutions-te-connectivity/fx29k0-100a-0010-l/load-cell-sensor-10lb-5-5v/dp/3285865>.
158. Garland. *Coaxial Cable, RG58/U, 20 AWG 50 Ohm, 500m*. [cited 2022 09/05]; Available from: <https://www.garlandcables.com.au/product/coaxial-cable-rg58-u-20-awg-50-ohm-500m/>.
159. Mueller. *Insulated Miniature Kelvin Clip*. [cited 2022 09/05]; Available from: <https://www.muellerelectric.com/products/BU-75K>.
160. SIHIMADZU. *EZ Test*. 2021 [cited 2022 22/05]; Available from: <https://www.shimadzu.com/an/products/materials-testing/uni-ttm/ez-test/index.html>.

# Appendices

## Appendix A

### A.1 Preparation Related Devices

#### PHI Manual Hydraulic Compression Presses – P210C

This presser was used to compress the PGS in the mould into a uniform shape with a flat surface to reduce the uneven thickness and porosity of the PGS foam.



Figure A.1 PHI Manual Hydraulic Compression Presses – P210C

#### FAITHFUL Vacuum Drying Oven

The PGS pre-polymer was cured through condensation polymerization, which was performed by FAITHFUL Vacuum Drying Oven.



Figure A.2 FAITHFUL Vacuum Drying Oven.

#### Corning Hot Plate Stirrer Model PC 351

To remove the NaCl porogen from PGS foam, the PGS foam was put into deionized water and magnetically stirred using the Corning Hot Plate Stirrer Model PC 351 (Figure A.3) and its magnetic stirrer.



Figure A.3 Corning Hot Plate Stirrer Model PC 351.

#### Fiocchetti Scientific Refrigerators SUPERPOLO 130

To remove the liquid deionized water generated in the previous step without the hole collaborating and interacting with each other, the freeze-dring method was applied. The freezing step was conducted with Fiocchetti Scientific Refrigerators SUPERPOLO 130. The PGS sample was placed

on a flat surface of the fridge for 2 hours to allow liquid water to condense.

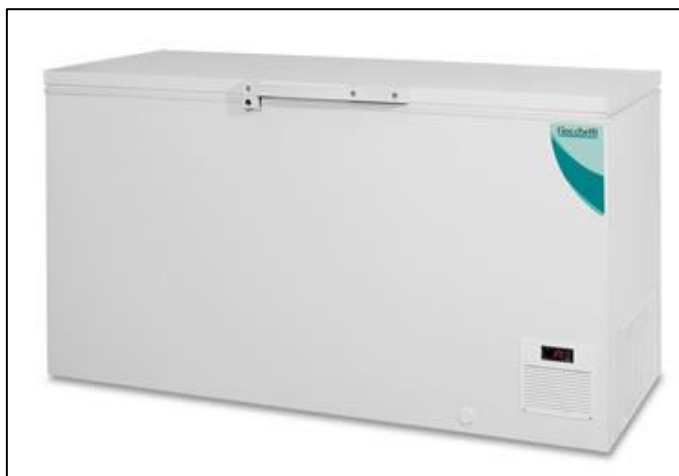


Figure A.4 Fiocchetti Scientific Refrigerators SUPERPOLO 130.

#### TOPTION Small Freeze Dryer TOPT-10D

The drying process was achieved using TOPTION Small Freeze Dryer TOPT-10D. The PGS sample was placed on the platform, and the ice in PGS foam was directly sublimated by the dryer under -42 °C conditions for 24 hours.



Figure A.5 TOPTION Small Freeze Dryer TOPT-10D.

#### Flashforge Inventor Dual Filament 3D printer TL4230

The 3D models were built using the Solidworks software, and then the 3D files were exported as an STL to be able to read in the FlashPrint Software, the software this printer used.



Figure A.6 Flashforge Inventor Dual Filament 3D printer.

#### Laser Engraver

A laser Engraver platform (Versa Laser Device, VLS2.50, Universal Laser System, Ltd.) was applied to laser cut the silver tape for the capacitive sensor. The VLS2.50 platform owns a CO<sub>2</sub> plotter with a maximum Laser Power of 25 Watt, a maximum resolution of 1000 pixels per inch (PPI) and a scan length from 0.25 to 25 mm/s, which could make it have enough power to engrave material with relatively high hardness and laser cut the material accurately and rapidly.

The device is accompanied by a default 2.0 inch lens. AutoCAD (Autodesk Inc., USA) was utilized to draw the desired pattern.



Figure A.7 Versa Laser Device.

## A.2 Performance Measurement Devices

### JCM-6000 Versatile Benchtop Scanning electron microscopy



Figure A.8 JCM-6000 Versatile Benchtop SEM

### Zurich Instruments Impedance Analyzer - Electrical signal measuring device

LCR meter from Zurich Instrument MFIA Impedance Analyzer was used to measure the capacitance value of the sensors (Figure A.9), and its operation software LabOne was used to input the parameters and output the measured data (Figure A.10). The calibration of the capacitive signal was required before the measurement by taking the capacitance reading at an open and short circuit load to compensate for residual capacitance.

The LCR meter was connected with the computer with a Garland Coaxial Cable (Garland, RG58/U, 50 Ohm, AWM Style [158]) and a Mueller insulate miniature Kelvin clip (Mueller, BU-75K [159]), shown in Figure A.11.



Figure A.9 LCR meter from Zurich Instruments MFLI Impedance Analyzer.



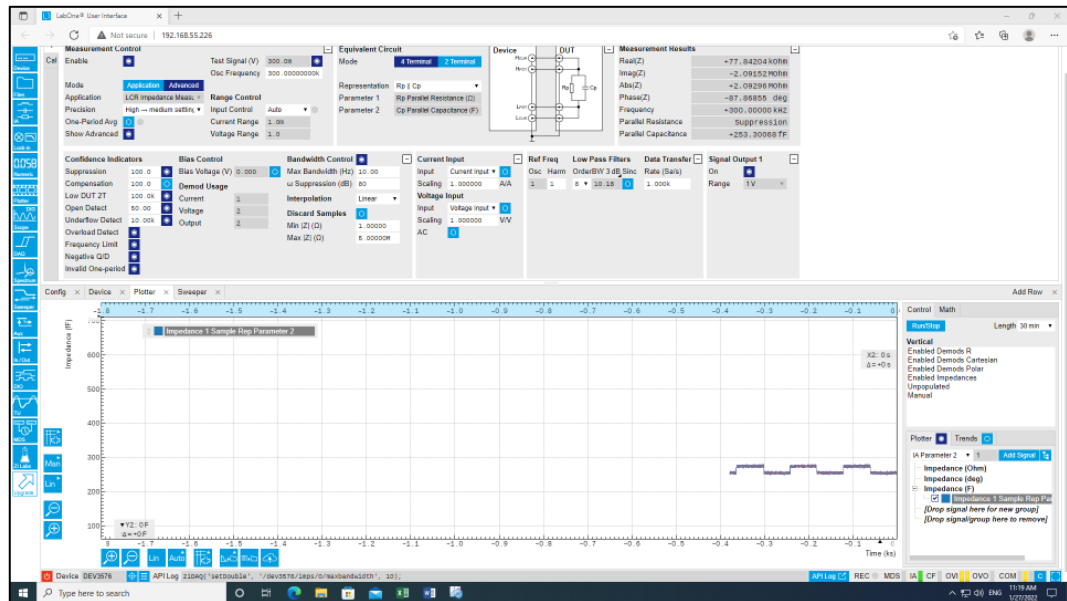


Figure A.10 The interface of the LabOne software.

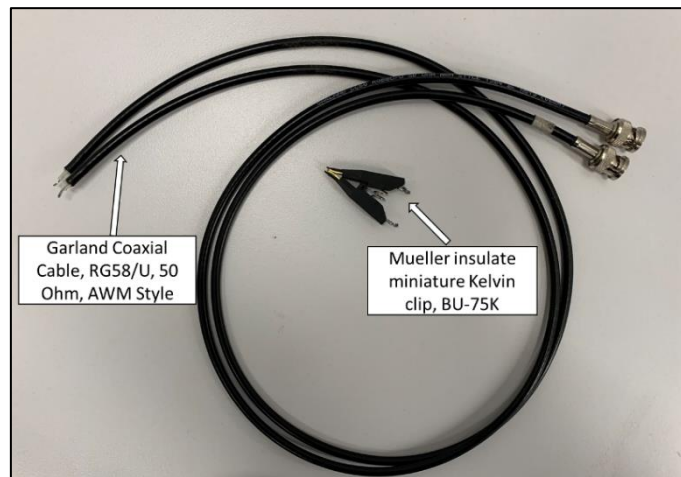


Figure A.11 Garland Coaxial Cable and Mueller insulate miniature Kelvin clip.

## Shimadzu EZ Experiment Devices - universal testing machine

The input or measured mechanical signals were performed by the universal testing machine (Figure A.12). This device could apply a uniaxial compression experiment at different strain rates to the items.



Figure A.12 Universal testing machine, Shimadzu EZ Experiment Devices [160].

#### Heated Vacuum desiccator “Vacuo-temp”

The temperature-dependent capacitance change measurement was performed by JP-Selecta Heated Vacuum desiccator “Vacuo-temp” (Figure A.13). The desiccator can adjust the temperature of its vacuum bell from ambient +5 °C to 170 °C with a resolution of  $\pm 1$  °C. During the temperature measurement, the vacuum desiccator was set at ambient room temperature +5 °C, which is 25 °C and it was heated at intervals of 5 °C until 75°C. To guarantee the accuracy of the temperature, five minutes of stabilization time after reaching the set temperature was required for each specified temperature.

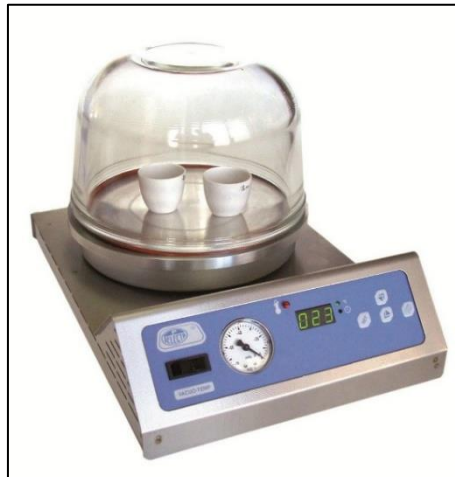


Figure A.13 JP-Selecta Heated Vacuum desiccator “Vacuo-temp”.



## Appendix B

The normalized capacitance change behaviour of the PGS dry sensor at all speeds and strain conditions are shown below.

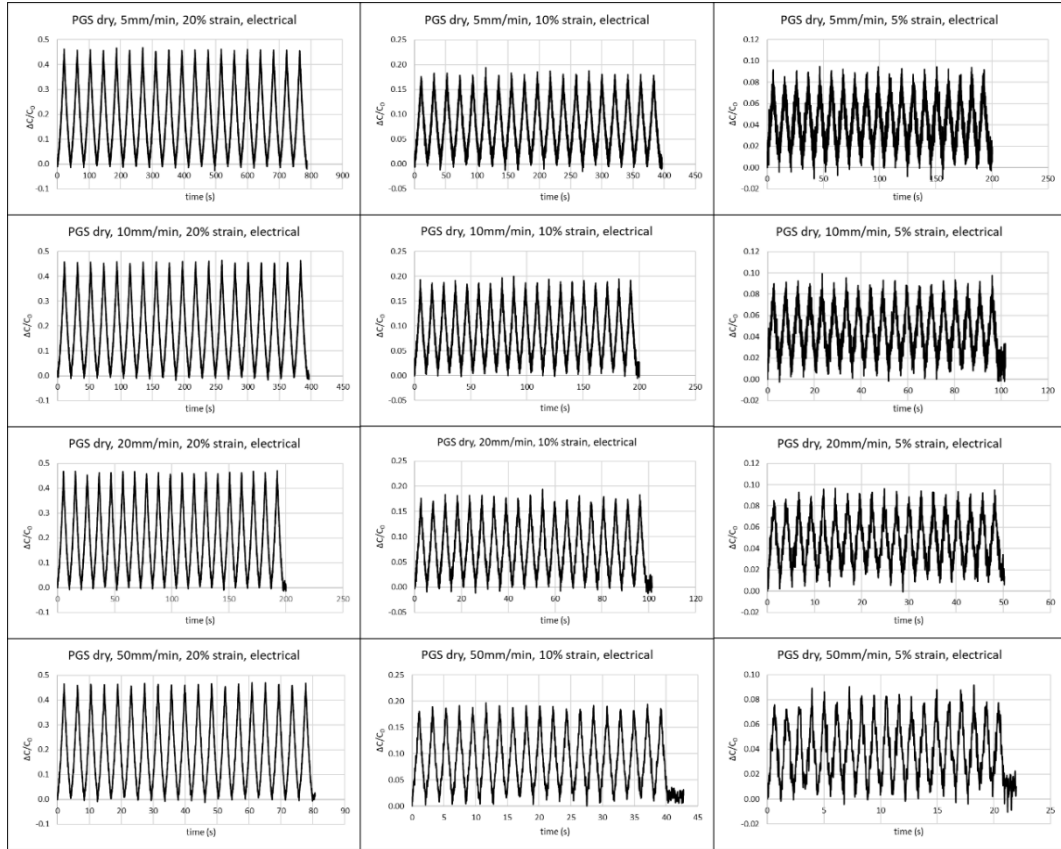


Figure B.1 The  $\Delta C/C_0$  of the PGS dry sensor under all conditions.

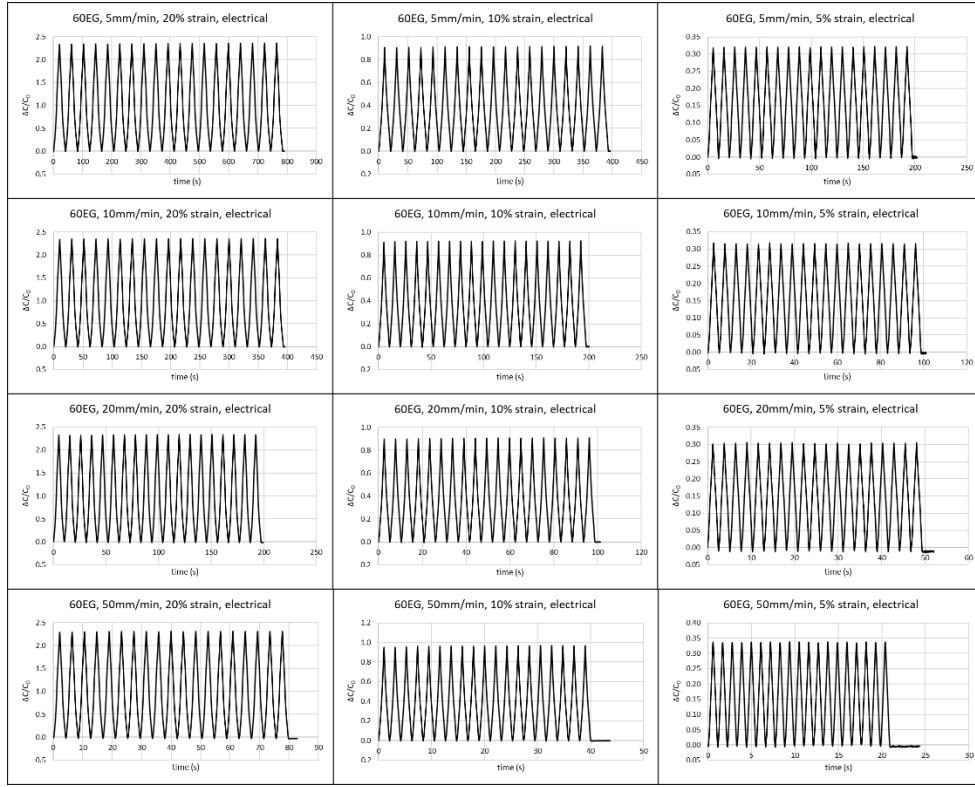


Figure B.2 The  $\Delta C/C_0$  of the PGS<sub>40</sub>/EG<sub>60</sub> sensor under all conditions.

The S and GF of the PGS dry sensor and PGS<sub>40</sub>/EG<sub>60</sub> sensor respectively at all speeds and strain conditions are shown in Figure B.3 - Figure B.6.

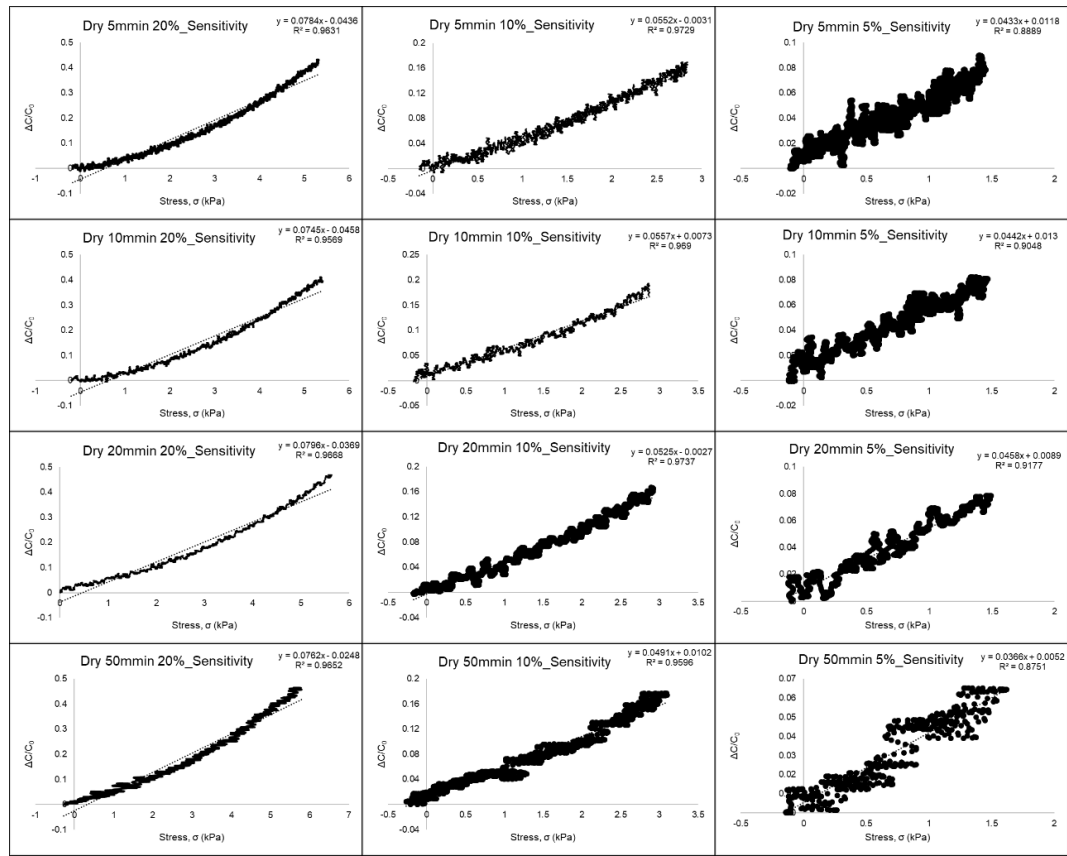


Figure B.3 The Sensitivity of the PGS dry sensor under the load speed of 5, 10, 20 and 50 mm/min , and strains of 5% 10% and 20% .

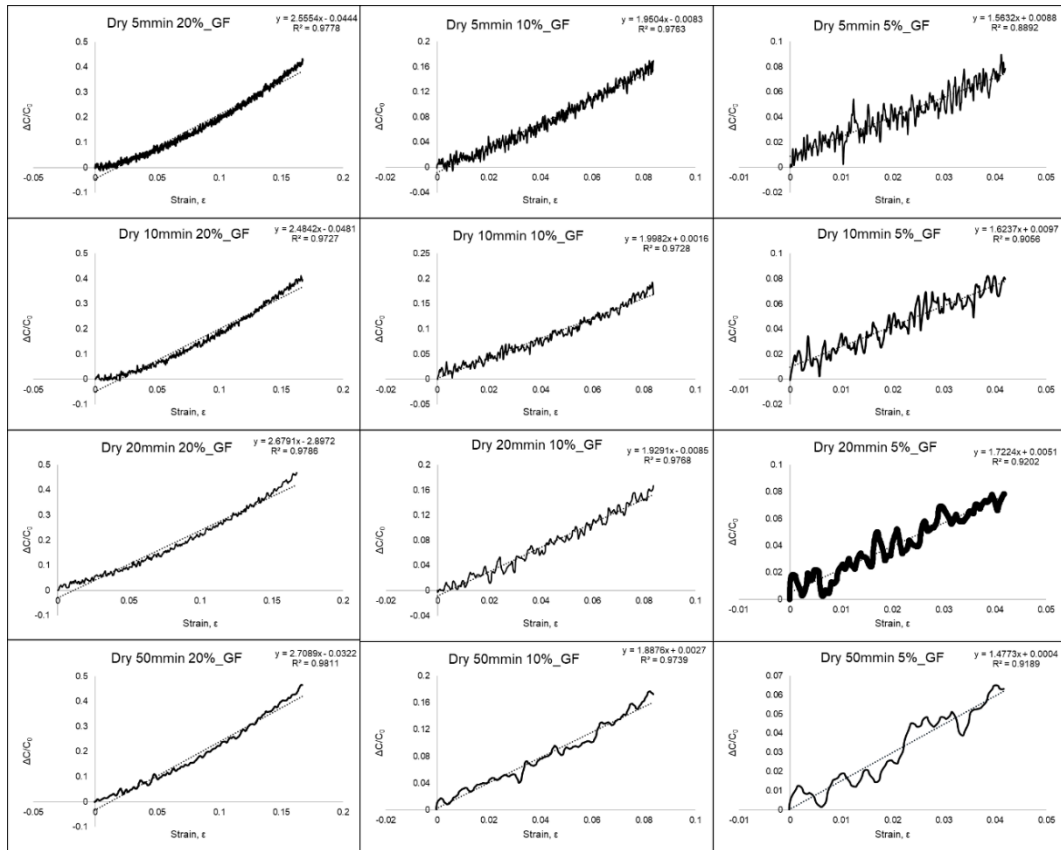


Figure B.4 The Gauge Factor of the PGS dry sensor under the load speed of 5, 10, 20 and 50 mm/min , and strains of 5% 10% and 20% .

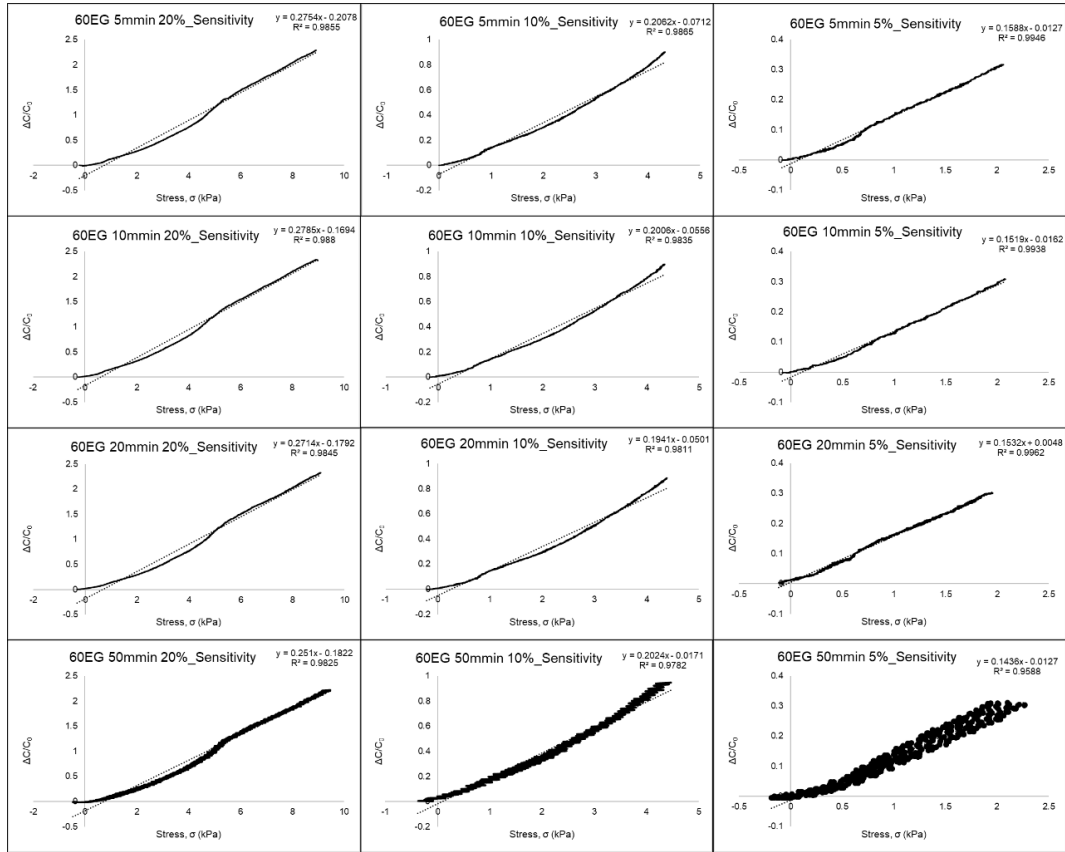


Figure B.5 The Sensitivity of the PGS<sub>40</sub>/EG<sub>60</sub> sensor under the load speed of 5, 10, 20 and 50 mm/min, and strains of 5% 10% and 20%.

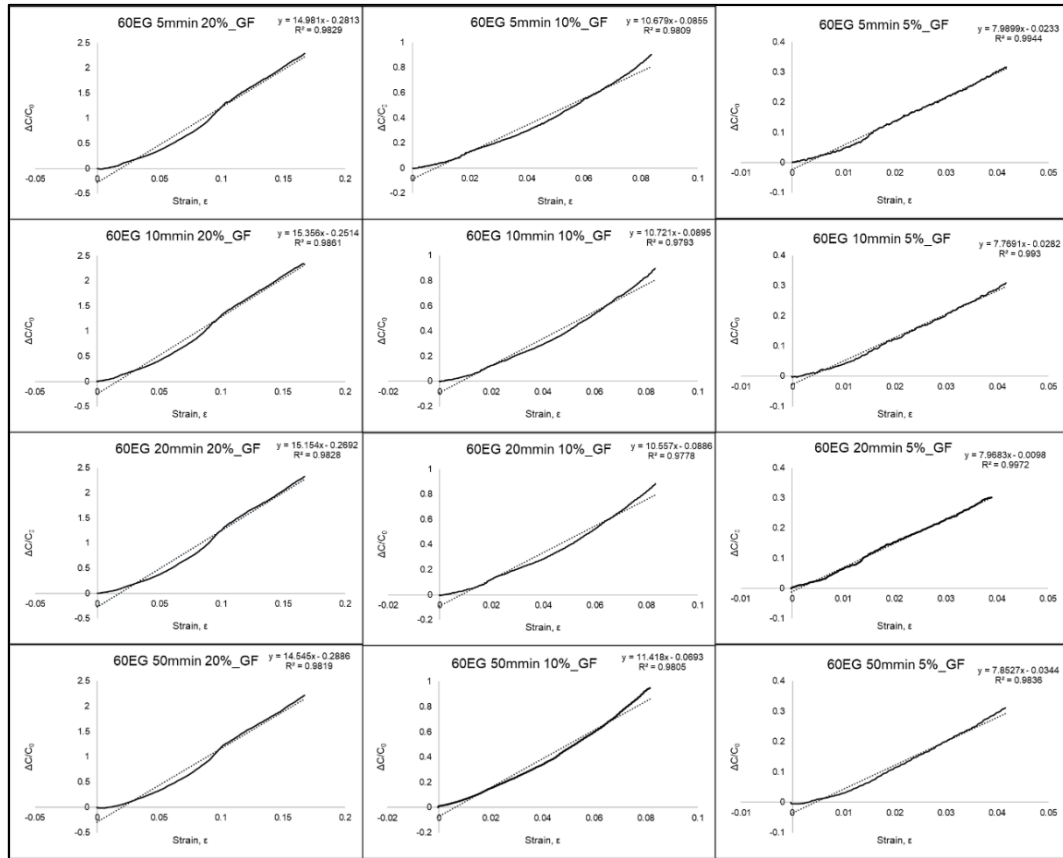


Figure B.6 The Gauge Factor of the PGS<sub>40</sub>/EG<sub>60</sub> sensor under the load speed of 5, 10, 20 and 50 mm/min , and strains of 5% 10% and 20% .

The stability experiments data of the PGS dry sensor, PGS<sub>60</sub>/EG<sub>40</sub> sensor, PGS<sub>40</sub>/EG<sub>60</sub> sensor and PGS<sub>20</sub>/EG<sub>80</sub> sensor are shown in Table B.1.

Table B.1 Stability experiments for 3600s. The  $\Delta C/C_0$  value, the drift difference of  $\Delta C/C_0$ , and the percentage change of  $\Delta C/C_0$  of the PGS dry sensor, PGS<sub>60</sub>/EG<sub>40</sub> sensor, PGS<sub>40</sub>/EG<sub>60</sub> sensor and PGS<sub>20</sub>/EG<sub>80</sub> sensor in.

Time (s)	$\Delta C/C_0$ value			
	0	40 wt%	60 wt%	80 wt%
500	47.43%	75.04%	221.11%	23.35%
1000	47.80%	75.36%	221.93%	23.64%
1500	48.05%	75.37%	222.62%	23.68%
2000	48.08%	75.57%	223.68%	23.58%
2500	48.19%	75.86%	223.48%	23.96%
3000	48.39%	75.96%	224.39%	24.43%
3500	48.46%	76.06%	225.30%	24.84%

Time (s)	Difference from the value of 500s				Percentage change from the value of 500s			
	0	40wt%	60wt%	80wt%	0	40wt%	60wt%	80wt%
500								
1000	0.37%	0.31%	0.82%	0.28%	0.78%	0.42%	0.37%	1.21%
1500	0.62%	0.33%	1.51%	0.32%	1.31%	0.44%	0.68%	1.39%
2000	0.65%	0.53%	2.57%	0.23%	1.38%	0.70%	1.16%	0.99%
2500	0.76%	0.81%	2.37%	0.61%	1.61%	1.09%	1.07%	2.61%
3000	0.96%	0.92%	3.28%	1.08%	2.03%	1.22%	1.48%	4.63%
3500	1.03%	1.01%	4.19%	1.48%	2.17%	1.35%	1.89%	6.36%

The repeatability experiments data of the PGS<sub>40</sub>/EG<sub>60</sub> sensor is shown in Table B.2.

Table B.2 Repeatability experiments of the PGS<sub>40</sub>/EG<sub>60</sub> sensor. The  $\Delta C/C_0$  and differences at load per cycle.

Cycles	1	2	3	4	5
Capacitance change (%)	235.1	236.3	237.6	237.4	237.4
The difference compared with the first cycles (%)		1.2	2.5	2.3	2.3
	6	7	8	9	10
	236.7	237.0	237.0	237.1	237.6
	1.6	1.9	1.9	2.0	2.5
	11	12	13	14	15
	237.8	238.1	237.8	237.6	237.9
	2.7	3.0	2.7	2.5	2.8